Monitoring and control of Metal-Based Additive Manufacturing Technologies

Alexander Thomas Burton - *MEng Mechanical Engineering (Distinction)*

MSc by Research

Heriot Watt University

IPAQS/EPS

January 2020

Abstract

This work shows the development of monitoring and control strategies for additive manufacturing (AM) processes. An arc-length control system and a PID temperature control system were developed for Wire-arc AM processes. An Oxygen monitoring/control system with a shielding gas crossflow was developed for Powder based fusion (PBF) processes.

The arc-length control system delivered a constant transfer mode and allowed for consistent temperature measurements whilst drastically improving process stability and part appearance. Small improvements where observed with the use of the PID temperature control system. Maximum temperatures were reduced by approximately 200°C. The results indicate a successful temperature control system requires the use of an independent arc-length control system. For PBF, a controlled environment capable of maintaining oxygen levels of 1ppm during the entire build process was designed. A simple monitoring/control system was developed to ensure the machine did not operate over a user selected oxygen concentration threshold. A laminar cross-flow device was developed to remove unwanted by-products generated by the PBF process. High speed imaging experiments were used to test the validity of the crossflow. The results show, that the use of a laminar crossflow device leads to a drastic improvement in process stability.

Contents

Table of tables

Table of figures

Chapter 1

Introduction to Additive Manufacturing

1.1 Background

Additive manufacturing (AM) allows complex geometries such as honeycomb structures to be produced directly from 3D CAD models. After years of being limited to making polymer prototypes for the visualization of product designs, AM techniques are now used to produce metallic parts across a range of industrial sectors [1]. Unfortunately, the names given to metal-based AM technologies developed in the late 1990s - such as direct metal deposition, laser engineered net shaping, shaped metal deposition and selective laser melting - were a source of confusion [2] [3]. Today, these technologies are named according to the guidelines of the American Society for Testing and Materials, which recognizes five nomenclatural categories: powder bed fusion (PBF), directed energy deposition (DED), binder jetting, material jetting, and sheet lamination processes [2] [4].

Metal-based AM can create fully dense components without the need for excessive machining or mould die manufacturing. In general, a 3D CAD model is sliced into 2D layers which are used to generate a tool path. In PBF and DED, a heat source such as a laser beam or an electric arc, is moved across the tool path to create a melt pool. Material is then added directly to this melt pool either in the form of powder or wire. This process generates solid beads joined side-by-side and layer-by-layer to create a 3D object [5]. The use of metal-based AM is of particular interest for the manufacture of components that are difficult to machine or that are made from expensive materials, e.g., titanium alloys. These technologies can be used to support traditional manufacturing methods, reducing costs and lead times [3], and to improve sustainability by reducing buy-to-fly ratios [6]. In addition, they offer the possibility of producing parts that could not be manufactured via traditional techniques.

Despite consensus among research and industry groups that metal-based AM techniques are game-changing and disruptive technologies that offer unique manufacturing possibilities, their widespread adoption has been hindered by the quality and repeatability of the parts produced [1]. The lack of AM adoption as a standard manufacturing method is certainly apparent in industrial sectors with high part quality requirements [2]. Thus, quality assurance remains a research priority. Some efforts have been made to monitor and control specific process parameters and also to modify already produced parts, in order to invest them with the desired mechanical properties. For example, heat treatment has been used for residual stress relief and to modify microstructure [7]. However, this post-treatment process greatly increases costs and is unfeasible for large objects. Quality and repeatability are thus rightly regarded as the current Achilles' heel of AM, and monitoring/control is required to establish metal-based AM as a viable production method [2].

Achieving high levels of quality and repeatability is difficult given the extremely complex underlying physical phenomena involved. In addition, the AM of metallic parts is a multivariable and strongly coupled process, susceptible to small variations in process parameters such as speed and power inputs. Further, small variations or disturbances in heat dissipation, previous bead geometry or layer temperatures can strongly influence part quality, and often force deviations from pre-optimized conditions [2] [8] [9]. In other words, disturbances over long build times may affect part quality. Defects may include increased porosity, poor bonding, low geometrical accuracy and over/under building [9].Research indicates that geometry and quality fluctuations arising from variations in process parameters cannot be eliminated by open-loop systems [8]. Thus, even if the adequate parameters for specific parts are obtained through an iterative process, part monitoring will still be required to truly deliver quality assurance.

Key parameters affecting part quality and appearance must be identified if adequate monitoring techniques and successful control systems are to be established. The literature highlights the importance of parameters across different metal-based AM techniques such oxygen level, scan speeds and melt pool temperatures. Oxides form due to the extreme heating phases of an AM process. The oxidation adversely affects

the wetting and spreading of the melt pool, thus deteriorating part appearance and geometrical accuracy [10]. Oxygen level monitoring and control continues to be a research priority and multiple research groups have focused in creating trailing shields, crossflow devices and control environments to reduce oxidation in different AM techniques.

Significant research efforts have also focused in temperature field monitoring and control since temperature has a direct impact on the microstructure, density, geometrical accuracy and mechanical properties of the resulting part [2] [5] [11] [12] [13] [14] [15]. For processes with more than one layer, heat accumulation over the build can lead to cracks appearing between the layers, and perhaps even total collapse [5], while if the heat input is insufficient the filler material will not melt, affecting part geometry [16]. Even if geometrical accuracy is met, the extreme heating and cooling phases of the process influence the microstructure of the part, strongly affecting its machinability and fatigue strength [15]. Some online temperature control systems have been developed that can adjust the process parameters over the build time to accommodate for heat build-up and disturbances, but research in this area is on-going [2].

Most of the research groups that have focused in controlling parameters during a metal-based AM process conclude that simple feedback control systems are not adequate and highlight the need for multiple independent control systems or multi-input-multi-output control systems.

This report discusses the design, programming and manufacture of two additive manufacturing machines (Wire-arc and Powder Based Fusion) and the development of multiple monitoring and control systems. This work shows how using control strategies such as oxygen control, arc-length control and temperature control can lead a drastic improvement in the quality and repeatability of the processes. For Wire-arc, the results indicate that the development of a successful temperature control system would not be possible without an arc-length control system. For Powder Based Fusion, the results indicate that the development of a shielding gas crossflow device and a simple oxygen-content control system greatly increases process stability. For both technologies, the application of monitoring and control

strategies has drastically improved the quality of the parts produced. The machines developed can now consistently produce complex parts.

1.2 Process overview

This work focuses on wire arc-based AM (WAAM), a kind of directed energy deposition (DED) and Powder Based Fusion (PBF).

1.2.1 Powder Based Fusion

In PBF-AM, metallic powder is distributed via a blade or a roller to create a uniform layers over a build area (see Figure 1). A heat source, usually a laser, is used to melt the thin layers together [2].

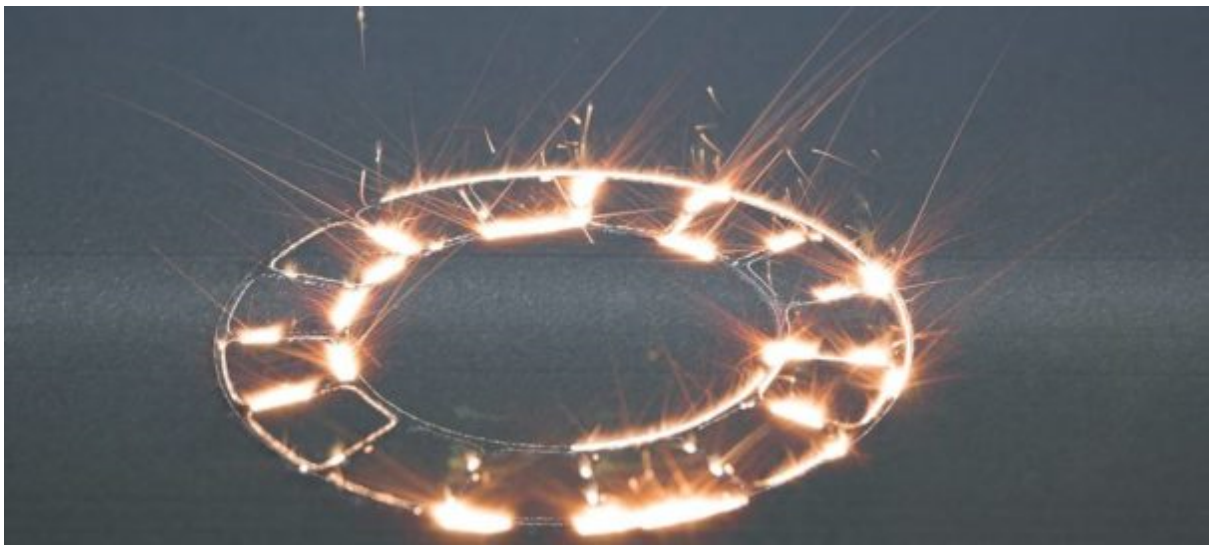

Figure 1. Example of powder-based fusion additive manufacturing during operation [17]

PBF allows for the production of complex three-dimensional metal products from metal powders [18]. The typical applications of this technology are parts with high geometrical complexity and small internal structures such as medical implants, turbine blades with cooling channels and complex casting moulds used by the aerospace sector [18]. However, PBF-AM has a large potential for manufacturing parts for a wide range of industrial sectors due to its almost infinite geometrical freedom and flexibility [18]. When appropriately used, PBF can result in shorter lead times to market, high production rates, high versatility and the ability to produce unique designs for one-off components [18]. However, defects such as pores, cracks, lack of fusion, key-hole induced voids, spatter and oxidation can be generated randomly, severely affecting the

quality assurance of the parts produced [19] [20]. PBF-AM currently provides the best dimensional resolution owing to the small layer thicknesses and widths achievable [21], and is already used to manufacture certain unique components such as titanium bone replacements.

The laser beam used to crate melt pools is controlled by a galvanometer (galvo). The galvos uses mirrors to direct the laser beam (X and Y direction) according to a pre-set laser path. The laser path is determined by the 2D layer slice information obtained from a CAD model [22].

The in-fill scanning strategy (hatching) is pre-defined and part dependent. To reduce residual stresses, the hatch directions are varied layer by layer. The hatch pattern chosen affects the length of the scan vectors and therefore influences the level of stress build-up in the component [23]. Three common hatching patterns used in PBF are: Meander, Stripe and Chessboard (see Figure 2) [23]. The latter divides the infill area into 5 by 5 mm islands with individual hatch directions. Every layer, the hatch direction is rotated typically 67° in an attempt to produce a homogeneous distribution of the residual stress [23].

Figure 2. Commonly used hatch patterns in PBF - Meander (left), Stripe (middle) and Chessboard (right) [23]

After scanning, the build platform is moved (Z movement) by a pre-set height and a new layer of powder is deposited. The key requirement when spreading powder is to achieve an accurate and repeatable layer thickness, typically around 50 µm [19]. Once the process is completed, the remaining powder can be sieved and re-used a finite number of times depending on the required specifications of the parts produced [22].

When the powder bed interacts with the laser, the formation of oxides can be observed. To prevent this, PBF technologies use chambers with low-oxygen atmospheres. Obtaining low levels of oxygen is normally accomplished by flushing the entire chamber with argon [24]. Commercial machines normally select a threshold value of oxygen concentration. For example, in the EOS M290 the process only starts when the sensors measure an oxygen level of 1000 ppm or less [24].

A shielding gas crossflow device is also used to remove spatter and unwanted by-products such as metal vapours and plasma plumes [24] [25]. In recent years, the importance of the crossflow devices has become apparent and several research groups have investigated the effects of such flow. For example, A. M. Philo et al. developed a multiphase CFD model that simulates the argon flow across the bed and investigated the spatter trajectories using high speed imaging data. Ahmad Bin Anwar tracked the spatter trajectories using a Discrete Phase Model [22] [25].

1.2.2 Directed energy deposition

DED covers a range of techniques but in essence is a complex process commonly used to repair, clad or build parts from 3D CAD models. A heat source is used to create a melt pool on the substrate, new material is then added to produce weld beads. DED can be divided into two major categories depending on how this material is added to the melt pool: wire- or powder-based DED.

Powder-based DED

Powder-based DED works by injecting a metallic powder though a nozzle to a weld pool (see Figure 3). It has many applications, including coating, tool repair, low volume manufacturing and design prototyping, etc. [26] [27]. A well-confined high-power laser can be used as the heat source. Small heat-affected zones can be created, minimising dilution and producing materials with enhanced mechanical properties [28] [29]. Indeed, this multilayer process can deliver multiple powders coaxially to produce functionality graded materials [29] [30] [31].

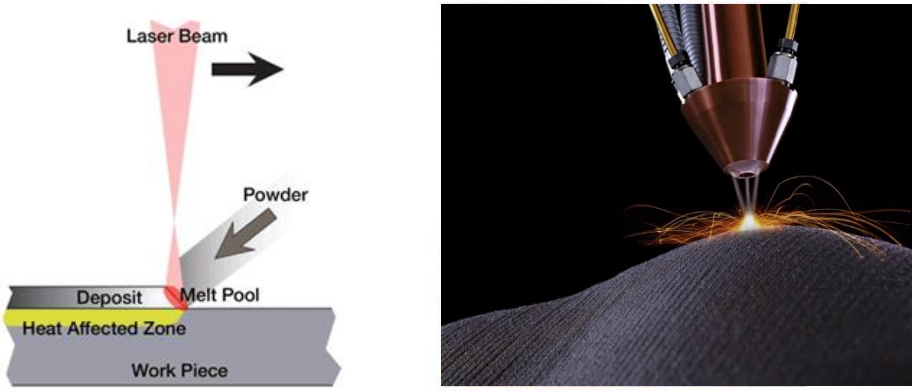

Figure 3. Example of Powder-based DED in operation (as provided in [32] [33])

Wire-based DED

Wire-based DED involves the injection of metallic wire into the melt pool (see Figure 4). It can be classified into three categories according to the energy source used to generate the melt pool: laser-based, arc welding-based, and electron beam-based DED [15]. Laser-based DED has attracted attention due to the clean working environment involved, the savings made in the use of materials, and the low contamination risks [34]. However, electron beam-based DED offers greater deposition efficiency and even lower

production costs [12]. In 2011, Baufeld et al. concluded that this technology was well suited for the near-shape forming of large components [12]. Arc welding-based DED has also shown great promise and offers advantages such as high productivity rates (its deposition rate is some 50-130 g/min while that of electron beam-based DED is just 2-10 g/min [15]), relatively low set-up costs, and powerful bonding strengths [34] [35]. However, all these advantages currently come at the expense of feature resolution.

Arc welding-based DED has been studied for some 20 years. In 1998, Spencer et al. examined ways of improving the microstructure and mechanical properties of components manufactured via this technique [34] [36]. In 2003, Zhang et al. studied the feasibility of using it to create 3D geometries [34] [37], and in 2009 and 2010, Xiong et al. and Karunakaran et al. developed new approaches in which milling was used to improve the dimensional accuracy and surface quality of the manufactured parts [34] [38] [39]. In 2011, Baufeld et al. compared the mechanical properties and microstructure of Ti-6A1-4V made via laser-based DED and arc welding-based DED [34] [40], while in 2012 Martina et al. studied the characteristics of plasma arc deposition for the production of Ti-6A1-4V [34] [41]. Later, in 2015, Martina et al. developed a system in which weld beads of deposited Ti-6Al-4V where compressed by a high-pressure roller that reduced the overall thickness and changed the microstructure of the parts produced from strongly columnar to equiaxed [42].

Arc welding-based DED can be further categorised into three common groups: gas metal arc welding-based DED (GMAW-DED), gas tungsten arc welding-based DED (GTAW-DED), and plasma arc welding-based DED (PAW-DED) [13]. GMAW-DED uses a DC current to create an arc between the filler wire and the work piece. The wire electrode is fed coaxially from a welding spool. The wire is melted by the arc and the resulting droplets fall on the substrate to generate a weld bead [5] [13]. This can achieve high deposition rates, rendering the technique more suitable for making medium to large sized structures [43]. However, the heat input from the GMAW torch is relatively large and can lead to residual stresses and distortions, as well as a poor surface finish, low geometrical accuracy and impaired mechanical properties [13]. Some research efforts have focused on alleviating the detrimental surface roughness. For example, Song et

al., in 2005, developed a technique in which milling is performed after each layer is deposited, thus creating a flat surface for the next bead [44].

In GTAW-DED and PAW-DED the arc is struck between a tungsten electrode and the substrate, and the filler wire is added to the melt pool independently [41] [13]. With these two technologies the angle and the position of the fed wire can be chosen to provide bridging transfer. This makes for a much cleaner and more controllable process, greatly improving part smoothness and layer appearance [12]. GTAW-DED is a relatively inexpensive AM method that can produce large structures at high deposition rates.

Due to the relatively large melt pools, severe oxidation effects can normally be observed. Currently, most GTAW-DED technologies use standard welding torch shielding gas mechanisms to prevent the formation of oxides during the build process. This shielding was designed to deposit single weld beads and does not provide adequate coverage when several layers have been deposited. Most of the oxides formed float to the melt pool surface and progressively accumulate. Several research groups have studied ways of mitigating the oxide formation effects with the use of trailing shields and controlled environments. Trailing shields have proven to mitigate some of the oxidation effects, but control environments are required to produce parts with stringent oxidation requirements.

Figure 4. Example of arc welding-based DED in operation [45]

Comparison between Powder and wire

Research indicates that wire-based DED allows for higher deposition rates with better deposition efficiency [5] [46] [47]. The deposition rate could be further increased by preheating the wire [46]. Although recycling is practiced, powder-based technologies have a low catchment efficiency (only 30-60% of the mass of powder used actually forms weld beads; the rest is scattered [5]). In contrast, wire-based DED processes are associated with little or no material waste [5] [47].

Numerous studies have also shown that parts manufactured using wire have better metallurgical properties and surface quality [5] while those made with powder tend to have some porosity [47]. The surface roughness of wire fed samples is around 40-60 µm, while for powder samples it is 70-90 µm. Thus, surface roughness is approximately 20-30% better in wire-fed parts [47]. Further, the use of wire allows for simple feeding mechanisms compared to the complex powder nozzles and powder spreaders [46]. Wire is also easier to produce and stock [21].

Powder based fusion (PBF) processes require the entire build area to be filled with powder, giving rise to inevitable material losses through contamination. Filling the entire area with metallic powder also becomes problematic when building large components [21]. Wire-based DED technologies, in contrast, are scalable and can produce large parts.

Despite these obvious benefits, wire-based DED processes are sensitive to changes in process parameters, such as the angle and direction of the wire feed [46] [47]. Problems such as droplet build-up and stubbing of the wire can dramatically reduce the quality of the parts produced [46]. Further, wire processes currently lack the dimensional resolution obtained with powder processes. Powder based fusion (PBF) processes can achieve high resolutions due to the small powder particles used, typically between 15-40 µm [21]. To date, most of the research performed with wire-based DED has involved wire diameters of approximately 1 mm, depositing bead widths between 5 and 15 times the wire diameter. However, some research investigating the use of microwires has yielded promising results [21]. In 2017, Demir developed a microwire-based DED process capable of delivering a homogenous microhardness over the build direction with a geometrical resolution close to that achieved by PBF manufacturing processes. This new

system could potentially deliver the resolution needed with the benefits of a wire system (see Figure 5). However, as highlighted by Demir, some control is still needed to increase repeatability [21]

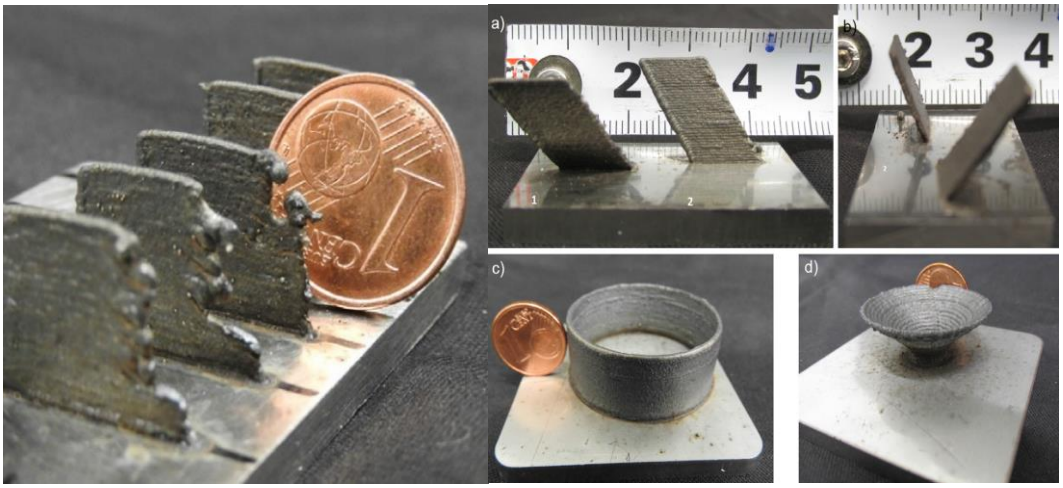

Figure 5. Parts produced by Demir's microwire laser-based DED [21]

1.3 Scope of thesis

This thesis covers work in DED and PBF. Heriot Watt's open architecture AM machines were further developed to deliver repeatable experiments. In both DED and PBF an existing experimental apparatus was re-designed, re-programmed and re-built to produce metal parts consistently and autonomously. The aim of this work was to develop multiple control strategies and test them in the open architecture AM machines. Full-scale manufacturing tests could be exploited by our collaborators at Cranfield University (DED) and Renishaw (PBF).

Chapter 2

GTAW-DED – Arc-length and Temperature Control System

1.1 Effects of temperature instability in GTAW-DED

Temperature is an excellent proxy for part quality and temperature control has been identified as a research priority in AM. Understanding how temperature affects the manufactured parts is crucial if metal-based AM technologies are to deliver quality assurance. According to Zeng et al., a homogeneous temperature field during manufacturing provides better part quality [48]. However, given the nature of the build process, it is currently impossible to maintain a constant melt pool temperature. The temperature increases significantly with build height and thus the cooling rates also change over time, affecting the microstructure [13]. Liberini et al., explained there to be three distinct microstructures in metallic AM parts due to the thermal histories of the different weld beads [15].

The first bead is in contact with a relatively cold substrate and heat is dissipated quickly by conduction [49]. However, as the build height increases with every layer, the newly deposited beads are further away from the substrate and a greater proportion of heat is dissipated through convection. Melt pool temperatures have been recorded to increase from 1500ºC to approximately 1700ºC over the first four layers [49]. If a constant heat input is maintained, the substrate and wall temperature increase over time, minimising the temperature difference between the new beads and the previous ones.

Further, different heat transfer mechanisms over the geometry of a part lead to large temperature fluctuations over the build process. For example, when support structures are present, heat conduction in localized areas will change, increasing the number of

temperature zones with different cooling rates over the part. Figure 6, shows that different heat transfer mechanisms lead to a part with changes in height over its length. The tall areas coincide with the regions where more conduction occurs. Areas built at higher temperatures have slightly wider and shorter beads.

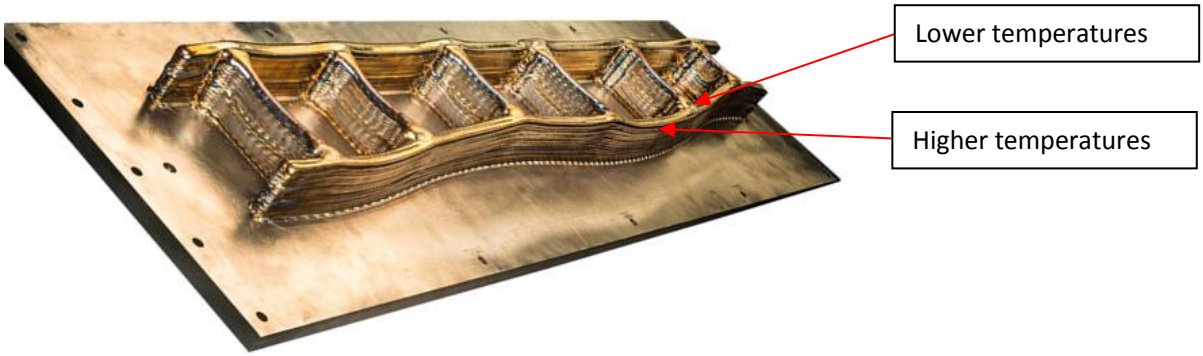

Figure 6. Example of how different heat transfer mechanisms can lead to geometrical inaccuracies if a constant heat input is maintained [50]

Similarly, at the end walls, the drastic increase in temperature caused by the change in heat transfer mechanisms from conduction to convection leads to wider and shorter beads (Figure 7).

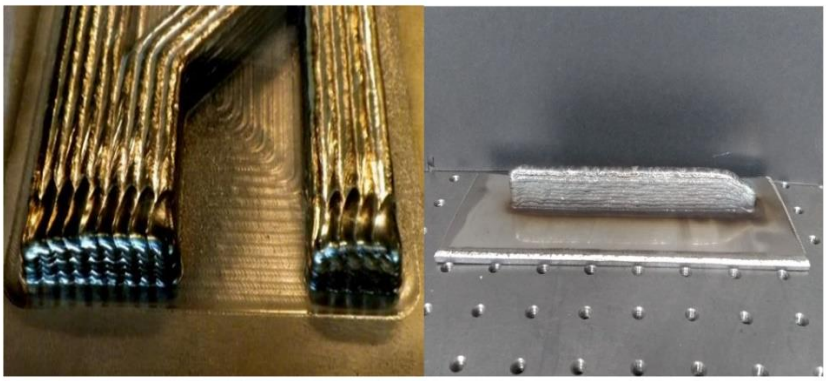

Figure 7. Example of how of changes in height due to heat accumulation at the end of walls

Repeated excessive heating can lead to large residual stresses and distortions, low geometrical accuracy, a poor surface finish and impaired mechanical properties [13]. Thus, most of the studies that have focused on improving part quality and geometrical accuracy have centred on thermal monitoring with temperature measuring devices [2].

Heralić et al., designed a control system to maintain a constant layer height and a stable temperature that yielded promising results. In their study, the melt pool width and and temperature were varied by changing the power input [5]. Further research from the same group highligted the importance of the relationship between temperature and the added filler material. Hua et al. also noted that, in order to produced components with the properties desired, a comprehensive understanding of the thermal behaviour of the material involved was needed [49].

Yang et al. investigated the thermal behaviour of GMAW-DED processes and also highlighted the negative effects of heat accumulation over time. To address the latter issue, they investigated the relationship between inter-layer cooling time and the quality of a single-bead wall, concluding that moderate prolongation of cooling time improved surface quality and geometrical accuracy [13]. A relationship between part geometry and temperature was also highlighted by Song et al. These authors developed a successful height control system based on temperature montoring. The power input was varied to control temperature and height. Bi et al. investigated the relationship between clad dilution, clad dimension and temperature. Their research led to a succesful monitoring and control system based on temperature control. They also concluded that laser power has the strongest influence on the temperature of the part [14].

Although significant research has focused on addressing temperature increase and the resulting thermal history, futher knowledge is needed to ensure the routine production of robust components with the required properties [2] [30] [51]. Correlating thermal history with microstrocture and temperature control could reduce the large numbers of expensive experiments currently performed by industry to optimise the building parameters for every manufactured part [51]. Existing temperature control sytems need to be significantly improved if they are to deliver the results that industry requires.

1.2 Temperature measurement devices

An adequate response time is a key requirement of any temperature-measuring device - certainly when the very rapid temperature fluctuations in a melt pool need to be monitored. The most common temperature monitoring devices used in GTAW-DED are pyrometers and thermocouples.

1.2.1 Pyrometers

The vast majority of studies that have focused on monitoring temperature in the vicinity of the melt pool have employed pyrometers, a consequence of the very high temperatures encountered (normally between 1200 and 2600 º) [2] [14] [28]. Pyrometers can be defined as non-contact temperature measurement devices that record a body's emitted thermal radiation [2]. Because they do not have to be physically in the melt pool, they can measure temperature in extreme conditions without being damaged [14] [15]. The term "pyrometer" is used broadly and covers multiple devices that rely on the principles of pyrometry to make temperature measurements. The pyrometers predominantly used in metal-based AM studies are photodiodes and digital cameras [2]. The cameras most commonly used are charged coupled devices (CCD) and complementary oxide semiconductor (CMOS) devices. In the literature, single point pyrometers are usually referred to simply as "*pyrometers*" while digital cameras are referred to as "*IR cameras*" or "*thermal cameras*". The same naming convention will be used here. Examples of the use of pyrometers, thermal cameras and photodiodes in metal-based AM technologies can be seen in the following studies: *pyrometers* - [52] [53] [54] [55] [56] [57] , *photodiodes* - [58] [59] and *thermal cameras* - [58] [60] [61].

From these studies it can be concluded that CCD and CMOS cameras are among the most powerful tools for obtaining temperature data simultaneously from different points [28] [29]. However, image processing is generally computationally demanding as well as time consuming, which limits response speeds - though they are fast enough to monitor bulk temperatures (see Figure 8) [30]. In contrast, single point pyrometers have good response speeds but provide limited information. However, the information stream is sufficient for online process control, and these pyrometers can be used for monitoring melt pool temperatures.

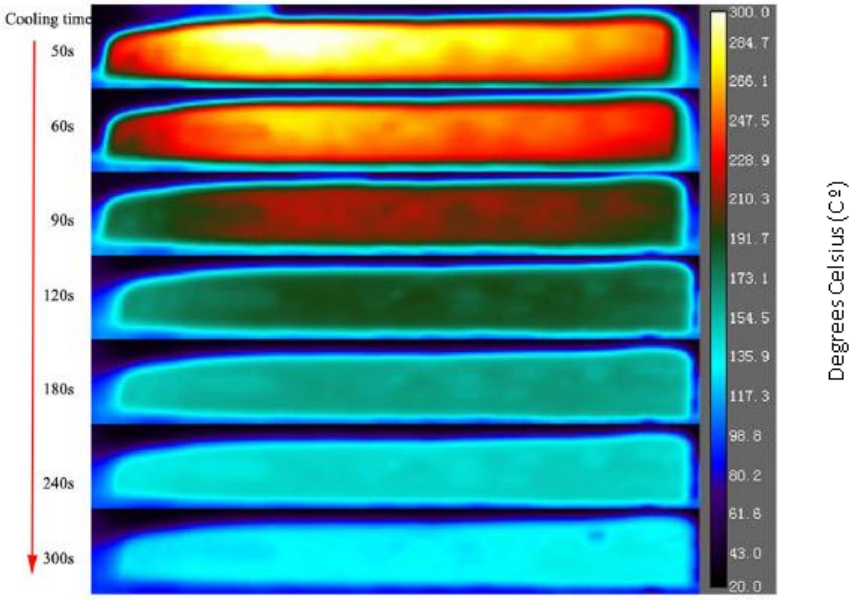

Figure 8. Example of the thermal images provided by a CCD thermal camera used for bulk temperature monitoring (part-cooldown) during a wire-based DED process [13]

Irrespective of whether single point pyrometers or thermal cameras area used, obtaining accurate data is a major challenge. The varying surface conditions, as well as the gases released during processes such as AM, can influence or obscure the radiation emitted [62]. To determine absolute temperature, the emissivity of the exposed surface must be known [30], and this can be complicated since materials undergo wide temperature variations and state changes. For bulk temperature monitoring, mean emissivity for all possible emission wavelengths and directions might be used to obtain a reasonable absolute temperature estimate [54].

For some applications, error-free emissivity measurements can be recorded if a two-colour pyrometer is used. A two-channel pyrometer is the only system on the market that can compensate for emissivity variations (See Table 1) [62]. However, these devices assume that the emissivity changes proportionally over both wavelengths and cannot always provide an absolute temperature. Köhler et al. studied the 'ruggedness' of different pyrometry devices, and presented the results below [62]:

Measuring concept	Accessibility of measuring site	Spatial resolution	Temperature span (K)	Ruggedness against disturbance	Sample rate (Hz)
One-channel pyrometer	High	0D	800 to 2000	Low	~166 k
Two-channel pyrometer	High	0D	700 to 2300	High	~500
Line pyrometer	Medium	1D	700	Low	~400
Filtered camera	High	2D	<500	Low	~150
Thermal camera	Low	2D	2040	Low	~440

Table 1. Comparison of temperature measuring devices

1.2.2 Thermocouples

A thermocouple is a contact temperature-measurement device. Their operation relies on the basic physical principal that electric current flows in a closed loop of two dissimilar metals when their junctions are at two different temperatures. The generated voltage is temperature-dependent and always in the millivolt range. A relationship between output voltage and temperature can be established [63]. Table 2 shows a list of the most common thermocouples and their operating parameters.

Type	Materials	Min temp	Max temp	Min°C	Max°C
J	Iron Constantan(Cu-Ni)	0°C	750°C	0 mV	42.281 mV
T	Copper Constantan(Cu-Ni)	-250°C	350°C	-6.18 mV	17.819 mV
K	Cromel (Ni-Cr) Alumel (Ni- Al)	-200°C	1250°C	-5.891 mV	50.644 mV
E	Cromel (Ni-Cr) Constantan(Cu-Ni)	-200°C	900°C	-8.825 mV	68.787 mV
N	Nicrosil (Ni-Cr-Si) NiSil (Ni-Si-Mg)	-260°C	1300°C	-4.336 mV	47.513 mV
S	Platinum-13% Rhodium Platinum	-50°C	1768°C	-0.236 mV	18.693 mV
B	Platinum-30% Rhodium Platinum-6% Rhodium	0°C	1820°C	0 mV	13.82 mV
C	Tungsten-5% Rhenium Tungsten-26% Rhenium	0°C	2320°C	0 mV	37.107 mV

Table 2. Common types of thermocouple used for AM temperature monitoring [64]

Although research into extreme temperature measurement has primarily focused on the use of pyrometers, several research groups have managed to successfully use thermocouples [2]. In 1999, Griffith et al. reported thermocouples to provide a relatively easy way of obtaining temperature measurements during the manufacturing process, and were able to monitor the in-process temperature and to study the solidification behaviour, residual stress and microstructural changes determined by the thermal

history [51] [49]. More recently, Martina et al. also used K- and R-type thermocouples to record the temperatures reached during a WAAM process [65].

Although thermocouples can provide accurate and consistent results without the calibration drawbacks encountered with pyrometers, the in-process temperatures reached during metal-based AM limit their use. High temperature thermocouples such as the ones made from Tungsten-Rhenium (maximum temperature of 2760°C) normally undergo a rapid deterioration when exposed to atmospheres containing oxygen at high temperatures [66]. These thermocouples are calibrated in hydrogen or inert gas atmospheres and the manufacturers indicate that they should not be used in air [66]. Although GTAW-DED technologies use localised shielding gas coverage the oxygen content is still relatively high. With the use of a trailing shield specifically designed for Wire-arc AM technologies, J. Ding et al. recorded oxygen levels between 2000-4000 ppm [67].

1.3 Monitoring and control strategies

GTAW-DED is a multivariable process susceptible to in-process variation that affects part quality. Even if process parameters have been specifically configured for a given part through experimentation, research indicates that disturbances during the build process may affect part quality and reduce repeatability. These small, unpredictable, in-process disturbances cannot be eliminated in open-loop systems [8]. Thus, a control system is necessary to correct them. Feedback or closed-loop control systems use measuring devices to compare the current process status to that expected. If a disturbance has deviated the process from the expected outcome, the control system will quantify that deviation and modify the process parameters to eliminate it as quickly as possible. For the control system to be able to correct the error in GTAW-DED, the relationship between the process parameters and the resulting weld beads must be known.

One of the main problems of a strongly coupled multivariable process is that modifying one parameter to reduce a specific error, e.g., the weld bead height, might affect another aspect of the build process, e.g., bead width, thus generating another error. Identifying an adequate control system with suitable dynamic models for metal-based AM techniques has proven rather complicated, although varying degrees of success have been obtained by different research groups. For a control system to be feasible, it is important to avoid the need to monitor a large number of inputs and outputs for each controlled variable. The key process parameters and their relationship with part quality and appearance must first be identified to simplify the system. The literature suggests there to be five variables that need to be controlled in metal-based AM technologies if accuracy and repeatability are to be ensured: bead height, bead width, wire position, temperature control, and microstructure control. Each of these variables has a process parameter with strong influence on the outcome.

The following sections will review existing control systems based on desired outcomes. For example, "*Height control*" will include control systems that change wire feed rate, scan speed and temperature since the desired outcome is to control height.

Table 3 shows the key process parameters used to control Temperature, bead height and bead width in AM.

Desired variable to control	Parameters changed to reduce control error
Temperature	*Inter layer cooling time* *Scan speed* *Power input*
Bead height	*Wire feed rate* *Scan speed* *Power input*
Bead width	*scan speed* *Power input*

Table 3. Key parameters previously used in AM processes to control temperature, bead height and bead width

1.3.1 Temperature monitoring and control

Several research groups have developed online temperature monitoring and control systems focused on improving the geometrical accuracy and mechanical properties of the manufactured part.

Temperature monitoring

Marshall et al. used pyrometers for non-destructive thermographic inspection as a means to ensure quality in Ti-6Al-4V parts [30]. The aim was to monitor temperature over the manufacturing process and relate the recorded data to microstructure formation [30]. They concluded that bulk heating due to the deposition of successive layers leads to microstructure variations over the part [30] and reported that pyrometer datasets were insufficient to predict microstructure formation [30].

Controlling temperature by changing the inter-layer cooling time

Yang et al. used an infrared camera to capture the surface temperature of parts during manufacture. Their aim was to investigate the thermal behaviour of GMAW-DED [13]. They attempted to control heat accumulation in the part by extending the inter-layer cooling time, concluding that a moderate prolongation of this time can lead to surface quality improvements and better geometrical accuracy. In agreement with Spencer et

al., they reported that the main reason for these improvements was the reduction in temperature of the previously deposited bead before the deposition of the new bead [13]. This study indicated that an inter-layer cooling time of 2-5 min yields the best surface quality; prolonging this period actually has a negative effect [13].

Controlling temperature by changing the power input

Using a PID control system and a pyrometer, Salehi et al. developed a simple melt pool temperature control system through LabVIEW [68]. Step response experiments were used to identify the relationship between the laser power and temperature. The group concluded that while LabVIEW can be successfully used to control the melt pool temperatures, this control does not ensure good quality beads, highlighting the need for a multi-input/multi-output control system [68]. Figure 9 shows the performance of their system.

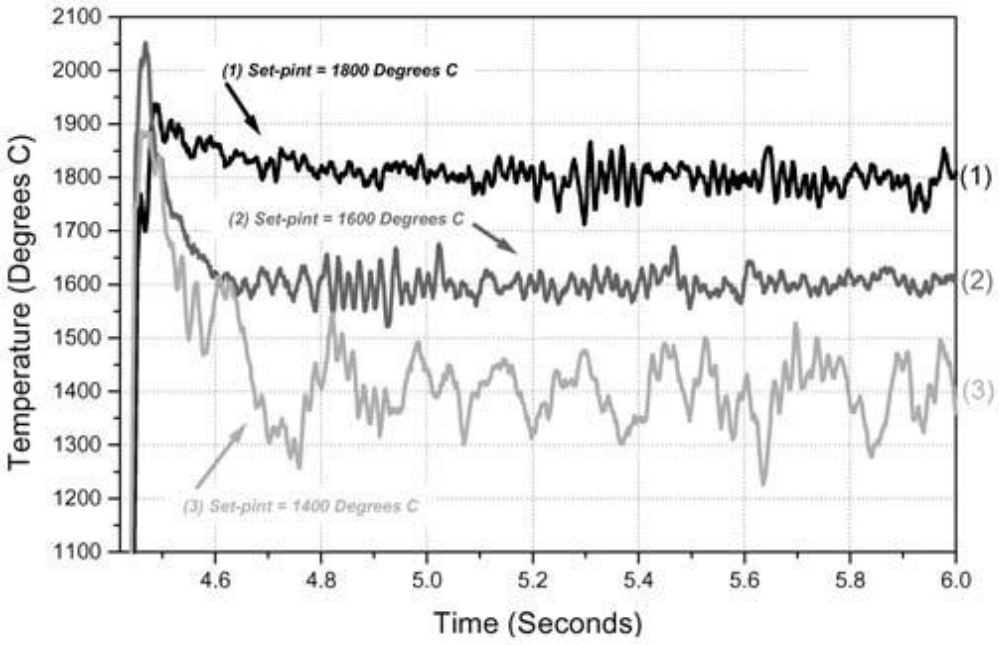

Figure 9. LabVIEW PID control system response showing temperature fluctuations over time for three different temperature setpoints (at t=0, the laser is initiated) [68]

Hua et al. developed a temperature monitoring system using a two-colour infrared pyrometer for powder-based DED. Interestingly, whilst studying the influence of process parameters on temperature, they concluded that the layer height could be directly detected by measuring the melt pool temperature, and accurately controlled by online adjustment of the process parameters [49].

1.3.2 Height control

In GTAW-DED, the layer height is normally pre-defined [34]. A common problem is that if the deposited bead height does not exactly match the expected value, there will be a mismatch between the bead height and the height increment. In a multilayer process, the height error may progressively increase. In conditions where the layer height is less than the height increment, intermittent deposition occurs [21]. When the layer height is greater than the height increment, the distance between the nozzle/welding-torch and the part being made is reduced layer after layer, eventually resulting in a collision with the part [21]. Further, the distance between the welding torch/nozzle and the substrate/bead affects the geometry of the beads deposited.

The deviation between the height increment and the bead height can be attributed to slight changes in deposition parameters such as current, arc voltage, deposition rate, etc [34]. In addition, especially for WAAM processes, large distances between the torch and workpiece can affect the shielding gas coverage, resulting in porosities and low-quality bead formation. If this distance is too short, welding spatters can adhere to the nozzle [34]. Thus, to achieve the required part quality, height control is essential. Several process parameters have a direct impact on layer height and thus a number of approaches to control height have been reported.

Controlling bead height by changing the wire feed rate

Xiong et al. developed a controller to keep the distance between the GMAW torch and weld bead constant. They established that the main parameters affecting height were voltage, current and the wire feed rate, with the last of these having the most influence on bead height [34].

Similar to research undertaken by other authors investigating DED control systems, Xiong et al. started with step response experiments to identify the relationship between the layer height and wire feed rate [34] [46] [3] [26] [28] [29] [31] . They concluded that because the result of the step response experiment was free of overshoot, the process dynamics could be approximated to a first order transfer function:

$$G(s) = \frac{K}{1 + T_s} e^{-sT_d} \qquad (8)$$

This conclusion was also reached by Fathi et al. and Heralić et al. [46] [26]. Xiong et al. then indicated that because of the time delay between changing the wire feed rate and the resulting height change, a simple step response experiment could not represent the dynamic behaviour accurately [34]. They also affirmed that the dynamics of the process changed with time, possibly due to heat accumulation. In addition, they indicated and that the parameters of the control system must change over time, and that a PID controller would be insufficient. The solution was an autoregressive moving average system able to simulate the process plus the use of an adaptive controller capable of identifying online the process parameters and controller parameters. The maximum error of this control system was ±0.5 mm (see Figure 10) [34].

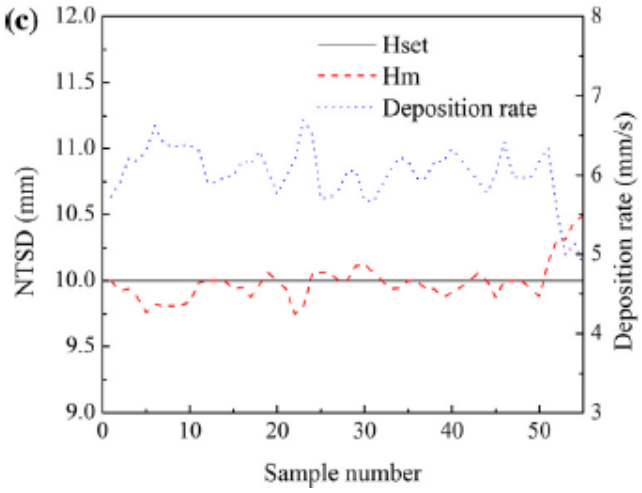

Figure 10. Height control experimental results showing how the control system changes the deposition rate to maintain a constant distance between torch and the part produced for the 15th layer [34]

Heralić et al. also found that the bead height mostly depends on the wire feed rate [46]. After their step experiments and the identification of the dynamic model, they concluded that a PID controller was unsuitable. Measuring the height of the bead just behind the melt pool was challenging because of the brightness of the molten metal [46]. A feed-forward control system was therefore developed. This measured the height of the previous layer in front of the melt pool and changed the wire feed rate to produce the required layer height, essentially compensating for any irregularities in the previous

layers [46]. This process yielded impressive results with a maximum error of 0.1 mm at the 13th layer [46].

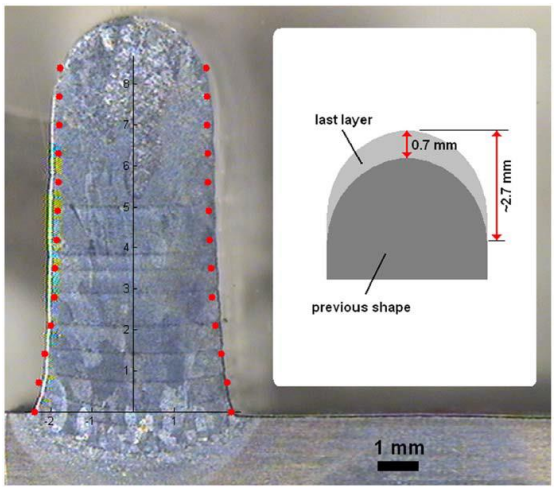

Figure 11. Example of wall produced using feed-forward control [46]

The same group later created another control system based on iterative learning to cope with arbitrary deposition patterns. This new system combined iterative learning for measuring height deviations and the use of a step height compensator [3]. This system had an identical maximum error of 0.1 mm at the 13th layer, and 0.2 mm at the 35th [3].

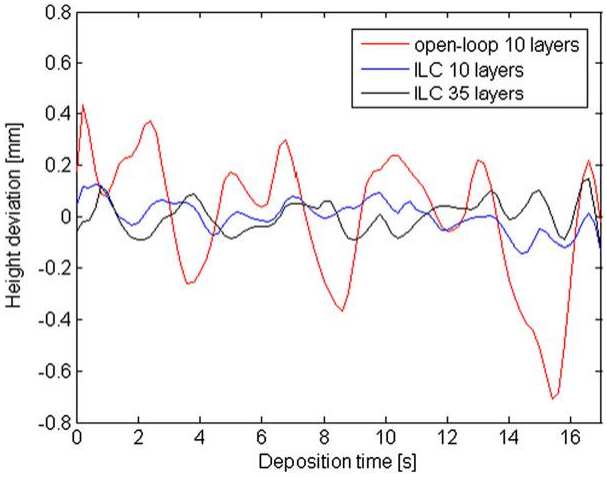

Figure 12. Comparison of bead height deviation over time with and without an iterative learning control system[3].

Controlling bead height by changing the scan velocity

Fathi et al. also developed a feed-forward PID to control clad height in powder-based DED [26]. The scan velocity was selected as the process parameter to vary in order to

obtain the appropriate clad height [26]. They based their PID control system on a first order transfer function obtained through step experiments. Figure 13 shows how the control system responded to a step change with a maximum overshoot of approximately 0.5 mm. After the system stabilised, the maximum error was approximately 0.1 mm [26].

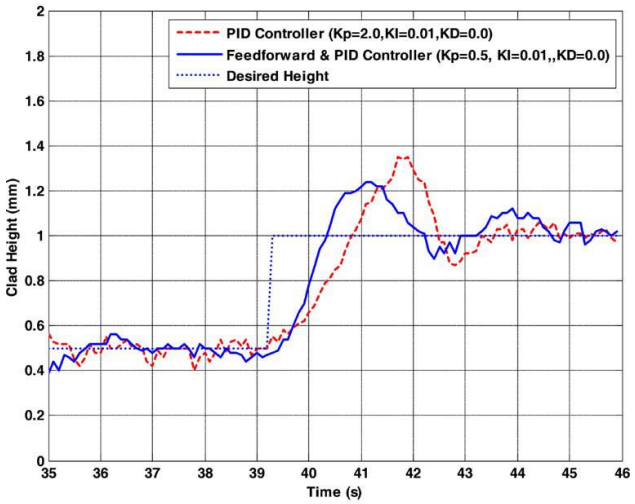

Figure 13. Feed-forward PID clad height control system response over time to a step change in the setpoint [26].

Controlling bead height by changing the power input

Song and Mazumder developed a generalized predictive controller (GPC) to control height by changing the power input to modify temperature [28]. They argued that, compared to a PID, a GPC offers better control and can be easily adapted to a multi-input/multi-output control system. A GPC essentially combines a feed-forward and feedback control design [28]. The feed-forward part predicts the height based on the experimentally determined dynamic system (a fourth-order linear state space model) whilst the feedback comes from the measured outputs and compensates for inaccuracies [28]. Their GPC managed to correct a purposely introduced change in height of the substrate by adjusting the laser power during cladding [28]. Song et al. also chose temperature as the process parameter to vary for controlling clad height. A two-input single-output GPC control system with a master height regulator and a slave temperature adjuster was used to control the height and melt pool temperature. A hierarchy of control systems was established so that constant temperature control was maintained - unless the layer height was above the expected value. In this case, the master height control system overrode the actions of the temperature controller to

reduce the clad height and avoid over-building. The maximum error obtained with this system was 1 mm. Further control systems that successfully vary laser power to control clad height are described in [31] [69] [70] [71].

In conclusion, the literature suggests that the wire feed rate has the most significant effect on bead height. A simple PID control system would seem insufficient to maintain a constant bead height. Arguably, the most successful control systems have a feed forward control, in which the data from the previous layer can be used to plan the next deposition.

1.3.3 Bead width control

In an open loop system, disturbances over the build time can lead to differences between the expected bead widths and the ones actually obtained. Further, heat accumulation over the build process has been reported to significantly affect the geometry of the weld profile. Research indicates, that in the same way as temperature, layer width is mostly affected by the power input [46]. Thus, control is necessary to ensure geometrical accuracy is obtained without long interlayer cooling times. However, despite the obvious importance of producing walls of the appropriate thickness, bead width control has received less attention than bead height control.

Controlling bead width by changing scan speed

Xiong et al. developed a single neuron self-adjusting controller for width control for GMAW-DED. The travel speed was selected as the input variable of the control system and the width was chosen as the output [8]. Step experiments were used to identify the dynamic model relating travel speed and bead width, as seen in Figure 14 [8].

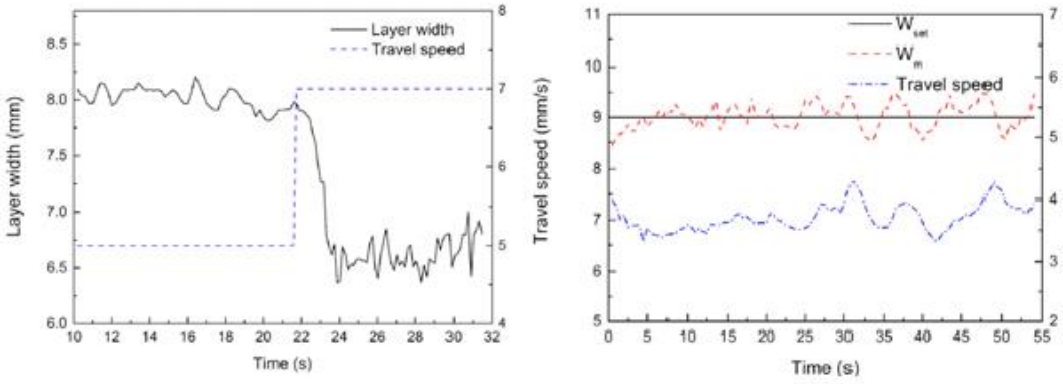

Figure 14. Step response experiments used to identify the relationship between travel speed and bead width (left) and control system response (right) [8]

Again, a first order transfer function was identified, as reported by other authors [46] [72]. However, Xiong et al. reported that it was necessary to establish a more accurate model. A non-linear Hammerstein-Winner model was used to describe the relationship between layer width and travel speed. According to the latter authors, a conventional PID with fixed parameters would not be suitable, and thus a single neuron self-adjusting controller was used [8]. Their control system yielded a maximum error of approximately 0.5 mm and took approximately 5s to mitigate bead width variation [8].

Controlling bead width by changing power input

Heralić et al. developed a simple PI controller that adjusted laser power for a robotized laser-based DED process. The K_p and K_i constants of the control system were identified using an experimental optimization procedure. This system was successfully coupled with a height control system [46]. The authors concluded that the PI width controller only contributed marginally to the stability of the process, and that the main contributor to overall geometrical accuracy was the height controller [46]. However, the PI controller did improve bead width and compensated for heat accumulation over the part. Their control system achieved an impressive maximum error of under 0.1 mm (see Figure 11) [46].

1.4 Control system discussion

Several research groups have developed successful control systems based on temperature monitoring to improve surface quality and geometrical accuracy by controlling bead width and height; a direct relationship exists between temperature and bead geometry. For wire-based DED processes, the parameters with the greatest influence on height and width are the feed rate and the power input respectively. The literature suggests that it is sensible to have the ability to control wire feed rate/scan speed and power input for the development of a new GTAW-DED temperature control system.

Consensus appears to exist among the most successful research groups that simple PID systems do not provide optimum control of geometrical accuracy. Relatively simple GPC and feed-forward PID control systems have arguably shown the most promising results. Indeed, it would seem that relatively simple control systems are the best of all. Complex control systems only seem to complicate matters or at best marginally improve them. The inter-layer cooling time could be used for offline bead mapping, alleviating the difficulties encountered when using online techniques. The data gathered from between layers can then be used to plan the next deposition. Careful parameter identification experiments to establish operational windows coupled with automatic offline adjustments and a relatively simple online control system, may hold the key to process stability.

1.5 GTAW-DED Experimental apparatus

1.5.1 Apparatus overview

An experimental GTAW-DED apparatus was developed to control various parameters during a multi-layer deposition process. Following conclusions from the literature, the apparatus and its accompanying software (LabVIEW) were designed to allow for offline (inter-layer) and online control.

Figure 15 shows a standard GTAW welding machine with a pencil torch used to generate melt pools. The torch is mounted on the Z-stage while the stainless-steel substrate is mounted on the X-stage. Stainless steel wire (1.2 mm diameter) is added independently through a wire feeder mounted on the Z stage. A Micro Epsilon 3D laser scanner is used to map the deposited beads. A Sensotherm two-colour pyrometer is also mounted on the Z stage and automatically changes its position as the wall height increases.

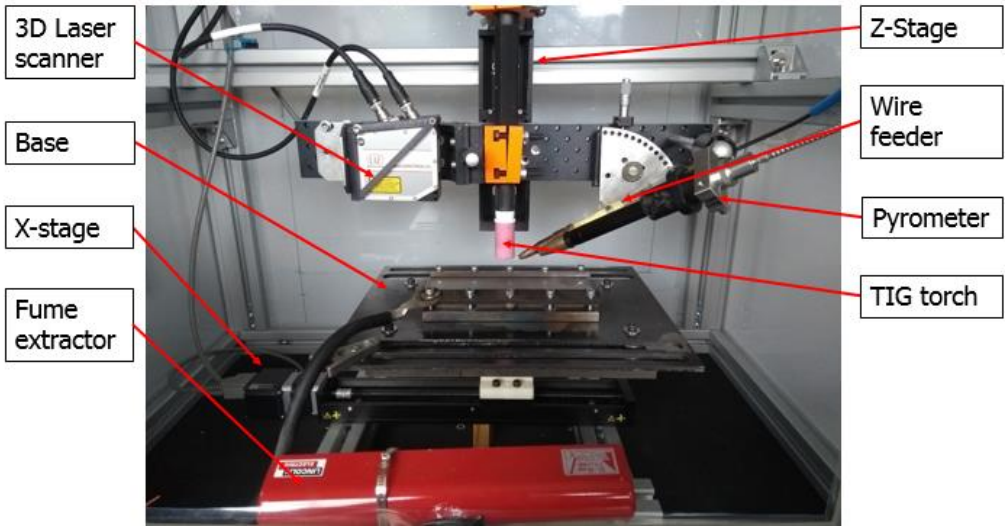

Figure 15. Experimental apparatus developed for melt pool temperature control in GTAW-DED

Figure 16 shows a CMOS and the thermal camera used to monitor the deposition process. The CMOS camera was used to monitor the melt pool, wire position and transfer mode while the thermal camera was used for overall process monitoring and relative temperature measurement.

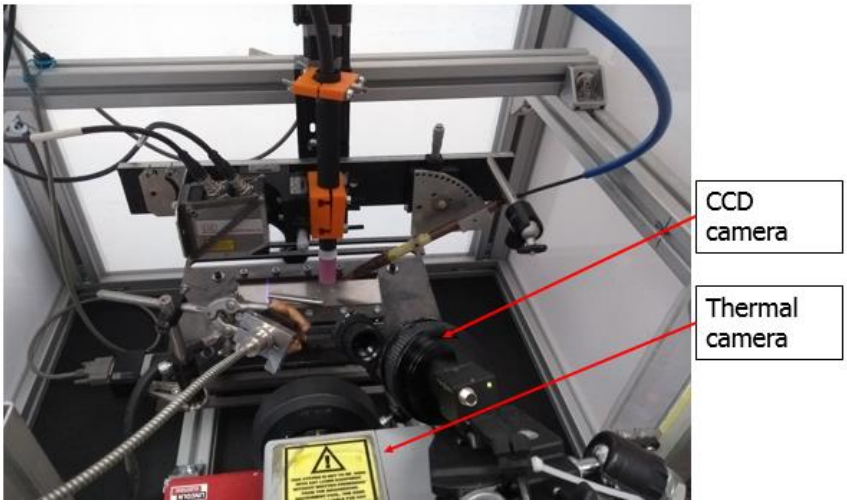

Figure 16. Experimental setup to monitor transfer mode, temperature and bead deposition during a GTAW-DED multilayer deposition process.

1.5.2 Apparatus components

Welding table/Printing bed and substrate clamp

The printing bed was made from steel to be able to withstand large temperature fluctuations. The connection between the bed and the X stage was made from polylactic acid plastic to insulate the electrical components from the welding current. It is worth noting, that all electronic components had to be well insulated to not be affected by welding process, specifically from the high frequency starter. Most of the errors encountered during experiments were due to an interference from the welding torch and the electrical components.

The welding bed was mounted on 4 springs with coaxial adjustment bolts (see Figure 17). This system allows for the welding bed to be adjusted with the use of a spirit-level and a feeler gauge. The adjustment procedure is similar to that recommended by FDM printer manufacturers. The welding torch is lowered into printing position and the feeler gauge is used to check the gap between the electrode tip and the substrate. This process

is repeated at numerous positions along the bed. The adjustment system ensured that arc-length was constant during the deposition of the first layer.

Figure 17. Welding bed adjustment mechanism

Figure 17 also shows the clamping method used to secure the substrate in place. The deposition process generates internal stresses in substrate. Without the clamping device, these stresses can cause severe deformations on the substrate. Twelve M6 bolts were used to secure the substrate in place during the entire deposition process.

Welding torch power control

In a GTAW welding machine, the power input is controlled by changing the current. Commonly a welding operator uses a pedal for this. A pedal bypass device was used to emulate the pedal mechanism, with a voltage generator run by LabVIEW software. This in-house software can change the current by altering the output voltage to the pedal bypass device. Interestingly, the relationship between the output voltage and current changes depending on whether the welding torch current is being increased or decreased (Figure 18). Further experiments with random changes in current verified this.

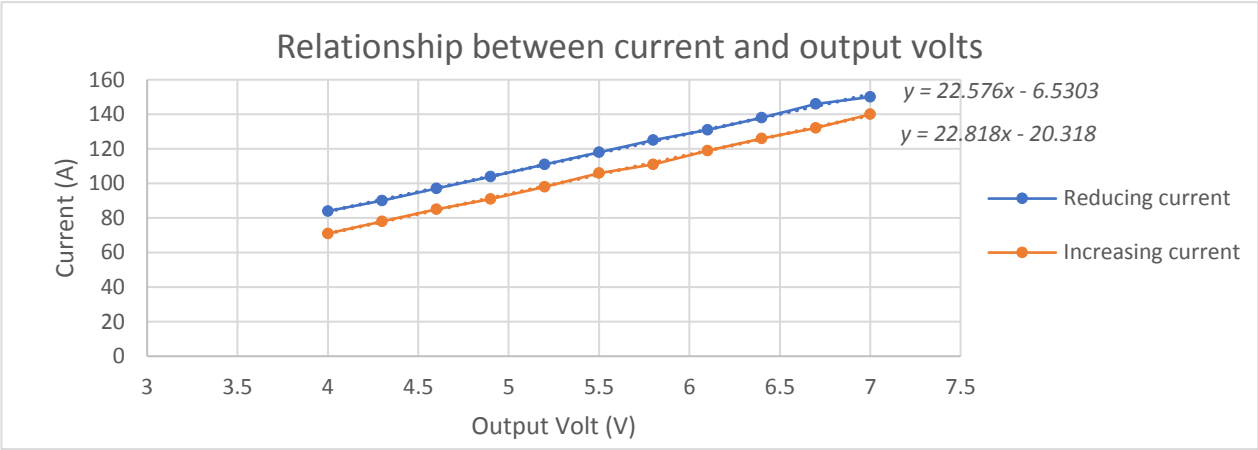

Figure 18. Relationship between pedal bypass voltage and the welding machine current output

Figure 18, shows the relationships between output voltage to the pedal bypass device and the welding torch current. The LabVIEW program uses these relationships and a current transducer (feedback device) to accurately control the current. The LabVIEW program was specifically designed to have independent loops that allow for adequate response times.

Gas shielding nozzle

A standard straight No.10 gas lens cup was used for local gas shielding. With this localised shielding method, the arc-stability was maintained during the entire build. However, after multiple depositions the formation of oxides was apparent. The parts produced with this method of shielding were heavily oxidized.

Wire feeder

The wire feed rate is also controlled with an analogue voltage output through LabVIEW. To control the feed rate, the relationship between the output voltage and the wire feed rate had to be established experimentally (Figure 19).

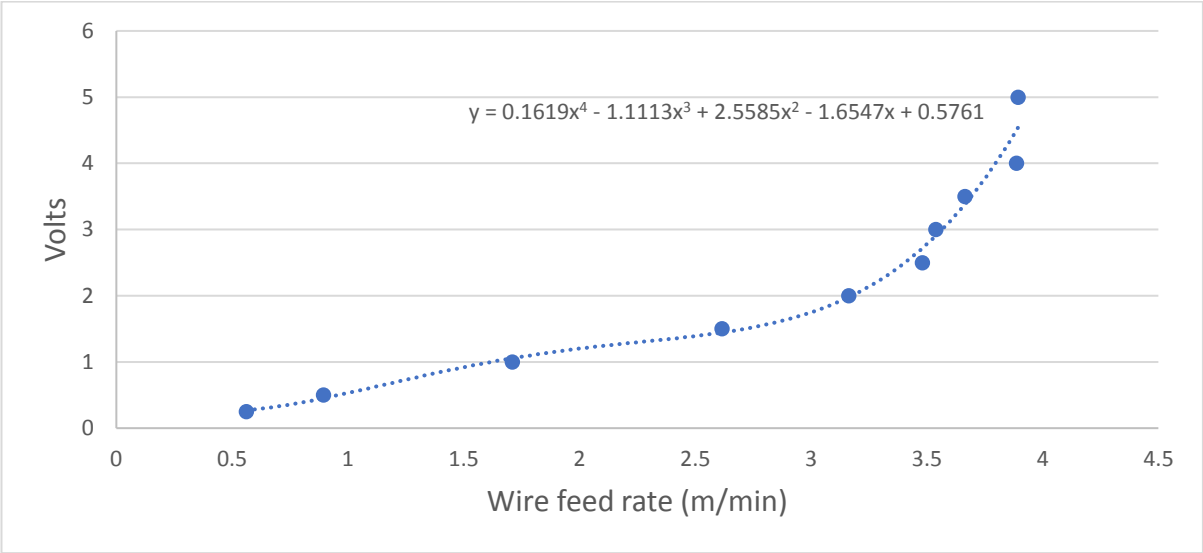

Figure 19. Relationship between LabVIEW controlled output voltage and the wire feed rate

The position of the wire feeder can be adjusted manually using mechanical stages. As highlighted by other authors [15] [40], the position of the wire within the melt pool can affect the geometry of the weld bead (see Figure 20).

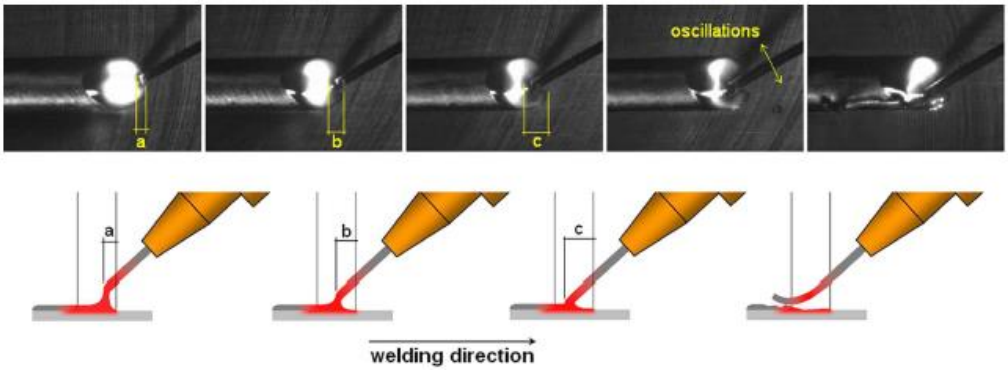

Figure 20. Relationship between wire position and transfer mode/weld bead geometry in a laser-based DED process [16].

If incorrectly positioned, the wire location with respect to the melt pool can lead to poor weld bead quality. Syed et al. concluded that a good bead was obtained when the wire was positioned at the leading edge of the melt pool [47]. For wire-based DED processes, the best feed direction is from the front, since it allows for more flexibility in the process parameters [16] [47] [73] [74]. Back-feeding usually requires rigorous parameter identification experiments and often leads to serrations [16] [47].

The wire feeder was set at an angle between 20º and 60º to achieve a bridging transfer mode at the edge of the melt pool in a front-feeding process.

3D scanner

The 3D scanner projects a laser line onto the deposited weld beads and through process imaging creates a 3D model of the growing part [47]. This 3D model is composed from 2D slices. The Micro Epsilon laser scanner used, has a resolution of 0.03 µm and a maximum sample rate of 0.5 ms [68].

The LabVIEW program relates the feedback position from the X stage to the 2D profiles. With these profiles, weld bead width and height can be measured and related to the X stage position. The 3D scanner is used to measure the wall height after a layer is deposited to plan the Z stage movement for the next deposition.

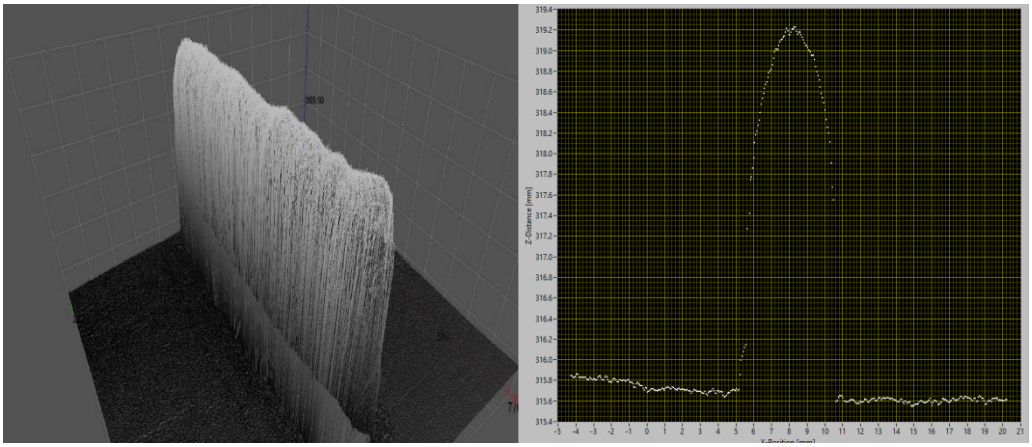

Figure 21. Example of the 3D and 2D profiles obtained by laser scanning during a multi-layer deposition process. The 3D profile (left) is composed of numerous 2D profiles (right)

Pyrometer

A SensorTherm two-colour pyrometer is used to measure single spot melt pool temperature required for process control. The pyrometer has a response time of 1 ms and can record temperatures of 400-1600°C. The LabVIEW program can also relate temperature to position using feedback from the X stage. To reduce noise, a 10 data point mean was calculated to produce one temperature output every 10 ms.

GTWA-DED LabVIEW program

The LabVIEW program was developed to automate the entire deposition process. Once the operator starts a multi-layer deposition, it requires no further intervention until the part is completed or the print fails due to the lack of control systems. However, the program, allows for manual interventions from the operator when the developed control systems are not operational. It is important to mention that the program has been designed to not be affected by the component with the slowest response rate; it works by using independent loops that truly allow the individual feedback devices to gather data at their individual maximum sample rates. MATLAB scripts linked with the LabVIEW program were used for the more mathematically demanding operations of the control systems.

1.5.3 Part building experiment procedure with no control systems

Once the welding bed has been calibrated, the wire feeder was set at an angle of 30º with the substrate. The welding torch and the wire feeder have to be manually aligned with mechanical stages. These mechanical stages are mounted on the Z stage and allow the torch and the wire feeder to have three degrees of freedom. The alignment between the torch and the feeder is crucial for the deposition of adequate weld beads and it requires a simple experiment to be conducted as follows:

1. The Z stage is moved until the tip of the tungsten electrode (grinded to 60º) is approximately 3.5mm from the substrate.
2. An initial visual alignment of the torch and the wire feeder with the mechanical stages is conducted.
3. The current is set to 150A and the arc is struck between the welding torch and the substrate.
4. The wire should be added manually through the wire feeding system. The feeding process should be smooth. If the operator detects any resistance, it is likely that the welding torch and the wire feeder are misaligned. The operator should also check that the wire is positioned at the leading edge of the melt pool.

5. Once the wire feeder and the welding torch are aligned, the CMOS camera can be used to verify the selected transfer mode. A bridging transfer mode leads to the best results.

Small misalignments between the wire feeder and the welding torch lead to serrations and wire stubbing that often result in a failed print. Once the alignment is completed and a new substrate is in place, the welding torch is moved to the "home" position. Through the LabVIEW program the wire feed rate, part length, current and the height increment are set. Note, that for the uncontrolled process a pre-defined layer height is chosen. After the first deposition, the transfer mode is likely to have changed from a bridging transfer mode to a globular transfer mode. Even the operator was to measure each bead after being deposited and adjusted the height increment in the LabVIEW program, geometrical inaccuracies along the length of the wall are still likely to affect the transfer mode.

The sequence between X stage movement, the wire feeder and the welding torch activation is crucial to ensure an uninterrupted deposition. The LabVIEW program has been specifically designed to be able to adjust this sequence. First, the X stage movement is initiated, then welding torch is activated and 0.5 s later the wire feeder is triggered. This ensures that the melt pool is already established before the wire is fed. At the end of the wall, the sequence is reversed. The wire feeder stops before the welding torch to ensure that the wire does not stick to the part. The welding torch stops before the X stage to reduce the heat accumulation at the end of the wall.

1.6 Temperature measurement for a temperature control system

The aim was to monitor temperature changes during bead deposition using a two-colour pyrometer for online control. To develop a successful temperature control system, the pyrometer data had to show the drastic temperature changes expected in the areas of the part with less effective heat transfer mechanisms, e.g., the end of the wall. However, as highlighted in the literature, obtaining the absolute temperature through pyrometry can be challenging and some problems were encountered.

1.6.1 Issues encountered with the two-colour pyrometer

When trying to capture melt pool temperatures during bead deposition there was a severe lag in the output of the two-colour temperature readings. Figure 22 shows that during a simple stainless-steel heating experiment, the individual channels (***k1*** and ***k2***) showed the relative temperatures at the expected time, while the two-colour temperature readings came with a significant delay.

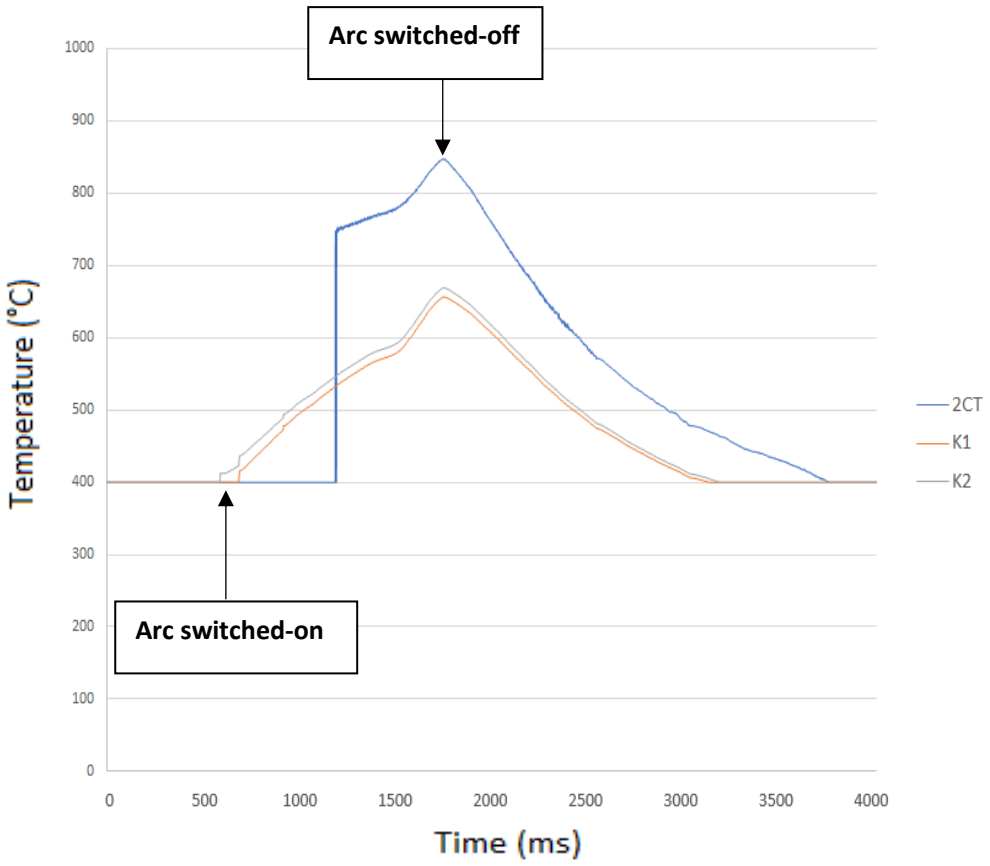

Figure 22. Data output delay example of the two-colour pyrometer during a stainless-still heating experiment

Light-proof pyrometer box

Initially, the delay in the two-colour readings was assumed to be caused by the light emitted by the welding torch. To test this hypothesis, a light-proof steel box was used to shield the pyrometer. The welding torch was placed on the outside of the box and the pyrometer was placed inside. Figure 23 shows that no improvement in the lag was obtained.

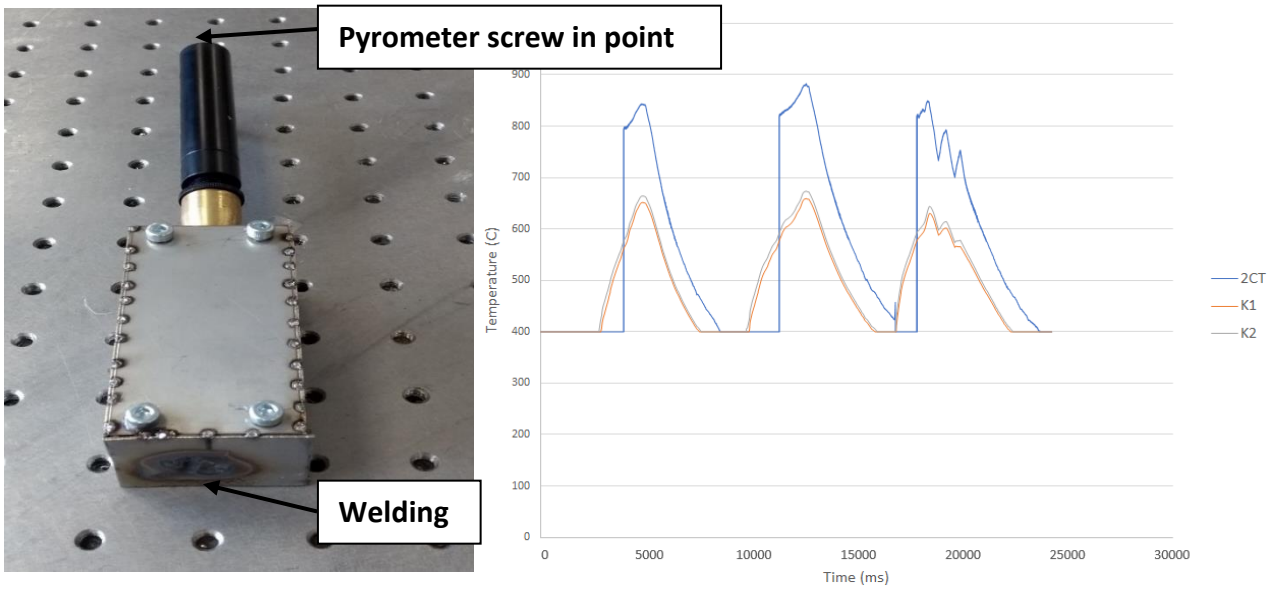

Figure 23. Arc-light interference experiment (attempt to reduce the lag in the pyrometer readings using a light-proof box)

Calculating the two-colour temperature from the two data channels

In an attempt to understand the reason for the lag, the two-colour temperature was calculated from channels ***k1*** and ***k2*** using a simple in-house program based on the following equations. The energy radiated by a black body is described by Plank's radiation equation:

$$N_{\lambda,b} = \frac{C_1 \lambda^{-5}}{e^{\frac{C_2}{\lambda T}} - 1} \quad (1)$$

where:

$\boldsymbol{N_{\lambda,b}}$ is the spectral radiance (W/ (cu cm) (steradian)

$\boldsymbol{C_1}$ is the first radiation constant (C_1= 1.1909x10^{-12} (cm^2 steradian))

$\boldsymbol{\lambda^{-5}}$ is the wavelength (cm)

$\boldsymbol{C_2}$ is the second radiation constant (C_2= 1.438 (cm K)

T is the temperature (K)

However, the Wien approximation was used because of its relative simplicity [75]:

$$N_{\lambda,b} = \frac{\varepsilon C_1 \lambda^{-5}}{e^{\frac{C_2}{\lambda T}}} \quad (2)$$

For a two-colour pyrometer:

$$N'_{\lambda_1,T} = \frac{\varepsilon_1 C_1 {\lambda_1}^{-5}}{e^{\frac{C_2}{\lambda_1 T}}} \quad (3)$$

$$N'_{\lambda_2,T} = \frac{\varepsilon_2 C_1 {\lambda_2}^{-5}}{e^{\frac{C_2}{\lambda_2 T}}} \quad (4)$$

$$\frac{N'_{\lambda_1,T}}{N'_{\lambda_2,T}} = R_o = \left(\frac{{\lambda_2}^{-5}}{{\lambda_1}^{-5}}\right) e^{\left[\frac{C_2}{S_C}\left(\frac{1}{\lambda_2} - \frac{1}{\lambda_1}\right)\right]} \quad (5)$$

where $\mathbf{S_C}$ is the colour temperature. These equations represent the ideal case in which the product of the detector and the transmittance of the optical glass of the pyrometer has a value of 1 [75].

The output of the pyrometer will be the ratio of the two signals incident upon the photodetector ($\mathbf{R_o}$). Once $\mathbf{R_o}$ is known, $\mathbf{S_C}$ can be calculated. The true two-colour temperature can then be obtained using a correction graph (Appendix A). This graph will display the relationship between the true temperature and the colour temperature for different emissivity ratios. The advantage of the two-colour system is that the individual emissivities at both wavelengths might change at the same rate, maintaining the ratio. This means that once an adequate emissivity ratio is obtained, the true two-colour temperature can be obtained even if the material changes its emissivity - as long as the emissivity at both wavelengths changes at the same rate.

From the temperature output of the individual channels, $\frac{N'_{\lambda_1,T}}{N'_{\lambda_2,T}}$ can be calculated, assuming $\varepsilon_1 = \varepsilon_2$ (grey body) [76] . In this condition, the emissivity term cancels out, and $\mathbf{S_C}$ and $\mathbf{T}$ are equal. This means that if a material has the same emissivity at both wavelengths, the true two-colour temperature can be calculated without a calibration graph - as long as the emissivity changes at the same rate for both wavelengths and the condition $\varepsilon_1 = \varepsilon_2$ is maintained. Based on Plank's law, to achieve this condition the wavelengths chosen must be close to each other. However, as shown in Figure 24 the

emissive power of a real object may vary differently across wavelengths making it difficult to select an appropriate off-the-shelf pyrometer.

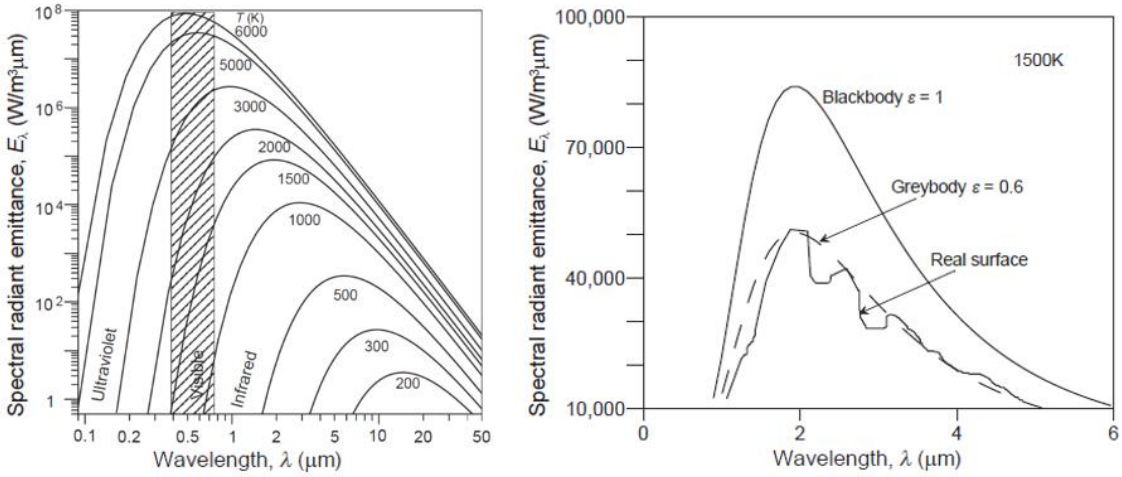

Figure 24. Blackbody emissive power against wavelength and relationship between a blackbody, a graybody and a real surface [77]

Figure 25 shows the two-colour temperature reading from the pyrometer during a welding experiment.

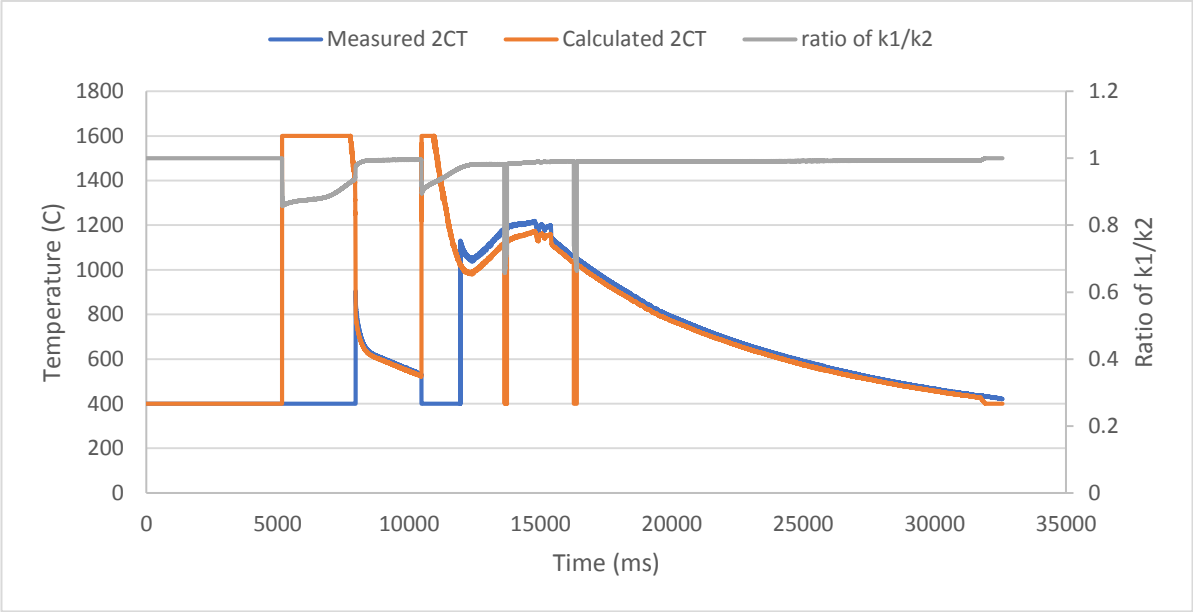

Figure 25. Comparison between the measured and calculated two-colour temperatures during a steel plate heating experiment (1600°C maximum temperature shown)

In this experiment, the pyrometer was fixed in position and a stainless-steel plate was heated with the welding torch. The calculated temperature is unrealistically high when the pyrometer provides no two-colour output. Figure 25 also shows that the pyrometer

output two-colour temperature is linked to the ratio between channels ***K1*** and ***K2***. When this ratio falls below 0.973, the pyrometer does not display two-colour temperature since it would be unrealistically high.

If the ratio between the two channel temperatures changes as the material heats up, the emissivity change across both wavelengths is not constant. The emissivity ratio therefore changes over time, affecting the calculation of the true two-colour temperature. Figure 26 shows the effects of this ratio on the calculation of the two-colour temperature.

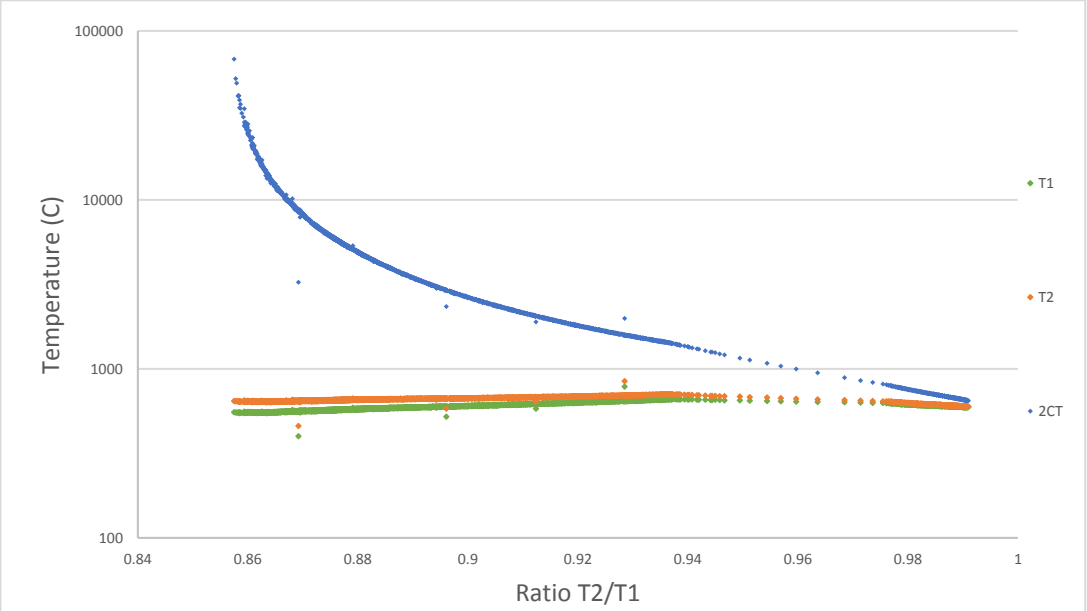

Figure 26. Relationship between two-colour temperature and the ratio of the individual pyrometer channels

Figure 26 shows that relatively small divergences between the individual channels can lead to drastic changes in the two-colour temperature. Absolute temperature measurement of objects with different emissivities across two wavelengths (bright and unoxidized metal surfaces) requires the emissivity ratio to be known [76]. However, selecting one ratio during a WAAM deposition process is not suitable due to the large temperature fluctuations and the formation of oxides. Figure 27 shows that single colour pyrometry follows a similar trend than the accurate two-colour temperature (ratio T2/T1 ≈ 1). In the region between T=11000s and T=12000s it can be seen that the two-colour temperature indicates that the part is cooling when in fact the part temperature was increasing. This erroneous cooling indication is due to the change in emissivity

across both wavelengths and would drastically impair the performance of a temperature control system. However, despite displaying a relative temperature, the single colour shows that the part is heating.

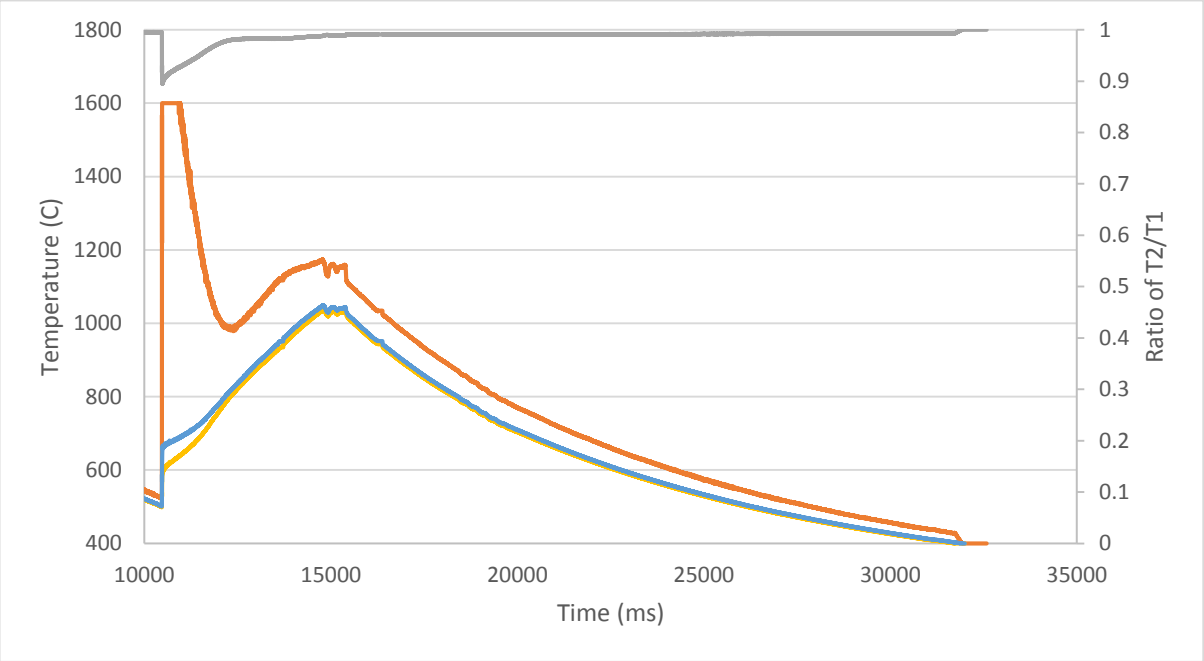

Figure 27. Comparison between two-colour and single colour temperatures recoded by the pyrometer during a steel plate heating experiment

Thus, since true two-colour temperature cannot be obtained with the current pyrometer, a single colour temperature was used for the development of the online control system. However, research in this area is still on-going and some research groups have managed to obtain absolute melt pool temperature measurements by selecting adequate wavelengths using high-speed cameras and filter arrangements [77].

1.6.2 Pyrometer Experiments

Once it was decided that a single colour temperature was to be used, experiments had to be conducted to identify the most adequate measuring position for online control.

Fixed point pyrometer

In this experiment, the pyrometer measured temperature at a single point while a layer was being deposited. The output data described the temperature changes at this point as the welding torch approached, went through, and moved away, from the measuring point. Figure 28 shows the data collected during a multi-layer process.

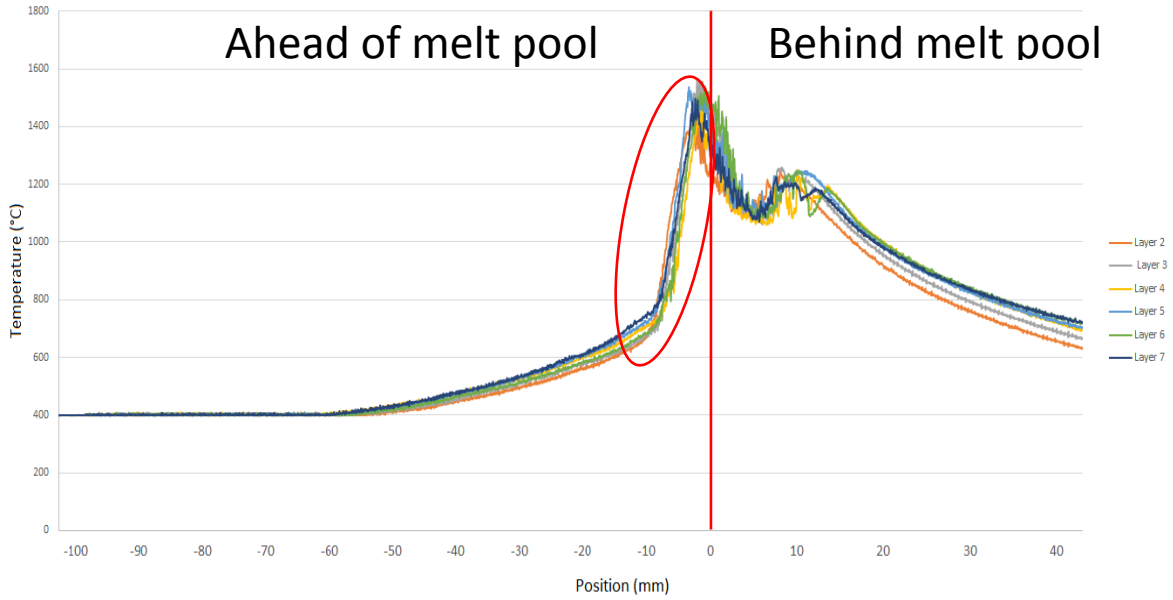

Figure 28. Relative temperature changes at a single spot as the welding torch moves through it during a multi-layer deposition experiment

Figure 28 shows a drastic temperature increase in front of the electrode tip (-10 mm). Interestingly, the rise in temperature at this location (indicated by the red circle) appears to be relatively constant with small variations across the layers, making it an ideal location for online control (see Appendix B for a graph representing a 12-layer experiment with offsets to identify individual layer trends). Behind the melt pool (10 mm) the temperature seems to change more across the deposited layers. As the number of layers increases, the heat transfer mechanisms change, and the part takes longer to cool down.

Figure 28 also shows a region of unexpected data approximately between positions -2 and 10 mm. This unexpected dip in temperature was presumed to be due to a drastic change in emissivity caused by a state change. To identify whether this area was in fact one of molten metal, the welding process was recorded with a CMOS camera and a thermal camera. Figure 29 shows that it is difficult to determine the size of the melt pool with a CMOS camera because of the unclear solidification boundary and oxidation. However, the thermal camera image clearly shows the area of presumed molten metal to have unrealistically low temperature. The agreement between the pyrometer readings and those of the thermal camera confirm that it is difficult to measure

temperature in this region due to changes in emissivity. Emissivity changes between solid and liquid states of the same material and its oxides has been previously reported in [78]. Thus, measuring in front of the melt pool would be more suitable for online control.

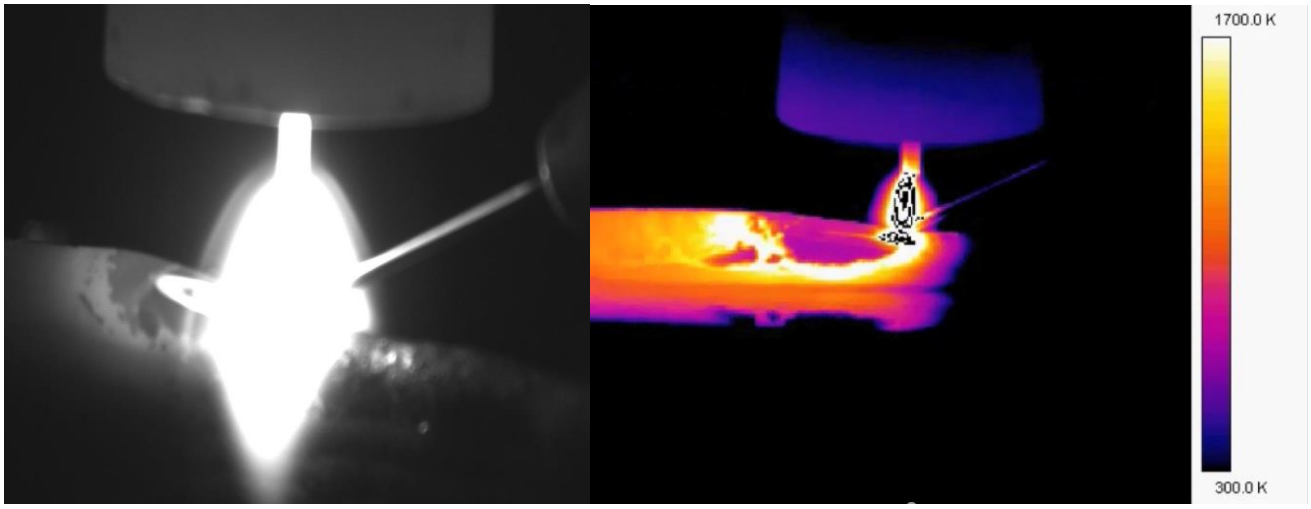

Figure 29. Melt pool imaging experiment with CMOS and thermal camera showing the area of molten metal as a "lower temperature area" during a multi-layer deposition process

Temperature measurement using a moving pyrometer

In this experiment, the pyrometer moved with the welding torch during the deposition process. The objective was to monitor temperature at different distances ahead of the electrode tip. Figure 30 shows that some of the torch/pyrometer configurations (i.e., the distance between the torch and pyrometer) do not seem to record the expected temperature rise at the end of the wall. The results showed that measuring 2 mm ahead of the electrode tip captures the drastic temperature increase data needed for online control.

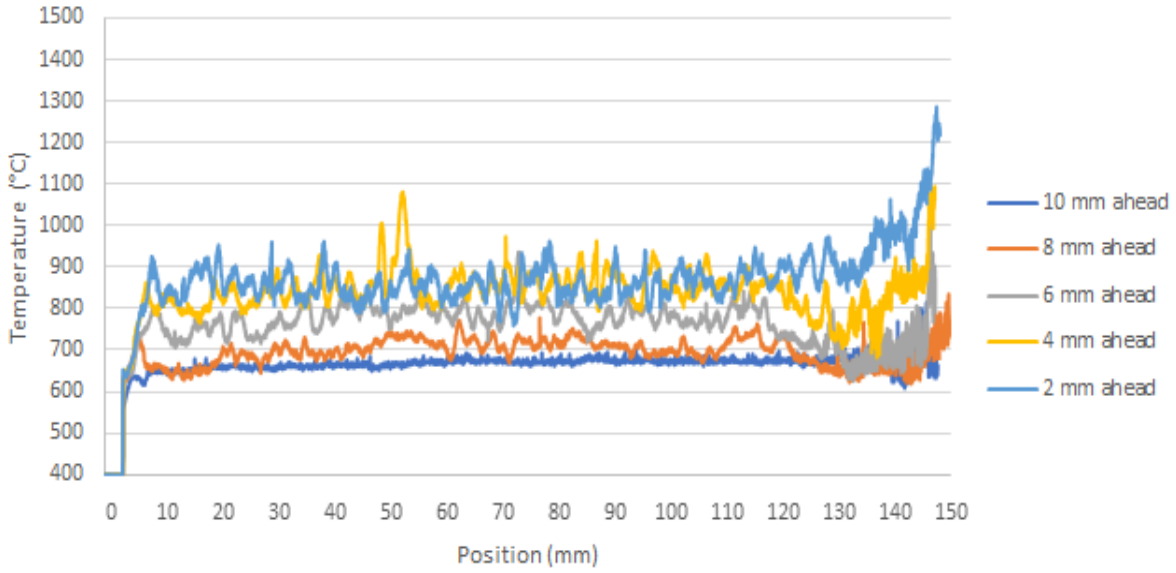

Figure 30. Temperature ahead of the melt pool at Layer 1 for different torch/pyrometer configurations. The configurations indicate the distance that the pyrometer is ahead of the welding torch (position 0 mm indicates the start of the wall and position 150 mm indicates the end of the wall)

Multilayer deposition temperature monitoring

In this experiment, temperature was recorded 2 mm ahead of the electrode tip (first configuration on Figure 30) during a multilayer deposition process. Figure 31 shows that unrealistically large temperature variations were recorded across the different layers. This may be explained in that, during multilayer deposition with no control systems, a predefined layer height is chosen. If the deposited beads do not all have this exact height, error is accumulated. The large temperature fluctuations result from the change in arc-length, changes in transfer mode, and changes in the pyrometer measuring position. Since the pyrometer is fixed to the Z stage, any variation in height will affect the output temperature. The lack of consistency in the temperature measurements across the layers renders the data unusable for online control.

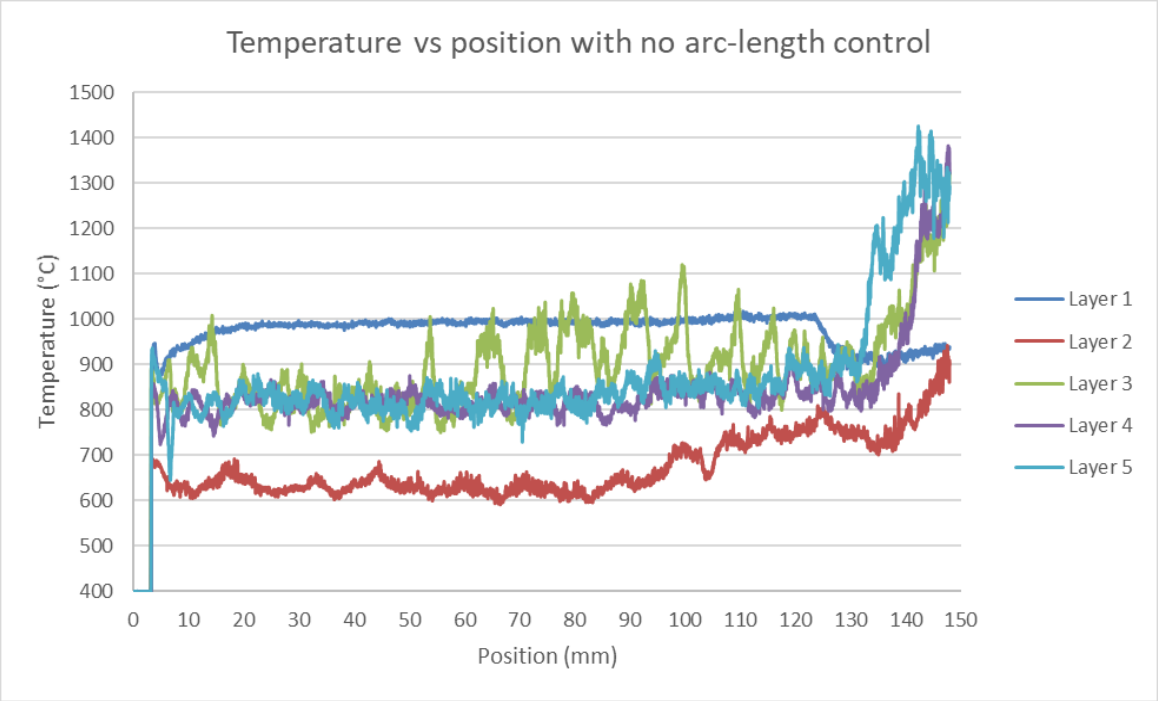

Figure 31. Temperature recordings 2mm ahead of the met pool of a multilayer deposition process (position 0 mm indicates the start of the wall and position 150 mm indicates the end of the wall)

The change in transfer mode and arc-length were recorded with the CMOS camera. Figure 32 and Figure 33 display three pictures that show the transfer mode at the start, middle and end of the wall for layers 3 and 10. In other words, Figure 32 and Figure 33 show snippets of the videos recoded with the CMOS camera. Note, that layer 1 had a bridging transfer mode (the ideal transfer mode).

Layer 3:

Figure 32. Layer 3 transfer mode during a multilayer deposition process at the start (left image), middle (centre image) and end of the wall (right image).

Layer 10:

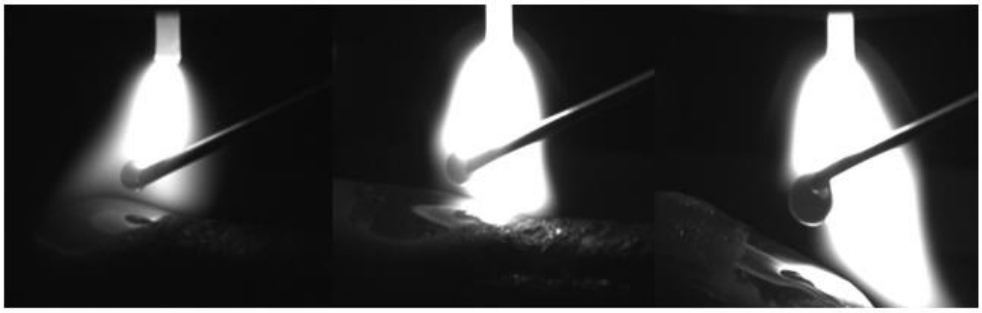

Figure 33. Layer 10 transfer mode during a multilayer deposition process at the start (left image), middle (centre image) and end of the wall (right image).

The open loop bead height system is rather unforgiving and requires constant operator adjustments to prevent collisions between the welding electrode and the wall. Also, there is a risk of molten metal spatter if the arc-length increases from one layer to the next. Figure 34 shows an example of a 9-layer wall created with no arc-length control; Figure 35 shows a side view of the created part, it represents the profile of the wall by displaying its height at different X positions.

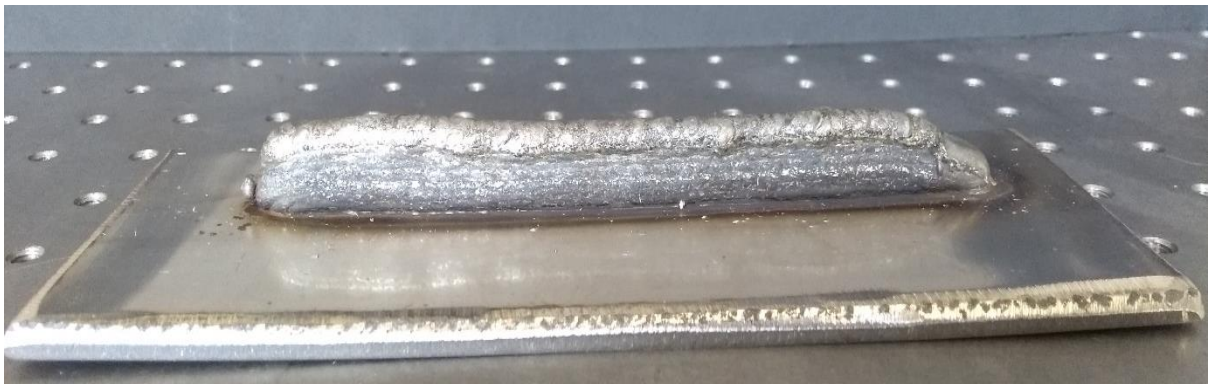

Figure 34. A 9-layer wall created with no arc-length control

Figure 35. Wall height progression with no arc-length control. The lines indicate the profile of the wall as the build progresses (position 0 mm indicates the start of the wall and position 150 mm indicates the end of the wall)

The results suggest that any temperature control system based on temperature recordings taken during a multilayer deposition procedure in which neither the arc-length nor the bead height is controlled is likely to fail.

1.7 Development of an arc-length control system

An arc-length control system capable of taking consistent temperature measurements while maintaining a constant transfer mode was successfully developed. With this system, the deposited beads are scanned before the next layer is deposited. The recorded data are used to plan the next deposition. The arc-length control system changes the Z stage position to maintain a constant distance between the electrode tip and the weld bead. A predefined layer height is no longer required since the weld torch follows the shape of the previously deposited bead (Figure 36).

Figure 36. The developed arc-length control system following the shape of a test bead

Since the pyrometer is mounted on the Z stage, if the arc-length is controlled, then the pyrometer's measuring position and the transfer mode will remain constant even if the wall has severe geometrical inaccuracies. Figure 37 shows the temperature recorded 2 mm ahead of melt pool during a multilayer deposition process using the developed arc-length control system.

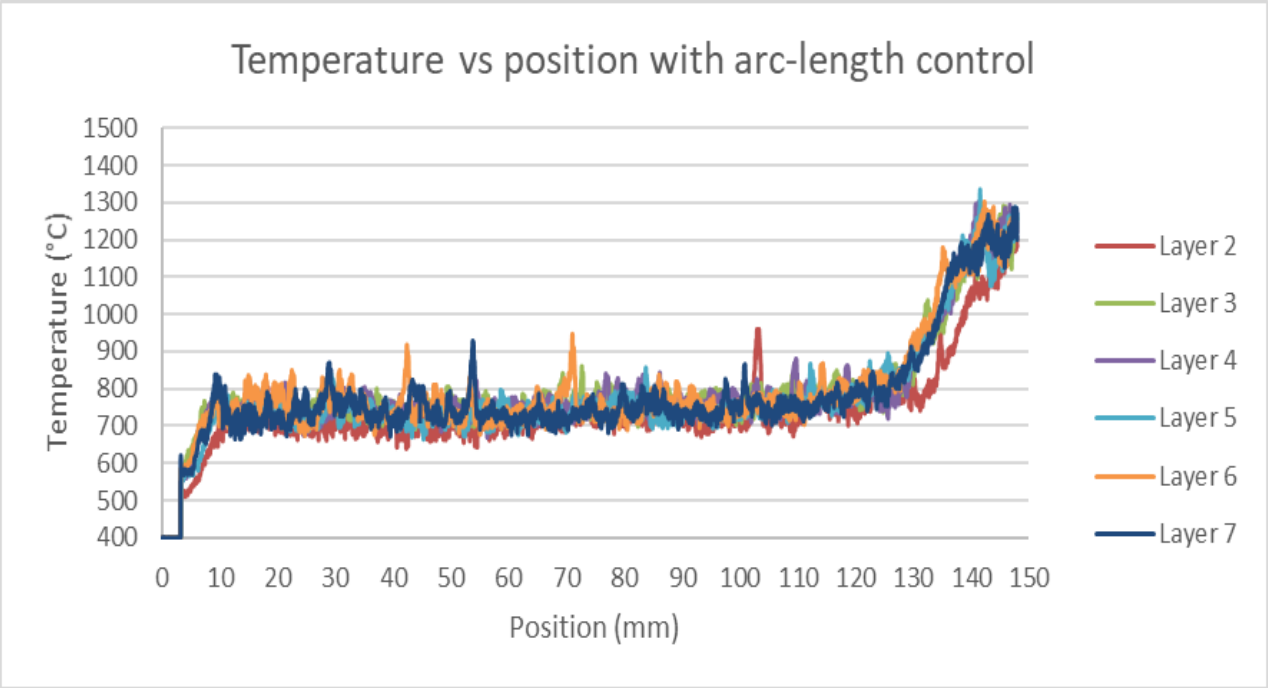

Figure 37. Temperature measurement 2 mm ahead of the melt pool during a multi-layer deposition process when using the arc-length control system (position 0 mm indicates the start of the wall and position 150 mm indicates the end of the wall)

Figure 37 shows that, with the developed system, the previously recorded large temperature fluctuations between one layer and the next are eliminated; temperature measurements are consistent, making online control possible. However, despite the obvious improvement, the use of a one channel pyrometer leads to a noisy signal. In layer 6 and 7 the 200°C spikes in the recorded temperature were likely caused by oxide islands with different emissivities. Because most oxides float to the top, the oxide island formation is a cumulative process. This accumulation might explain the increase in signal noise at the higher layer numbers. This means, that to obtain better data, oxidation monitoring and mitigations techniques should be introduced (See Chapter 3). This further reaffirms the hypothesis that to develop a successful control systems in metal-based AM processes, it is likely that multiple independent or multi-input-multi-output control systems have to be used.

The noise in the single channel temperature recordings could also be explained could also be explained by temporary signal attenuations caused by metal vapour fumes or smoke in the line of sight. These temperature fluctuations could be removed with the

use of a two-colour pyrometer. **Figure 38** shows how the signal attenuation induced errors are eliminated.

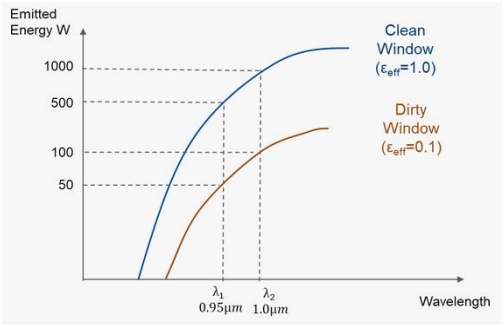

$$\frac{W_1(\lambda_1)}{W_2(\lambda_2)} = \frac{1000 \text{ energy units}}{500 \text{ energy units}} = 2 \rightarrow 1500°C$$

$$\frac{W_1(\lambda_1)}{W_2(\lambda_2)} = \frac{100 \text{ energy units}}{50 \text{ energy units}} = 2 \rightarrow 1500°C$$

Figure 38. Example of signal attenuation error mitigation by a two-colour pyrometer [79]

In this example the signal attenuation is caused by a dirty window. The reduction of energy received by the pyrometer would certainly affect the temperature recordings of a single colour pyrometer. However, assuming that the obstruction reduces the signal across two wavelengths equally, a two-colour pyrometer could be used to provide an accurate temperature reading. Two-colour pyrometer manufacturers state that even with a signal reduction of 95%, a two-colour pyrometer would still provide accurate temperature readings [79].

Although a working two-colour pyrometer would provide better results, the data obtained with obtained with a single-colour pyrometer and the arc-length control systems is adequate for an online temperature control system. The two-colour pyrometer used for this experiment was not able to provide sensible data due to the changes in emissivity ratio across both wavelengths. Despite the noisy signal, the single colour pyrometer provides usable data where the tested two-colour pyrometer does not. Further experiments show that a steady state is reached and that noise filtering techniques could be used to improve the recorded data. A 10-point mean was used to filter the signal from the pyrometer.

The arc-length control system was also able to maintain a constant transfer mode. The CMOS camera images clearly show that a constant deposition mode was maintained throughout the entire build process (Figure 39 and Figure 40). Again, Figure 39 and Figure 40 display three pictures that show the transfer mode at the start, middle and end of the wall for layers 3 and 10

Layer 3:

Figure 39. Layer 3 transfer mode when using the arc-length control system during a multilayer deposition process at the start (left image), middle (centre image) and end of the wall (right image).

Layer 10:

Figure 40. Layer 10 transfer mode when using the arc-length control system during a multilayer deposition process at the start (left image), middle (centre image) and end of the wall (right image).

For DED processes, the way in which the material is added affects the quality of the weld beads formed. As reported in [80] [81] [82] [83], the wire/powder feeder setup is one the most influential factors affecting process stability [16]. Because the wire feeder is mounted on the Z stage, once the ideal wire tip location has been experimentally found, the arc-length control system will fix this location for the entire build process. Figure 41 shows an example of the layer progression achieved for a 10-layer wall using the developed arc-length control system. Figure 42 and Figure 43 show examples of higher multilayer walls.

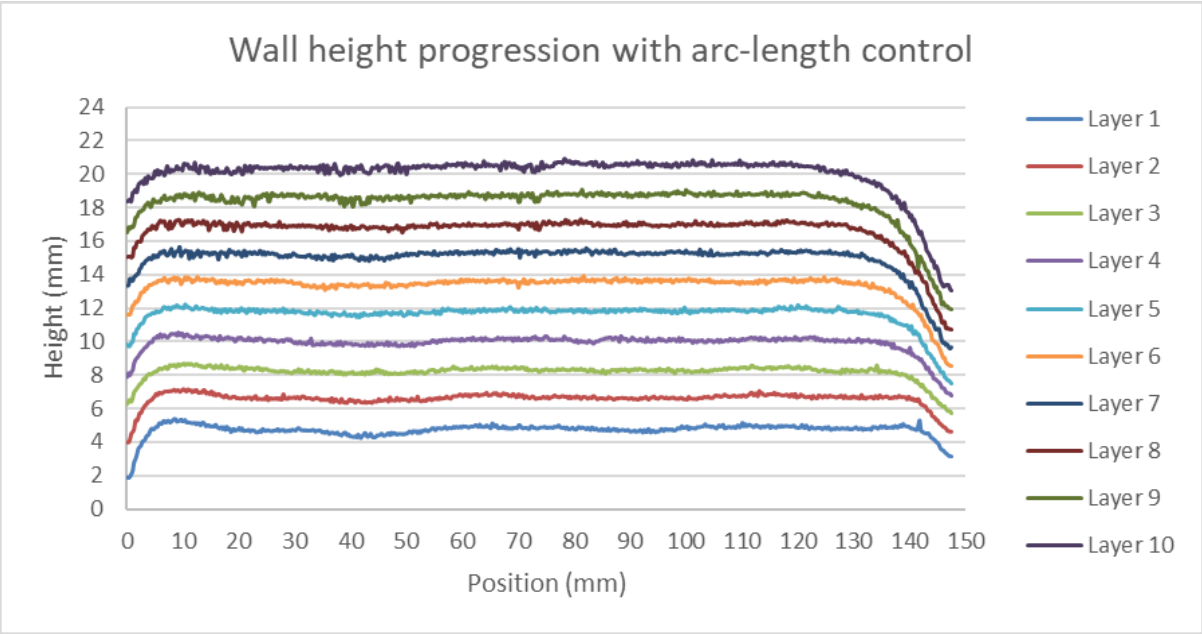

Figure 41. Wall height progression with arc-length control . The lines indicate the profile of the wall as the build progresses (position 0 mm indicates the start of the wall and position 150 mm indicates the end of the wall)

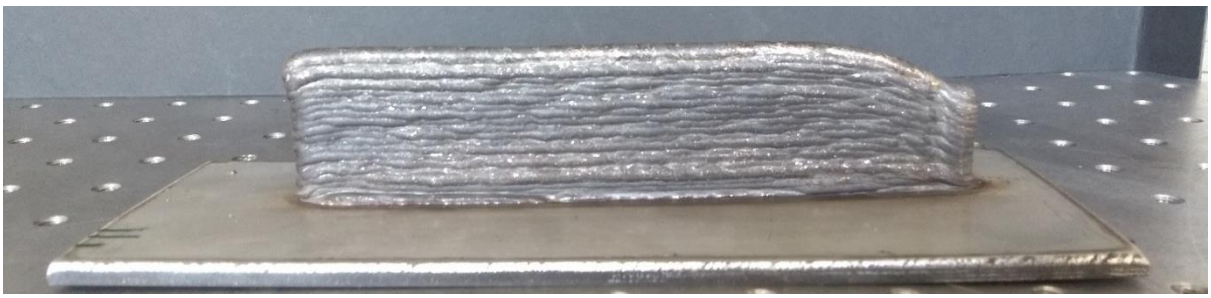

Figure 42. 15-layer wall deposited using the arc-length control system

Figure 43. 30-layer wall deposited using the arc-length control system

The developed arc-length control system allows for drastic improvements in layer progression consistency and part appearance. Further, the process is completely automatic; it requires no operator to adjust parameters during the build process. Figure 44 show an example of a deposition error correction over three layers with the arc-

length control system (see section 2.7.1 for error correction experiments with the arc-length control system).

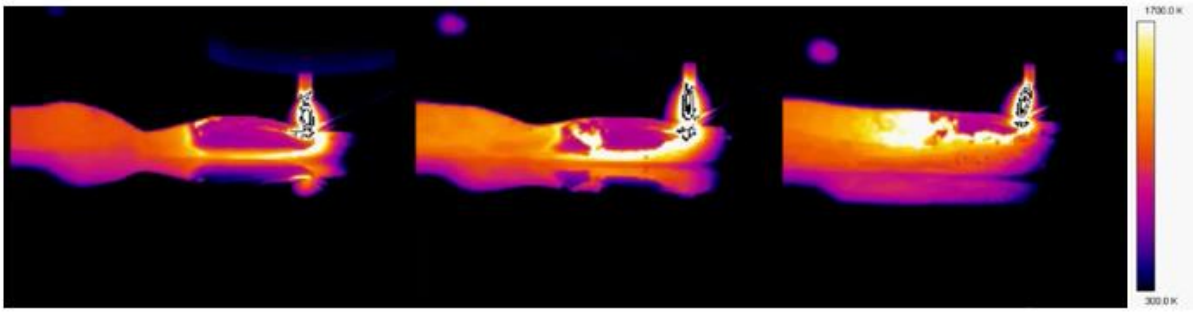

Figure 44. Error correction example with the arc-length control system over 3 layers (Layer 1 – left image, Layer 2 – middle image, Layer 3 – right image)

Figure 45 shows how switching-off the arc-length control system during the process affects temperature measurements.

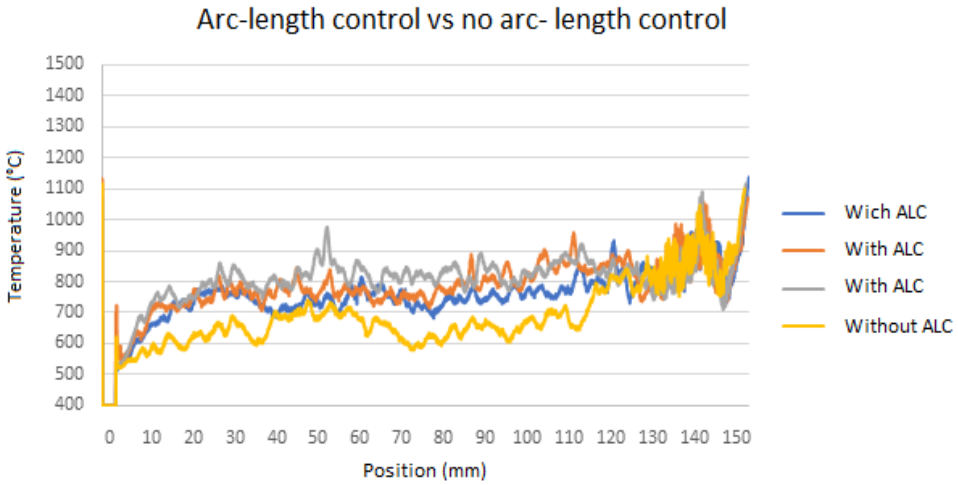

Figure 45. Effect of switching off the arc-length control system during a multi-layer deposition process (the arc-length control is switched off at layer 4)

In conclusion, the arc-length control system greatly increases process stability and allows for consistent temperature measurements. The results obtained indicate that no successful temperature control system is possible without an arc-length control. A bead height control system would also improve temperature measurements. However, to obtain the same level of consistency, the bead height control system would have to be very accurate. Any deviation in layer height would affect the temperature measurement and the transfer mode. The developed arc-length control system, which provides control

in a relatively simple manner, could easily be integrated with other existing control systems.

1.7.1 Error correction experiments

The increased stability of the deposition process with the arc-length control system appeared to be partly due an error correction advantage arising from the constant transfer mode. This hypothesis was formulated following the experiment shown in Figure 46.

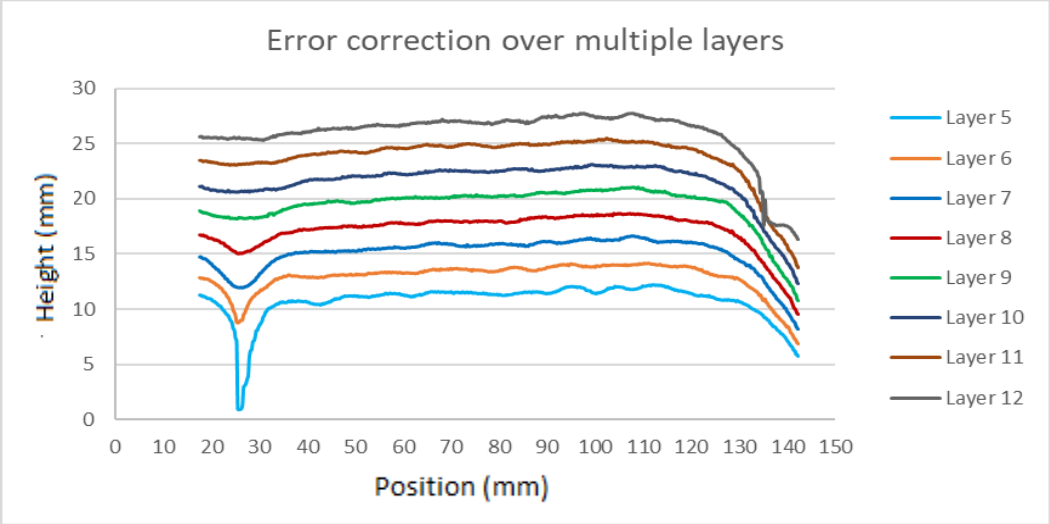

Figure 46. Error correction example with the arc-length control system over multiple layers. The lines indicate the profile of the wall as the build progresses (position 0 mm indicates the start of the wall and position 150 mm indicates the end of the wall)

Figure 46 shows that approximately a 10 mm error was corrected over 5 layers. To test if in fact the process was correcting errors that would have previously halted the deposition process, a number of experiments were devised.

In these experiments, three-layer walls were created with the arc-length control system. The test walls were removed from the welding bed and a known error was introduced with a milling machine at layer 3. Figure 47 shows an example wall with an introduced 2.2mm error.

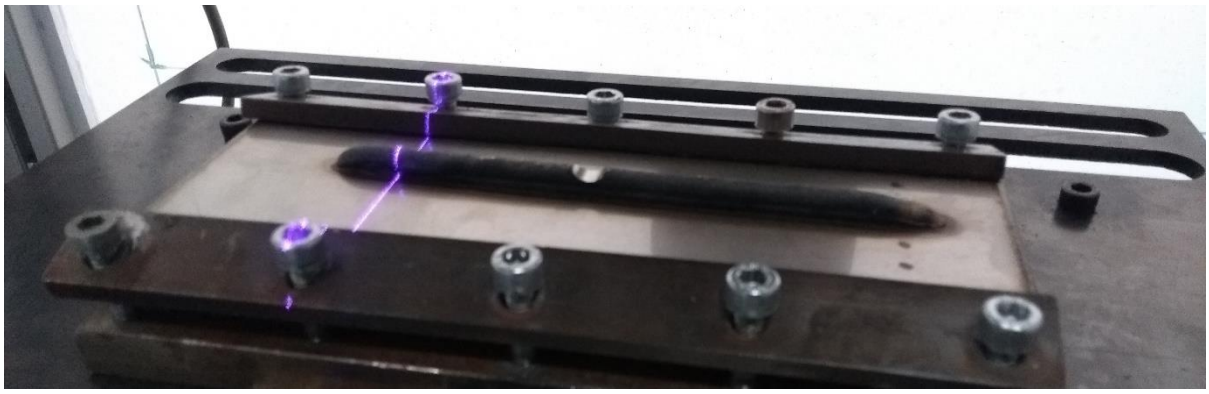

Figure 47. Error correction experiment with a known introduced error.

The walls with the introduced errors were then scanned Micro Epsilon 3D laser scanner. For the experiment with no arc-length control the average height of the third wall was used to select the ideal location of the torch (average 3rd layer height + 3.5 mm). This ideal case provides the best possible torch position for an uncontrolled process, since in a normal deposition, the error arising from the pre-selection of the layer height would have likely been significant enough to introduce a globular transfer mode. Figure 48 shows the wall height progression of an uncontrolled process after the know error was introduced.

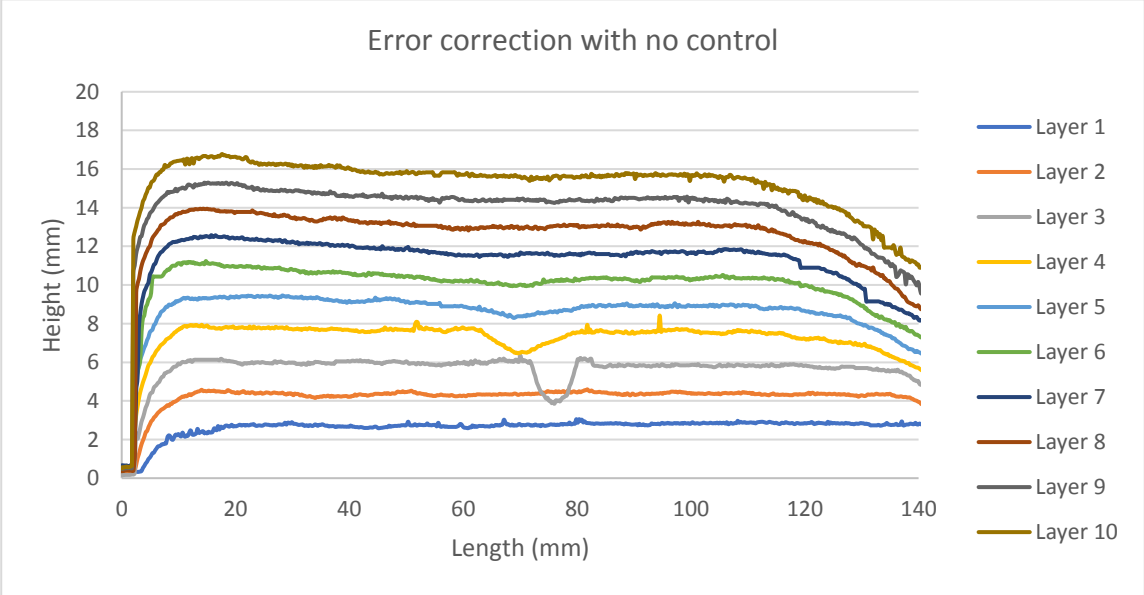

Figure 48. Small introduced error correction with no arc-length control. The lines indicate the profile of the wall as the build progresses (position 0 mm indicates the start of the wall and position 150 mm indicates the end of the wall)

Figure 49 shows the wall height progression with arc-length control.

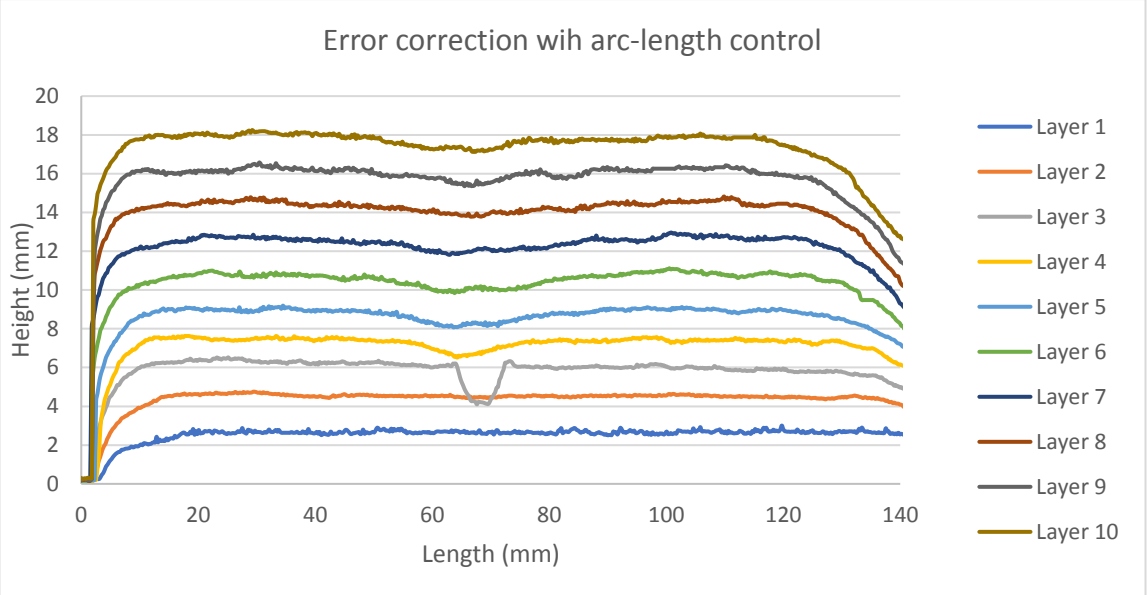

Figure 49. Small introduced error correction with arc-length control. The lines indicate the profile of the wall as the build progresses (position 0 mm indicates the start of the wall and position 150 mm indicates the end of the wall)

Figure 48 and Figure 49 show that the are no significant differences between the error correction layer progression of an uncontrolled and a controlled process. This conclusion is only true in the best possible scenario, where the introduced error appeared relatively early (layer 3) and there was no layer height error accumulation. A further experiment with a larger error re-affirmed this conclusion (See Figure 50, Figure 51 and Figure 52). However, in a non-ideal situation were the error is introduced at a later stage, it is likely that the accumulation of bead height error would be too great to fix the deposition problem. For example, if during an uncontrolled build a deposition error occurs at layer 10, it is more than likely that the transfer mode and the unstable arc-length would not be able to amend the defect. In fact, the most likely scenario would be that the metal is not deposited, and spatter falls on the substrate. These conclusions also hold true, in areas with geometrical inaccuracies induced by heat accumulation. If an error was introduced at the end of the wall, the uncontrolled process will not be able to amend the defect.

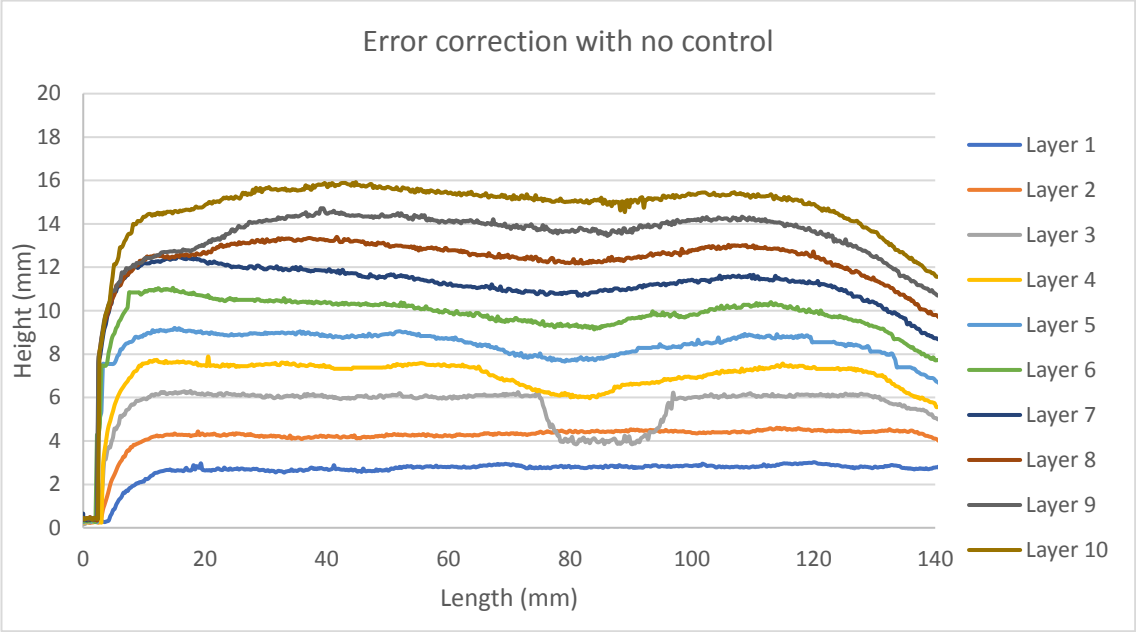

Figure 50.Large introduced error correction with no arc-length control. The lines indicate the profile of the wall as the build progresses (position 0 mm indicates the start of the wall and position 150 mm indicates the end of the wall)

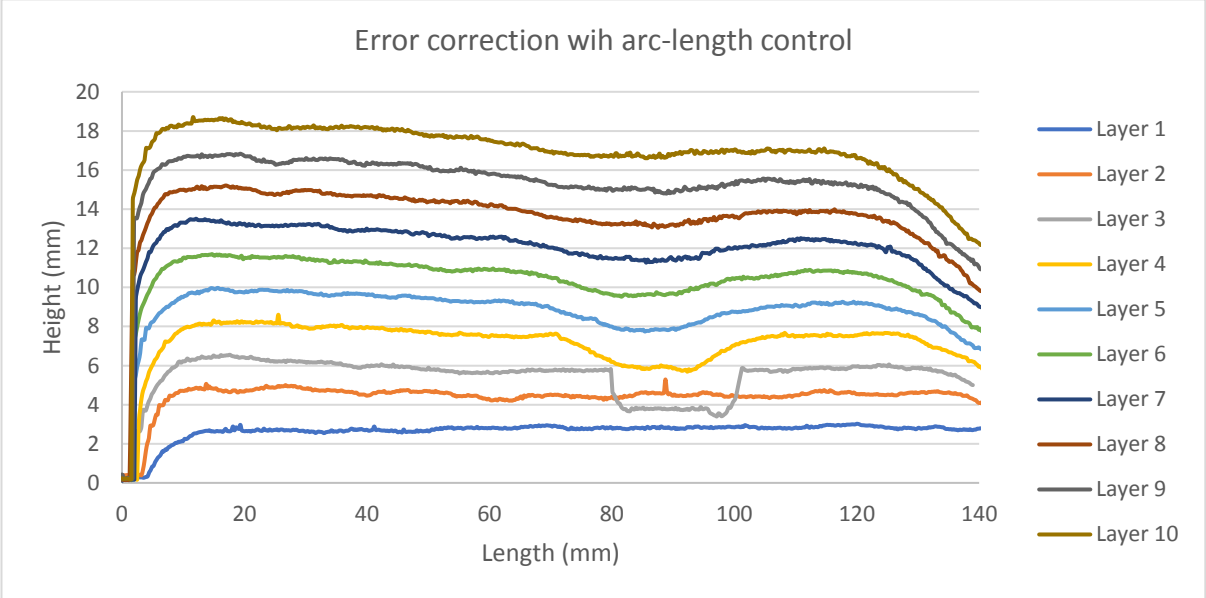

Figure 51. Large introduced error correction with arc-length control. The lines indicate the profile of the wall as the build progresses (position 0 mm indicates the start of the wall and position 150 mm indicates the end of the wall)

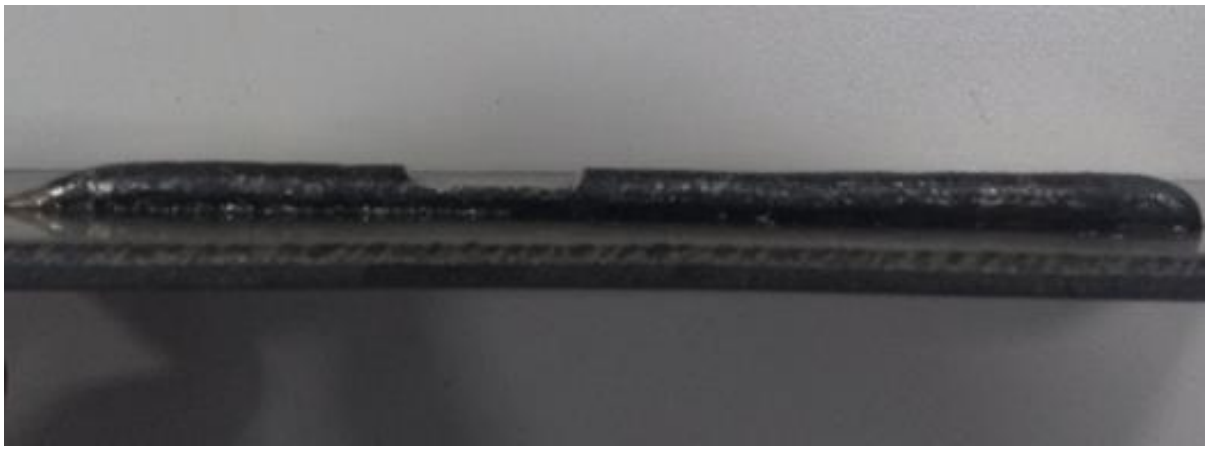

Figure 52. Example of a three-layer wall with a large introduced defect

1.8 PID temperature control system

Once consistent temperature readings for the build process were obtained, a preliminary PID temperature control system was developed to maintain the melt pool temperature by adjusting the current. The purpose of developing this experimentally tuned PID was to modify the controlling software to allow for installation and testing of different controls systems. This experimental PID system highlighted some of the challenges that need to be tackled to create more complex control systems in the future.

The temperature 2mm ahead of the melt pool was set as the process variable. The single colour pyrometer was used to measure the process variable. Following the temperature recording experiments with the arc-length control system, a setpoint of 725°C was chosen. The aim of the control system was to maintain that temperature through the entire deposition process. The error of the system is difference between 725°C and the pyrometer measurements. This control system attempts to reduce the error by changing current. The change in current is determined by the control system algorithm.

A Proportional-Integral-Derivative (PID) control is by far one of the most common control algorithms used in industry and has been universally accepted in industrial control [84] [85]. PID control systems have gained popularity due to their robust performance and their relatively simple operation [84]. The simplicity of a PID means that it can be operated with a few empirical rules [85]. Most of the practical feedback loops in industry are based on PID control or some variations of it. In fact, many of the industry controllers don't even use the derivation action [85]. In metal based-AM an experimentally tuned PI controller was used by Heralic to control melt-pool width [46].

PID algorithms consists of three basic coefficients (proportional, integral and derivative) that are varied to obtain an optimal the response. The standard version of a PID controller is defined as [85]:

$$u(t) = ke(t) + k_i \int_0^t e(\tau)d\tau + k_d \frac{de}{dt}, \tag{6}$$

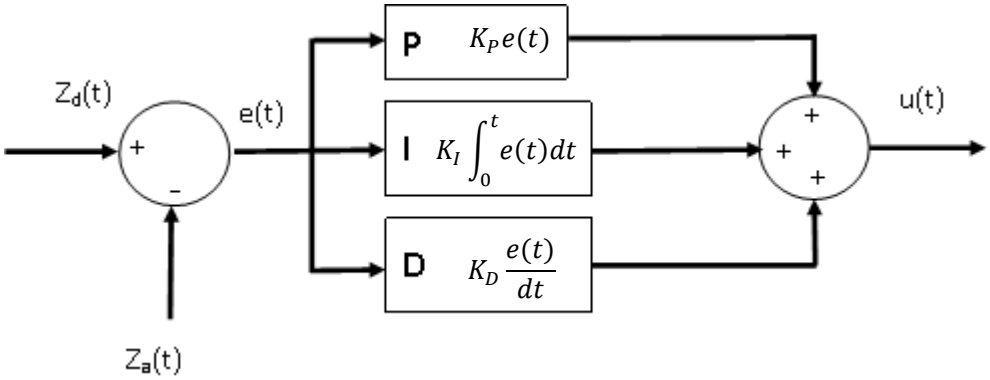

Figure 53. Example PID loop

where ***u*** is the control signal and **e** is the error. The control signal is a sum of the three terms **P**, **I** and **D.** The term **P** is proportional to the error, the term **I** is proportional to the integral of the error and the term **D** is proportional to the derivative of the error [85].

The proportional gain ***K*** determines the output response to the error. For example, if the error is 10 and the proportional gain is 5 the response of the system will be 50 [84]. Increasing the proportional gains will increase the response of the system. However, as the proportional gain is increased, the system becomes more oscillatory and the likelihood of overshooting increases. The typical response of a PID control system with a proportional gain ***K*** too large is an unstable oscillation [84].

The integral term k_I sums errors over time. A small error over time will cause the integral component to increase. This integral component will increase unless the error is 0. The aim of the integral term is to eliminate steady state errors [84]. For example, if a hypothetical control system had reached a steady state with a constant control signal and a constant error ($e_0 \neq 0$), then from Equation 6 it can be seen that:

$$u_0 = ke_0 + k_i e_0 t. \qquad \text{(Eq. 7)}$$

The left term of the equation will remain constant but right-hand side is a function of time. To have a constant control signal output, the error must be equal to 0 [85]. Figure 54 shows the steady state error reduction with the addition of the integral gain.

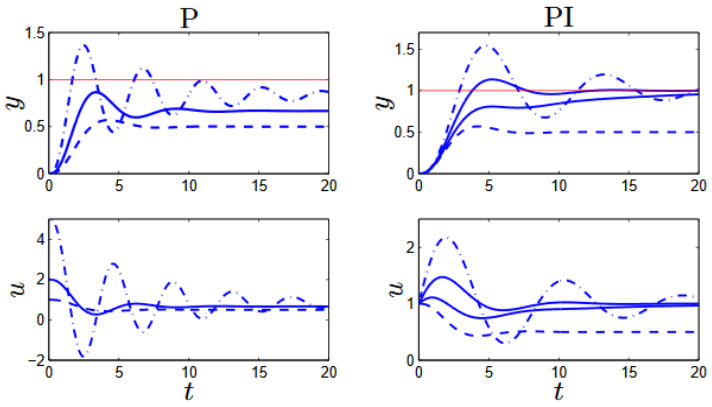

Figure 54. Example comparison between a proportional control system and a PI control system [85]

In this example, the system has a transfer function P(s) = 1= $(s+1)^3$. The controller parameters are k=1(dashed), 2 and 5 (dash-dotted) for the **P** controller. For the **PI** controller the proportional gain is set at 1 and the integral gain is changed between 0 and 1 (k_I= 0 (dashed), 0.2, 0.5 and 1 (dash-dotted)) [85]. Figure 54 shows that a control system with a proportional gain K=1 and integral gain K_I = 0 (a purely proportional control) will reach a steady state error. The same control system with a value of K_I = 0.5 will slowly reduce the error and with a value of K_I = 1 the system will overshoot but the reduction of error will be quicker. Increasing the integral term makes the system more oscillatory and can lead to a phenomenon called *integral windup*. When this occurs, the integral action saturates the controller and the signal is not driven towards 0 error [84].

The derivative term $\boldsymbol{k_D}$ reduces the output if the process variable is increasing rapidly. Thus, the derivative response is proportional to the rate of change of the process variable [84]. If the derivate term $\boldsymbol{k_D}$ is increased, the system will react more vigorously to rapid changes in error, increasing the overall response of the system. A controller with a proportional and a derivate term can be interpreted as a controller that is made to react proportionally to the predicted process output [85]. Figure 55 compares the previously described **PI** control system with a **PID** system.

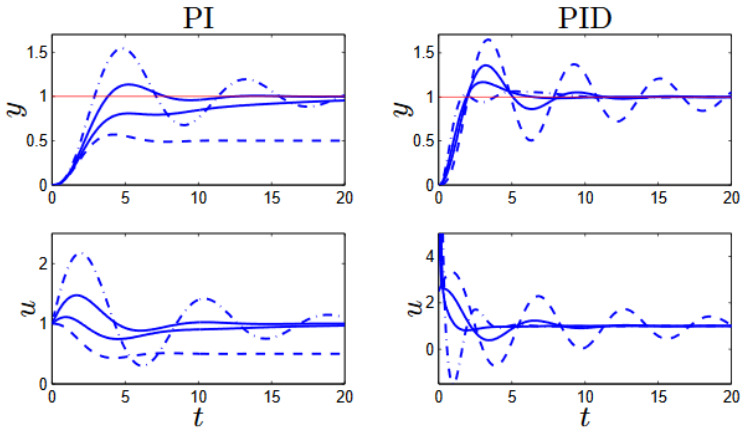

Figure 55.Comparison between a PI control system and a PID control system [85]

In this example, the controller parameters for the PID system were **k** = 2.5, $\mathbf{k_I}$= 1.5 and the derivative term was changed between 0 and 4 ($\mathbf{k_D}$= 0 (dashed),1, 2, 3 and4 (dash-dotted). Figure 55 shows that the addition of the derivative term dampens the overshoot and reduces oscillatory tendencies [85]. Practical systems tend to have small derivate gains because the response is highly sensitive to noise. If the term $\mathbf{k_D}$ is too high and loop rate is too slow, a noisy temperature reading could result in an unstable control system. This may explain why Heralic et al decided to only use a **PI** controller and why Salehi used a relatively small $\mathbf{k_D}$ factor for controlling a metal-based additive manufacturing process [46] [68]. In industry, tests are normally conducted to identify if only **P**, **PI** or **PD** control systems can be used. For a GTAW-DED temperature control, the closed-loop feedback mechanism (pyrometer) must have an adequate sample rate.

1.8.1 PID tuning

As highlighted in the literature review, most of the studies investigating control systems for DED processes concluded that the dynamic response of the system could be approximated to a first order transfer function. This conclusion was reached after performing step response experiments and observing a lack of overshoot [34] [46] [3] [26] [28] [29] [31] [46] [26]. The relative simplicity of a first other system allows for the use of non-parametric methods of tuning. Normally most control systems used in first order plants are only proportional control systems because they are easy to implement [86]. PID control systems are normally used to control second or higher order systems [86].

Tuning a PID control system involves manipulating the terms **k**, $\mathbf{k_I}$ and $\mathbf{k_D}$ to obtain the desired response from the control system. Multiple experimental methods exist for non-parametric tuning of control systems such as the Cohen-Coon and Ziegler Nichols methods. The Cohen-Coon system can only be used for first order systems and the more popular Ziegler Nichols can be used for any system. The developed temperature control system was developed using a combination Ziegler Nichols system and a purely experimental method.

The Ziegler Nichols method was developed in the 1940s and it's still one of the most common methods of tuning a PID system. The idea behind the method is simple – conduct an experiment to determine features of dynamic system and determine the controller parameters from the data extracted [85]. The Ziegler Nichols method involves increasing the proportional term **k** until the loop oscillates. Once the system is oscillating, the critical gain **k** ($\mathbf{k_c}$) and the period of oscillations $\mathbf{P_C}$ are recorded [84]. The rest of the terms are determined using Table 4.

Control	k	k_I	k_d
P	0.5Kc	-	-
PI	0.45Kc	Pc/1.2	-
PID	0.60Kc	0.5Pc	Pc/8

Table 5. Ziegler Nichols oscillation method of tuning parameter table [85].

The Ziegler Nichols experiment provided the approximate values used for manual tuning of the control system. However, further experimental tuning was needed to improve the response of the system. For a first order system, once the significance of each of the gain parameters is understood, manual tweaking of the controller gains is relatively easy [84]. However, an experimental procedure has to be followed. The proportional gain is modified to obtain a small overshoot and an adequate response time. The integral term is increased to stop the oscillations induced by the proportional term. The integral is then tweaked to achieve the minimal steady state error. Once the **PI** terms are obtained, the derivative term is increased until the response is adequate [84]. For the temperature control system, the derivative term was increased with caution since the

literature suggests that the noisy signal from the pyrometer could drastically affect the performance of the control system.

1.8.2 LabVIEW PID implementation

The LabVIEW PID control pallet was also used to further improve the response of the system. Figure 56 shows some of the options available to help with the development of the temperature control PID.

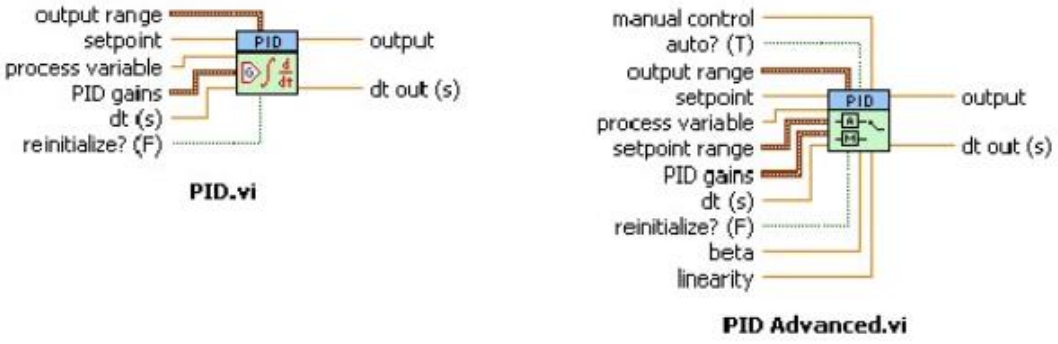

Figure 56. LabVIEW PID toolset used to further improve the control system [84]

The output range can be set to minimise the possible overshoot of the system. For the developed GTAW-DED machine, it was experimentally established that minimum current should be 120A and the maximum 150A. The minimum current setting ensures that there is enough energy input to maintain the desired transfer mode. The maximum current ensures that the produced part does not collapse due to an excessive energy input. The program was also developed to allow for a change in the output range for every layer deposited according to the data collected from previous experiments. For example, the user might determine that in the first layer the current should be between 140-150A to maintain the setpoint temperature and that at layer 10, the current should be between 120-130A. The programming essentially allows for optional additional process information that may help the control system to maintain a stable temperature. Following the conclusions from the literature, the LabVIEW program was developed to easily accommodate a feed forward control system.

A PID autotuning program was also developed to improve the response time. Figure 57 shows the LabView pallet available to automatically tune PID control systems [84]. Once approximate figures for the control system parameters are obtained, the auto-tuning

program was used to further optimize the control. However, the results obtained from the auto-tuning program were trivial.

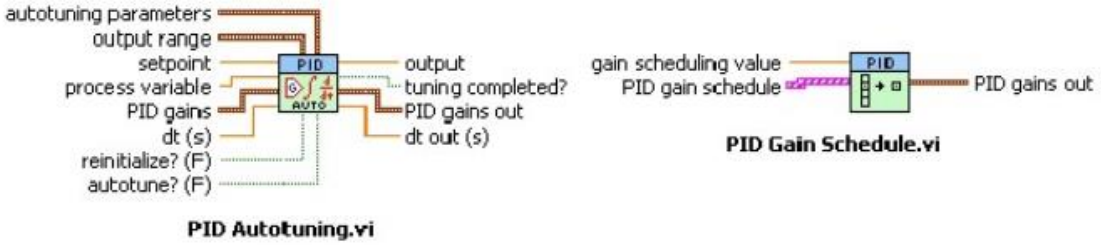

Figure 57. LabVIEW PID auto-tuning tool pallet used [84]

1.8.3 PID experiment results

Figure 58 shows how the PID system changes the current to maintain a temperature of 725°C.

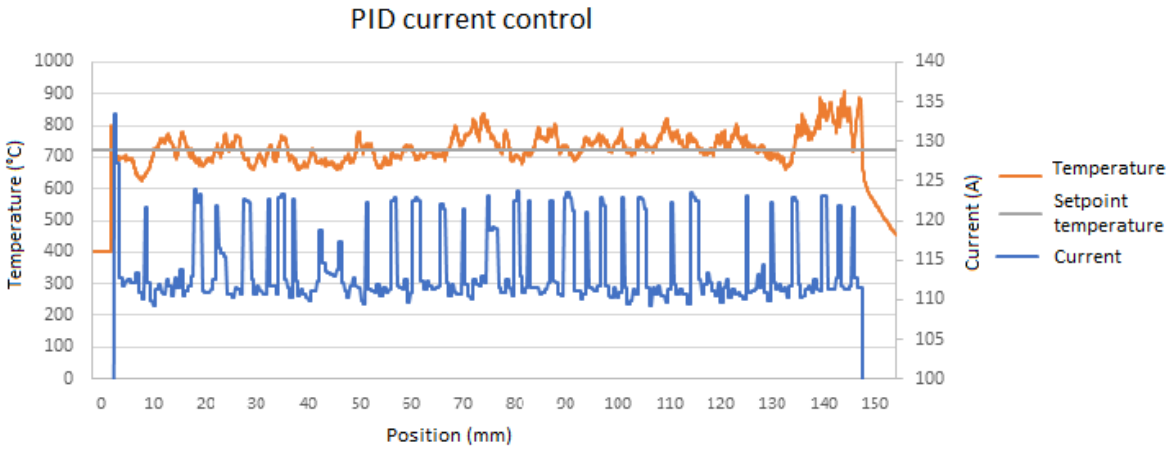

Figure 58. Single layer temperature control by changing current using the preliminary PID temperature control system (position 0 mm indicates the start of the wall and position 150 mm indicates the end of the wall)

Figure 59 shows the temperature readings taken 2 mm ahead of the electrode at different positions along the developing wall, using arc length control and the PID system.

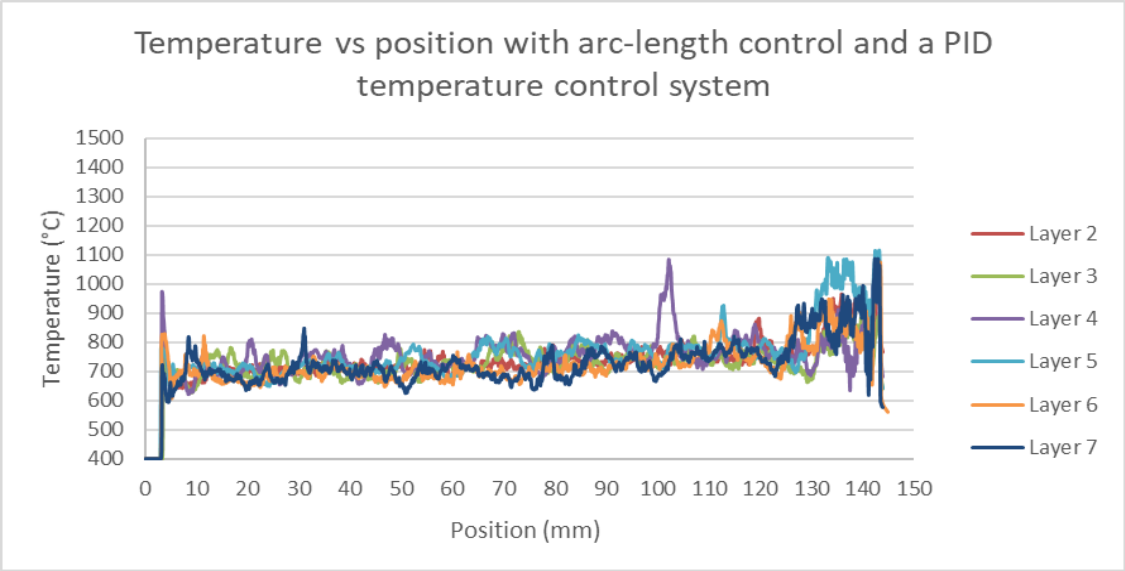

Figure 59. Temperature readings of a multilayer deposition process with the preliminary PID system set to maintain a temperature of 725°C (position 0 mm indicates the start of the wall and position 150 mm indicates the end of the wall)

The results show that only a mild improvement was obtained with the PID system. At the end of the wall, peak temperature was consistently reduced by approximately 200°C when compared to the temperatures obtained without the PID control system (see Figure 31). However, the temperature was still high enough to produce visible deformations; the appearance of the finished wall was therefore similar to that of a wall produced using only arc-length control. Figure 60 shows an example of the layer height progression during a multilayer deposition process with arc-length control and PID temperature control .

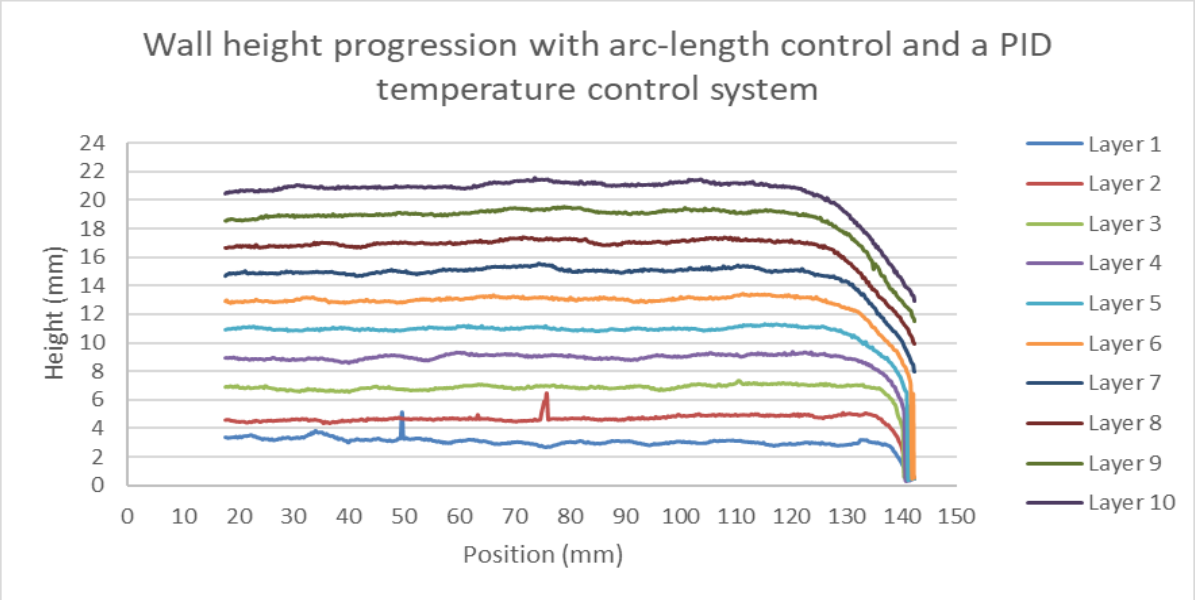

Figure 60. Layer height progression with arc-length control and the preliminary PID control system. The lines indicate the profile of the wall as the build progresses (position 0 mm indicates the start of the wall and position 150 mm indicates the end of the wall)

The results indicate that a PID temperature control system is potentially suitable for maintaining a constant temperature in the areas where there are no significant changes in heat transfer mechanisms. However, a fully calibrated control system with experimentally obtained relationships between current and temperature will be required if better results are to be obtained. Even though a 200°C peak temperature reduction was achieved with the PID, a drastic temperature increases still occurred at the end of the wall and the temperature induced geometrical defects were still present. These results indicate that a feedforward control system is probably required to maintain a stable temperature in those areas where the heat transfer mechanisms change. Further calibration experiments are required to identify the relationships between the parameter settings and the bead outcomes (e.g. d{***h,T,w***)/d{***P,Vs,Vw***}). Once these relationships are obtained, a more comprehensive PID system could be developed. The degree of success of the new PID system will show whether a feed-forward control system is required. Despite the possible improvements that could be implemented from further calibrations experiments, this relatively simple PID system was able to improve the overall temperature stability of the system and managed to

reduce peak temperatures. Further, the development of this PID has established the framework and the control program structure required to accommodate experimentally found relationships.

Future work might indicate that simply changing the current will be insufficient to control the temperature, and that additional independent or multi-input-multi-output control systems might be required. A new approach for equalizing the heat transfer mechanisms during a GTAW-DED deposition is explored in Chapter 5.

Further experiments might also indicate that even if a constant temperature is maintained, the deformations at the end of the wall will still be apparent. Although it is likely that these deformations will reduce, the way in which the material added, and the flow of the melt pool can also affect the shape of the deposited beads - at the end of the wall, the sudden stop of material transfer might still induce the characteristic slope encountered in wire-arc AM parts. Zeqi Hu et al. studied the weld pool dynamics in a GMAW DED process with a three-dimensional transient fluid model and a finite elements model. They concluded that the abnormal bead geometry at the end of the wall can also be attributed to a backward fluid flow and metal swelling in the melt pool [87]. The macrostructural deformation problem occurs when every layer starts and ends at the same point. There is consensus amongst researchers that this deformation that this deformation is caused by changes in the heat transfer mechanisms and the weld pool dynamics [88]. Again, the solution to these deformations will likely require multiple control strategies such as a deposition control system and temperature control system. Relatively easy ways to reduce the deformations at the end of the wall and the apparatus design changes required are discussed in Chapter 5.

Chapter 3

GTAW-DED – Oxide formation mitigation

3.1 Oxide formation in GTAW-DED background

The experimental apparatus developed initially only used the in-built torch shielding gas to prevent oxidation. Because this gas shielding method was developed with single weld beads in mind, severe oxidation is observed once several layers have been deposited (see Figure 61).

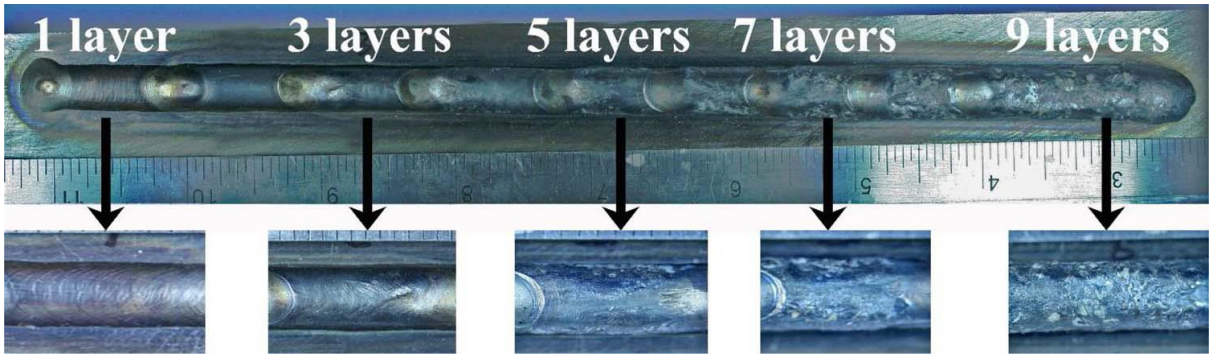

Figure 61. Oxide formation at different layers during a multi-step wall experiment [10].

Most of the oxides float to the melt pool surface, progressively deteriorating the surface finish. Xiangfang et al. studied the oxide accumulation mechanisms and the influence of the oxides in the subsequent depositions. They showed that the accumulation of oxides added to the uncertainty of the layer dimension and deteriorated the surface finish. They also showed drastic differences between walls built with additional shielding mechanisms and walls built only with the standard welding torch. They concluded that oxidation adversely affects arc stability and the wetting and spreading of the melt pool, reducing process stability [10]. Interestingly, Xiangfang et al. reported that small oxides

trapped in the structure can increase the ultimate tensile strength (UTS) of a part by up to 11% and reduce part´s elongation by 19% [10]. However, this increase in UTS comes at great expense in layer appearance and geometrical accuracy. Since the aim of the present work is to increase process stability through the use control systems, several additional shielding methods were development. Following conclusions from the literature, the new shielding mechanisms were expected to increase the arc stability, reduce the generation of oxide islands that affect the pyrometer's temperature measurements (affecting the PID temperature control system) and to improve the overall part layer appearance. Figure 62, shows how oxides affect the arc's voltage during a deposition. Note that since the arc voltage is directly linked to the arc length, reducing oxidation is also expected to improve the stability of the arc-length control system [10].

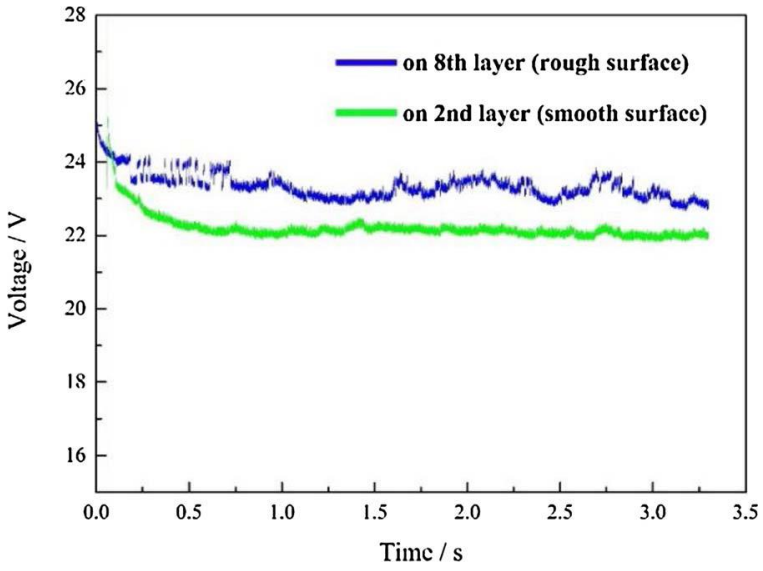

Figure 62. Arc voltage variation example with different surface conditions caused by the formation of oxides [10]

3.2 Trailing shield design

A trailing shield is an additional shielding device that normally works in conjunction with a standard welding torch shielding mechanism. The torch shielding is used to maintain the stability of the arc and the extra shielding device follows the torch closely. The aim of the trailing shield is to create an atmosphere with a low oxygen concentration to prevent oxide formation in high temperature areas. The benefit of a trailing shield, when compared to a controlled environment, is that significantly less shielding gas is used, and it allows for better scalability. With a trailing shield, GTAW-DED machines could be used to manufacture large parts that would be unfeasible with a fixed chamber or a welding tent.

3.2.1 Trailing shield: Multiple welding diffuser design

The first attempt at creating a trailing shield involved using multiple standard welding torch diffusers (see Figure 65). A simple COMSOL model was developed in collaboration with Ioannis Bitharas to identify the most suitable trailing shield parameters, such as gas flow rate and gas nozzle spacing. The aim was to identify the parameters that would prevent the formation of vortices that could lead to significant air entrainment, whilst providing enough argon to cover the required area. Following conclusions from the literature, the trailing shield was designed to reduce the oxygen concentration to approximately 2000ppm [67]. Figure 63, shows the gas velocity plot for the proposed trailing shield, and Figure 64 shows the gas coverage.

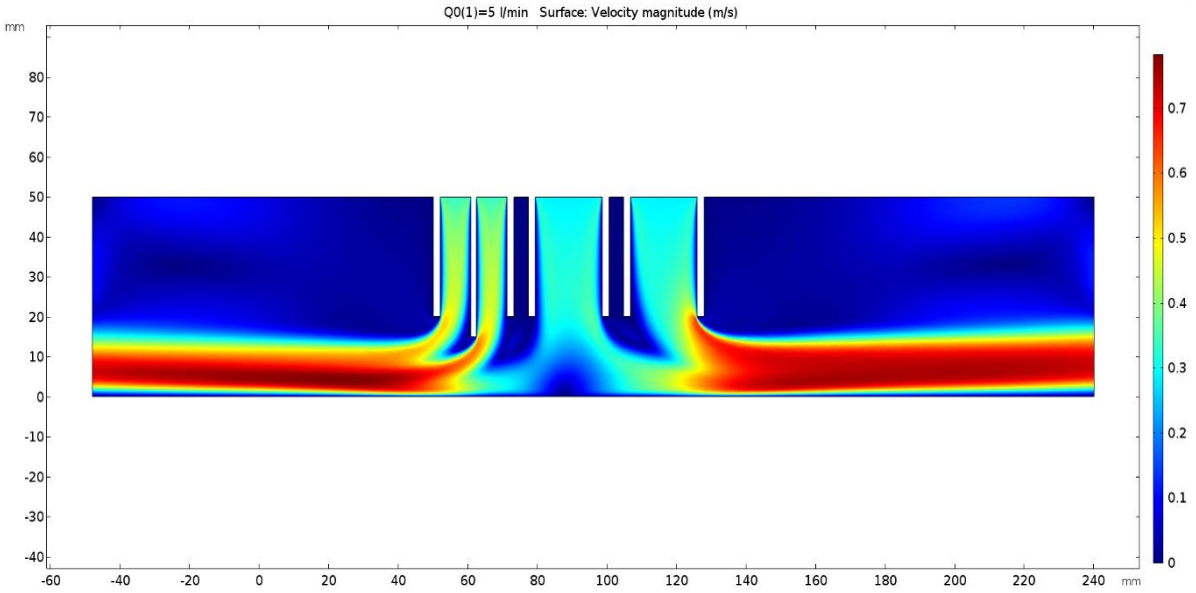

Figure 63. COMSOL model showing the expected shielding gas velocity magnitudes in a 240x80 mm 2D space

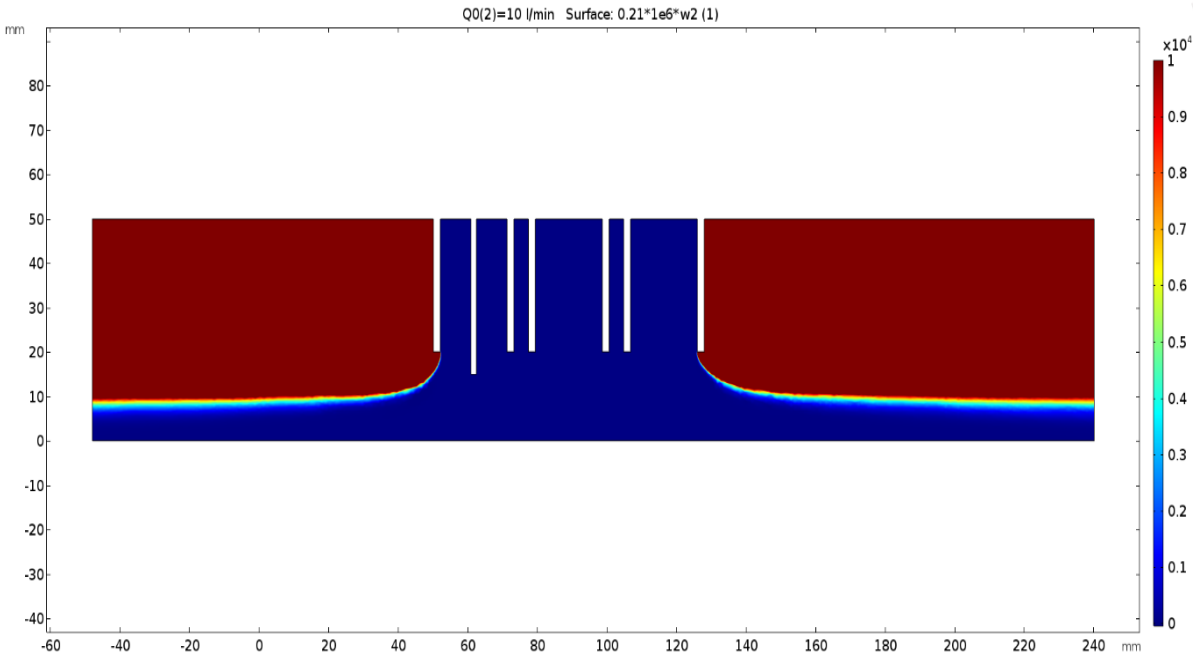

Figure 64. COMSOL model showing the expected oxygen ppm in a 240x80 mm 2D space

Figure 64, shows that to provide an appropriate gas coverage a flowrate of 10 l/min per nozzle had to be used. Following the findings from the COMSOL model, a prototype was developed and tested (Figure 65). The prototype was designed to have all nozzles active from two seconds before the deposition started, to 5 seconds after the deposition had

finished. The first experiments with the designed trailing shield showed only a mild improvement over the first layers. For parts over 5 layers, this trailing shield device had a negligible impact and the oxide accumulation was still apparent.

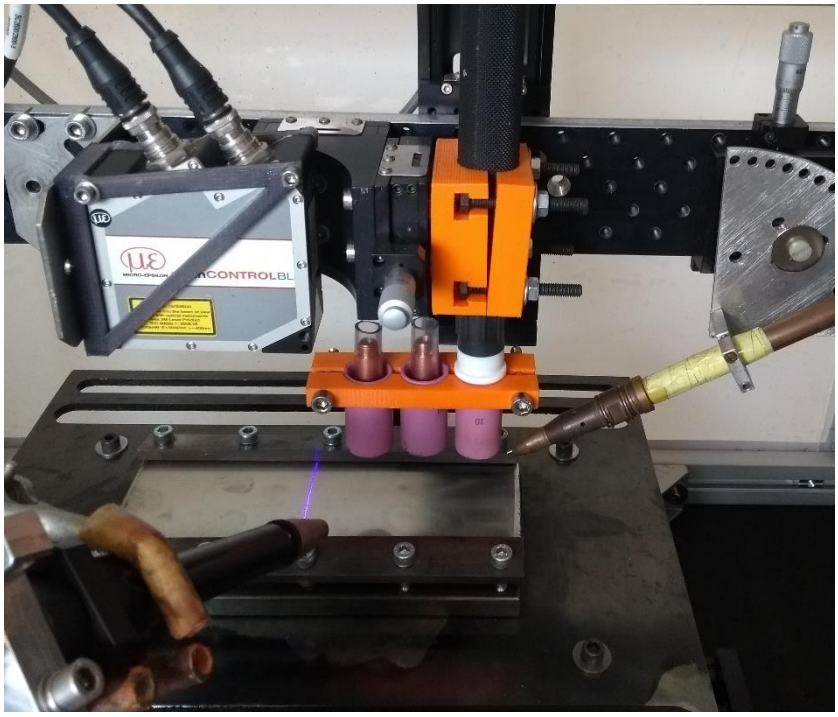

Figure 65. Trailing gas system prototype with multiple torch diffusers

It was concluded that significant air entrainment was the root cause of the oxidation. A new device aimed at reducing this entrainment was designed. The new trailing shield device was based on the findings of S. Jackel et al. Their work explored different concepts of trailing shield designs for GTAW applications [67]. They evaluated different concepts and described the main contamination mechanisms of stainless still welding with numerical and experimental methods. In their design, the two diffusers were encased in a metal gas box to reduce entrainment. Figure 66 and Figure 67 show the design of a movable trailing shield skirt.

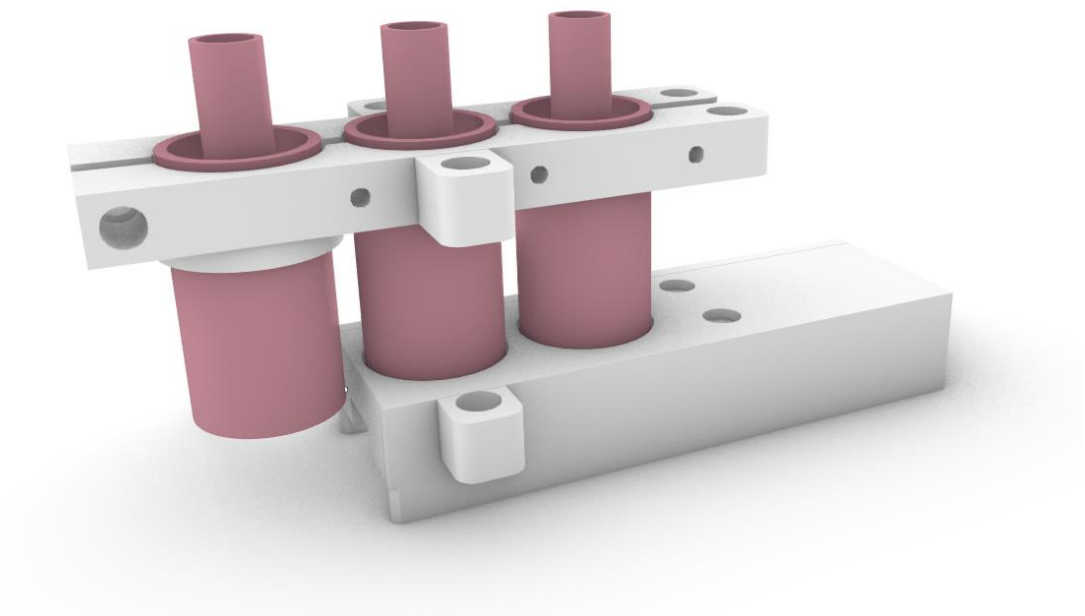

Figure 66. Trailing shield design with entrainment prevention skirt

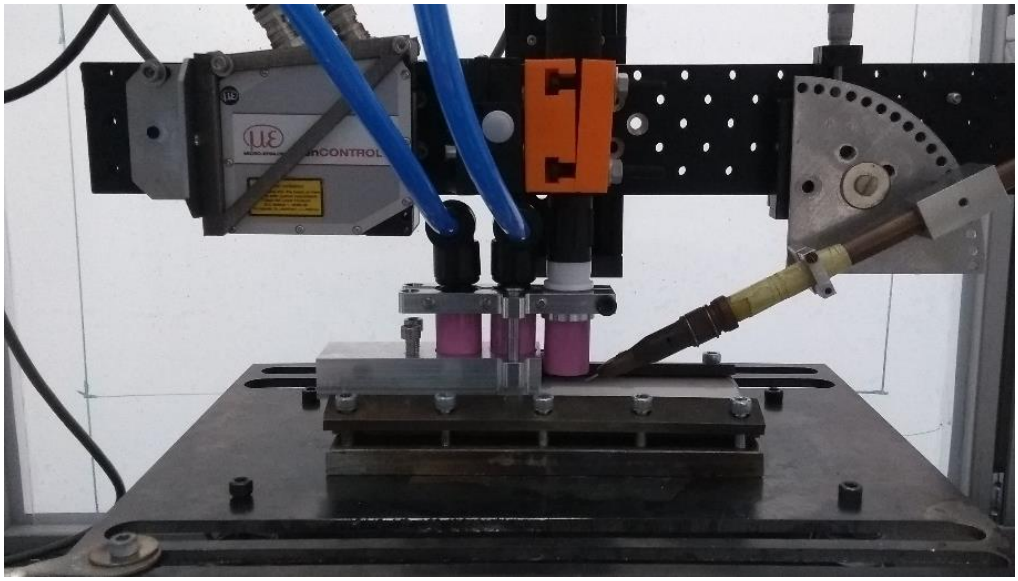

Figure 67. Trailing shield prototype with entrainment prevention skirt

The air entrainment mitigation device is mounted on two vertical shafts that allow it to slide. This design allows for a movable skirt mechanism that automatically adjusts its position to encase the printed wall. Over the first 3 layers, the shielding skirt is contact with the substrate, creating a seal. At the 3rd layer, the skirt is no longer in contact with the substrate, but the skirts are long enough to cover the top 3 layers. Figure 68, shows that a visible improvement was obtained with the use of the trailing shield device in an experiment where no filler wire was used.

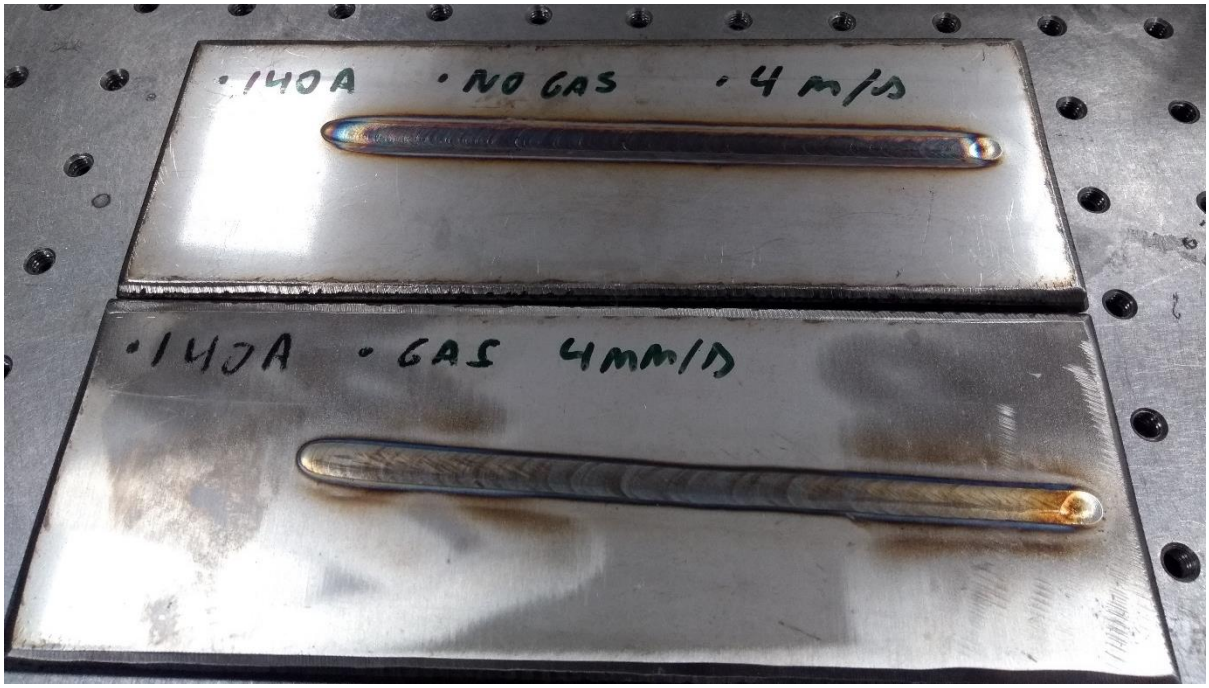

Figure 68. Oxide formation comparison when using a trailing shield with entrainment skirt (bottom substrate) and a standard welding torch diffuser (top substrate).

Figure 69. Example wall created with the trailing shield and entrainment skirt

Figure 68 and Figure 69 show that using the trailing shield device visibly reduces oxidation over the first layers. However, Figure 69 shows that as the build progresses, there is a clear accumulation of oxides. At layer 10, the oxidation levels appear to be similar to those obtained with no trailing shield device. The results indicate, that this trailing shield design is not suitable for multilayer deposition processes. However, the relative success at reducing oxidation over the first layers when the skirt was in contact with the substrate, might indicate that this device could be successful in processes where only the 3 top layers are exposed to the atmosphere (see Chapter 5 for the discussion of such process).

3.2.2 Trailing shield: Laminar flow design

Based on the learnings from the previous attempts, a new laminar trailing shield was designed. The aim of the new shielding device is to provide adequate shielding by preventing air entrainment. Instead of a metal skirt, the new design aims to prevent entrainment with argon flow curtains. Schlieren imaging experiments were performed to test the validity of the system.

Several research groups have studied the use of laminar flow devices. In 2007, Babish used bronze and stainless-steel wool as a defusing medium and in 2011 Kulkarni et al. studied the use of different honeycomb structures and screens to manage turbulence in a wind tunnel [67] [89] [90]. Kulkarni stated that honeycomb structures can straighten the flow by reducing lateral velocities and that the length-to-diameter ratio of the honeycomb cells had to be greater that eight to reduce turbulence [89]. J.Ding et. al developed a trailing shield for wire-arc DED processes and tested its effectiveness with an oxygen analyser [67].

Figure 70 shows the laminar trailing shield device used to create a localized argon atmosphere.

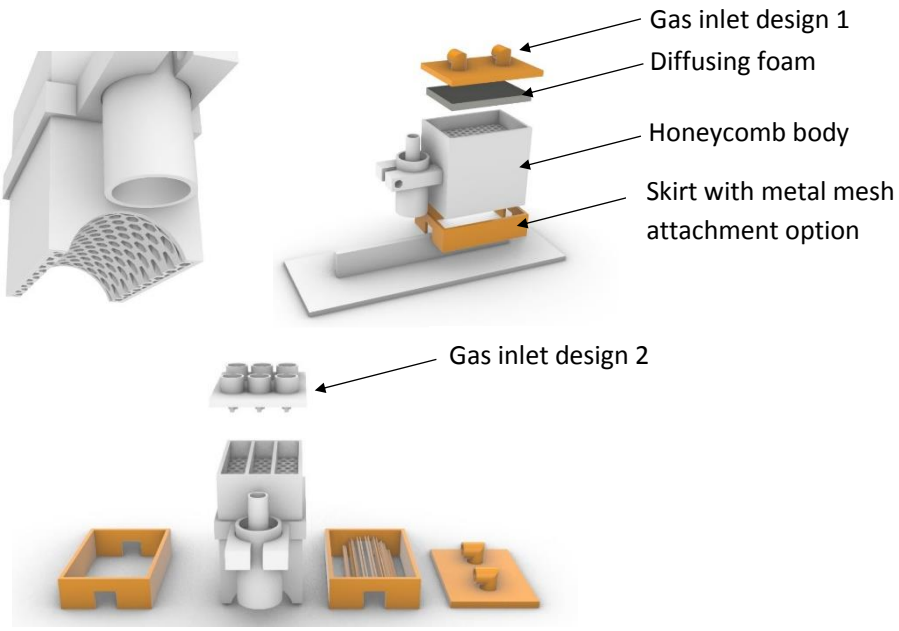

Figure 70. Laminar flow trailing shield device design

Different gas design inlets were developed to test different pipe arrangements. The six-pipe inlet design would enable the user to vary the flow speed at different sections of the flow straightener. The aim of having different flow speeds within a laminar flow is to experimentally determine the best flow dynamics with the schlieren system to prevent entrainment. For example, it could be experimentally determined that a stronger argon flow curtains reduce entrainment more effectively than a homogeneous flow.

The first part of the flow straightener is a diffusion chamber filled with foam that slows down and distributes the inlet gas [90]. Once the flow goes through the diffusing medium, it enters a honeycomb structure with a 19 length-to-diameter ratio. An optional skirt with a metal mesh follows the honeycomb structure and acts as a setting chamber. The metal mesh smooths the velocity profile produced by the honeycomb structure [67]].

3.3 Flow visualization: Schlieren experiments

Schlieren imaging systems have been used since the early 1800's for the visualization of flows. These systems provide and informative and a non-intrusive method for qualitatively studying transparent and optical media [91]. Schlieren is a commonly used method of imaging refractive index gradients and it's been previously used to image shielding gas flows from welding torches. This technique is similar to shadowgraphy and relies on the fact that light bends when it encounters changes in density of a fluid [92]. G.J. Gibson studied the effects of the nozzle standoff distance, the diameter of the nozzle and the relationship between gas flowrate and gas coverage using schlieren. G.J. Gibson also used schlieren to qualitatively investigate the effects of cross drafts at different flow rates on the gas coverage [93]. Dreher et al. used a schlieren system to investigate the influence of different nozzle and contact tip geometries on the turbulence induced by the shielding gas. Dreher concluded that to avoid turbulence, relatively large symmetrical flow sections have to be maintained [94].

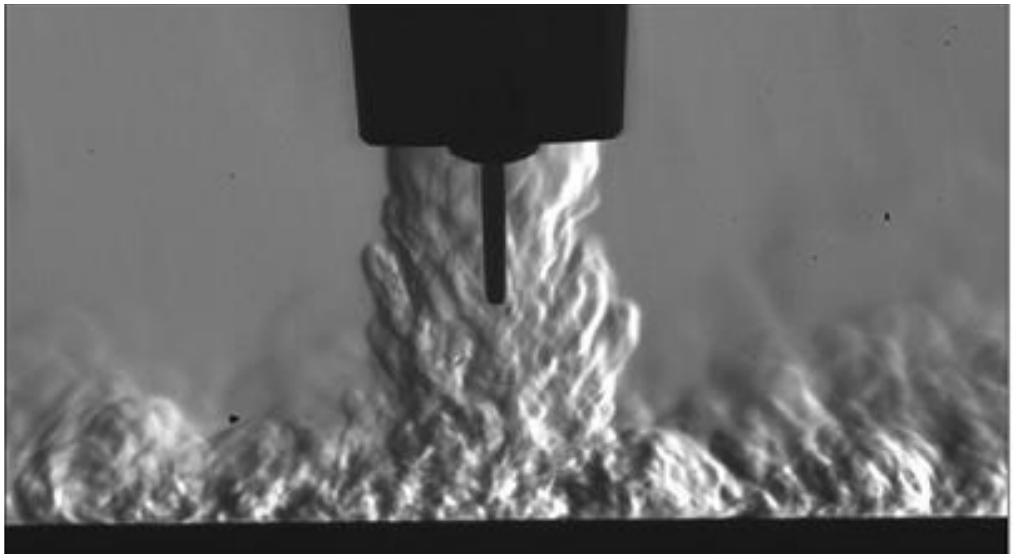

Figure 71. Example Schlieren imaging used to investigate shielding gas flow dynamics [94]

The physical basis for a schlieren system comes from Snell's law, which indicates that lights slows down upon interaction with matter [91]. If the media through which light travels is homogenous, light travels uniformly at a constant velocity. However, if the light encounters a fluid, it refracts and deflects from its original path resulting in schliere

[91]. Figure 72, shows a schematic of the optical system used. This system designed by I. Bitharas in [95] to obtain schlieren images.

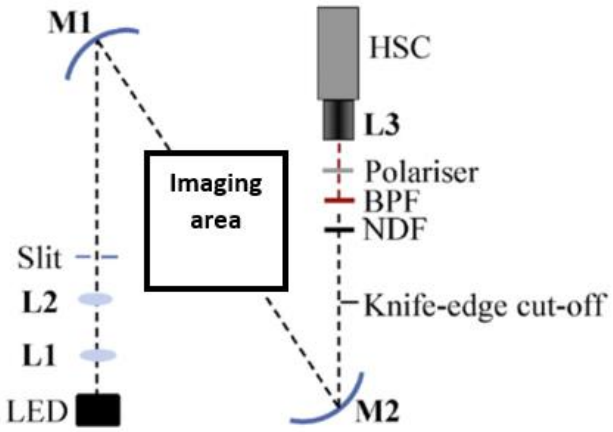

Figure 72. Schlieren optical system [95]

The optical system used Toepler's parabolic mirror arrangement to minimise aberrations. The light was collected by two lenses (**L1** and **L2**) in a telescope arrangement to reduce the LED's spot size before the slit, in order to maximise light collection efficiency. Two 100 mm diameter parabolic field mirrors (**M1** and **M2**) were located approximately two focal lengths apart. The mirror **M1**, collimated the light from the **LED** source and the **M2** focused it to a spot. A vertical Knife-edge cut-off was used to filter the refracted light to form the correct images with high-speed camera (**HSP**). A full description of the optical system used is given by I. Bitharas in [95]. Figure 73, shows the experiment apparatus used to obtain schlieren images of the laminar flow trailing shield device.

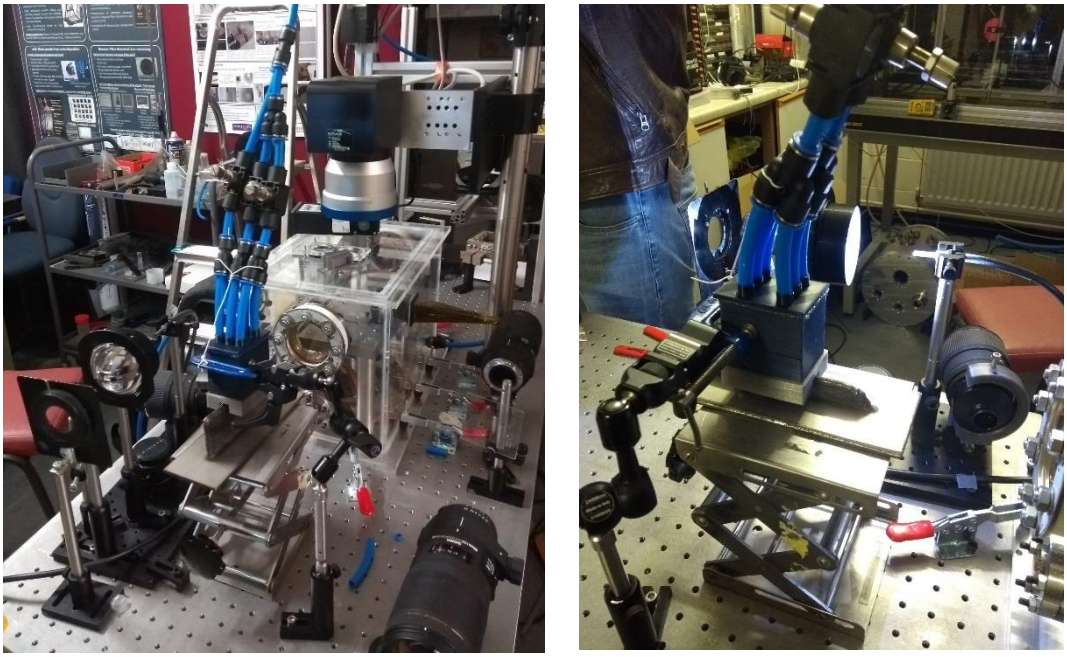

Figure 73. Laminar flow trailing shield device schlieren experiment setup

Experiments were conducted with a 10 layer and a 30-layer wall to evaluate the gas coverage of the laminar flow trailing shield system under different conditions. In all experiments, the same flow rate was maintained across all pipes with the use of flow rate regulators and a flow rate measuring device.

Figure 74, Figure 75, Figure 76 and Figure 77 show the images obtained for a 10 layer wall with an a flow rate of 30,50,75 and 100 l/min.

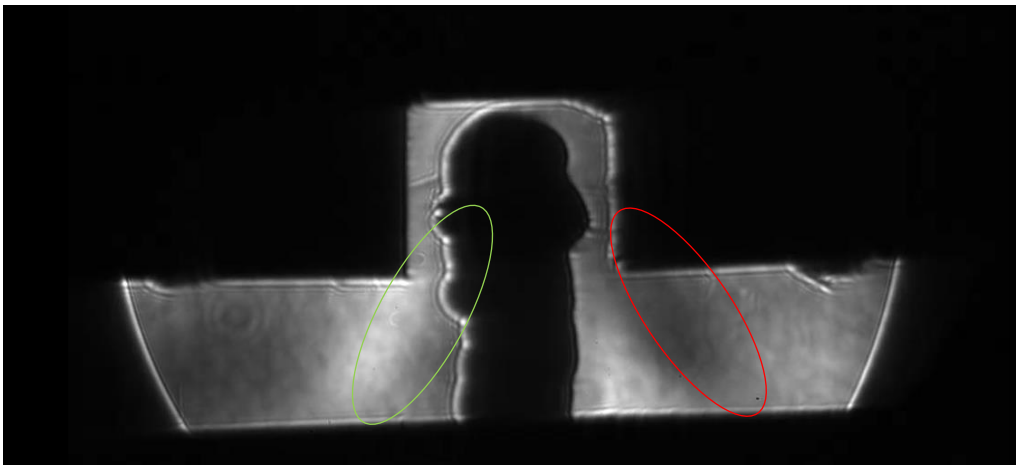

Figure 74. 10-layer wall, 30 l/min argon flow schlieren experiment

In Figure 74, the area indicated by the red circle shows a gradient in density in the X direction. It is worth noting that in the right side of the images the density gradients will appear as dark patches and on the left side of the image they will appear as light patches. This means, that despite the changes in colour, the area inside the green circle, indicates similar phenomena than the area inside the red circle.

The area inside by the red circle likely indicates a curtain of deflected argon flow with a higher density that its surroundings. This argon flow curtain could protect the covered area from air entrainment and reduce oxidation.

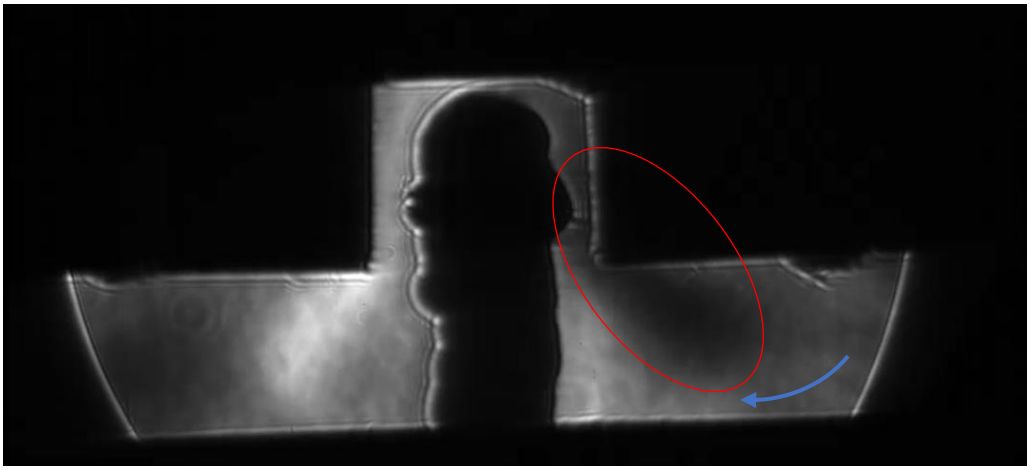

Figure 75. 10-layer wall, 50 l/min argon flow schlieren experiment

In Figure 75, the higher flow rate accentuates the phenomena described in Figure 74. However, the higher flow speeds appear to deflect the argon curtain. This deflection opens the possibility of air entrainment (blue arrow).

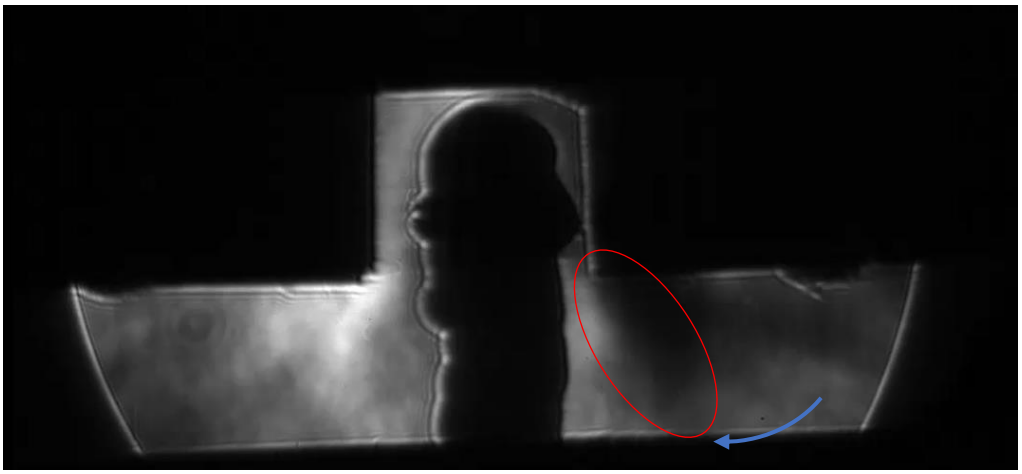

Figure 76. 10-layer wall, 75 l/min argon flow schlieren experiment

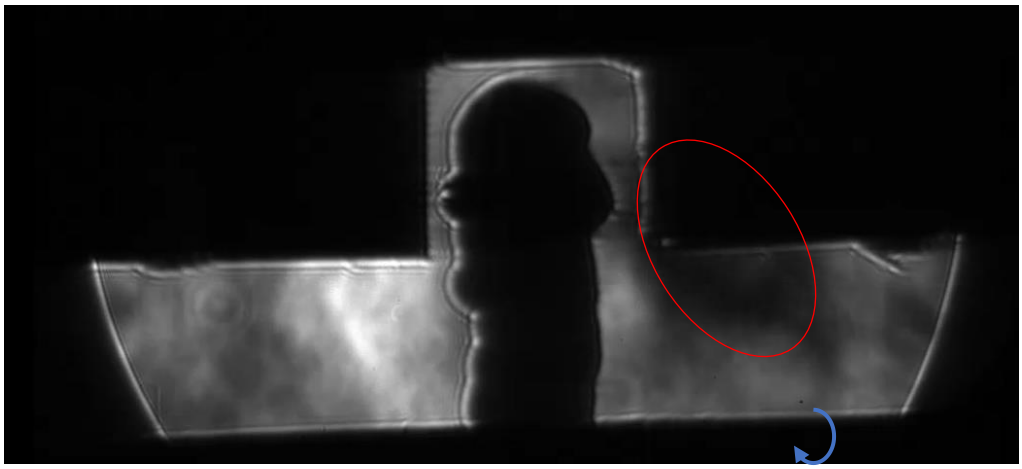

Figure 77. 10-layer wall, 100 l/min argon flow schlieren experiment

Figure 76 and Figure 77 show that further increasing the flow rate leads to an increase in turbulence. A turbulent flow could generate vortices that destabilize the flow cover and promote air entrainment.

Figure 78, Figure 79, Figure 80 and Figure 81 show the images obtained for a 30 layer wall with an a flow rate of 30,50,75 and 100 l/min.

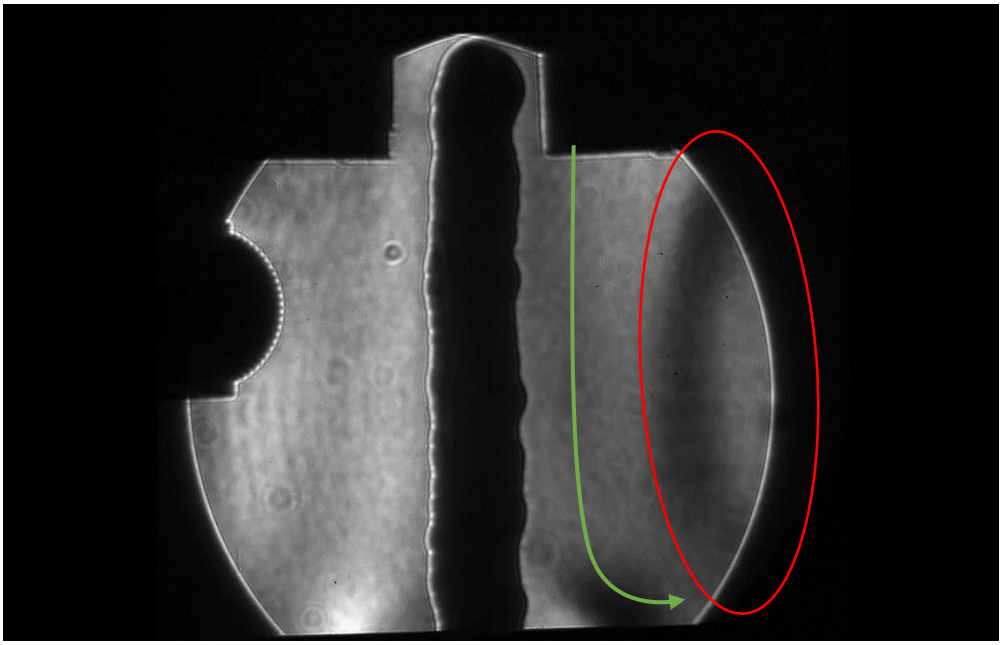

Figure 78. 30-layer wall, 30 l/min argon flow schlieren experiment

Figure 78 shows that a laminar argon flow curtain is created with a 30 l/min flow (red circle). The green arrow also indicates an extra argon flow curtain that appears to adhere to the wall until it reaches the substrate.

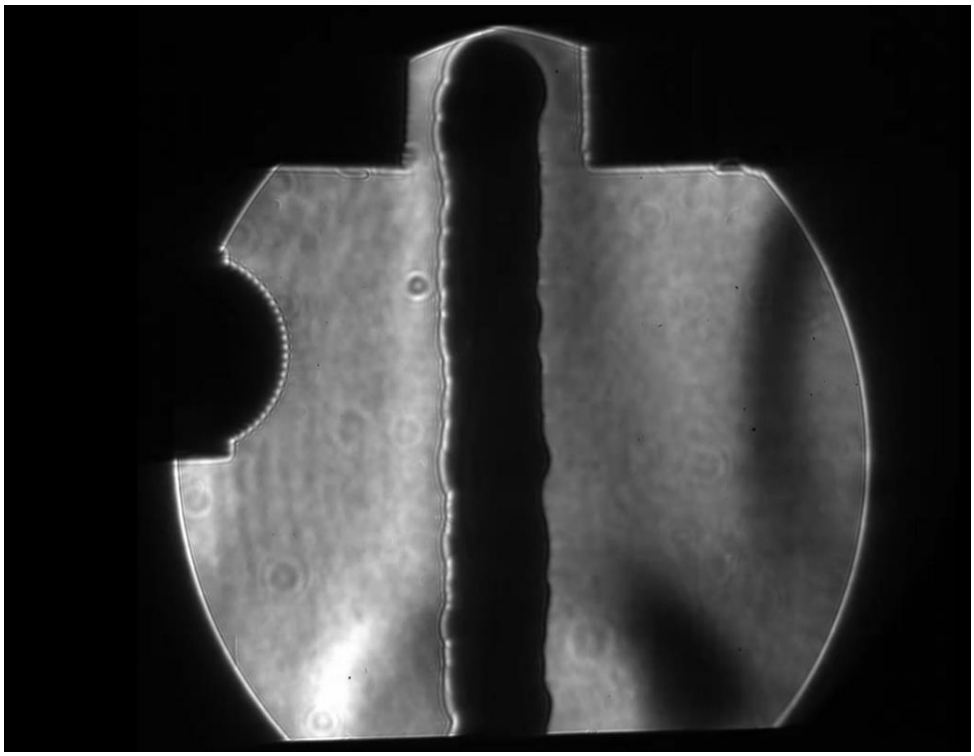

Figure 79. 30-layer wall, 50 l/min argon flow schlieren experiment

Figure 79 shows that, the 50 l/min argon flow appears to accentuate the phenomena observed with the 30 l/min flow. The uniformity of the flow is maintained and the density in the argon flow curtains and at the bottom of the wall appears to be greater.

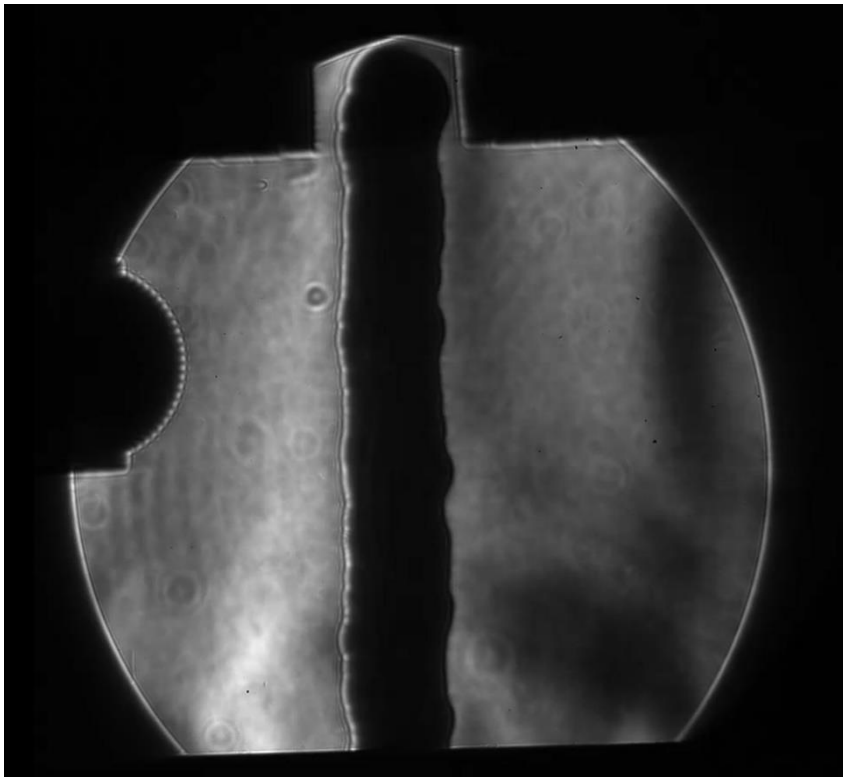

Figure 80. 30-layer wall, 75 l/min argon flow schlieren experiment

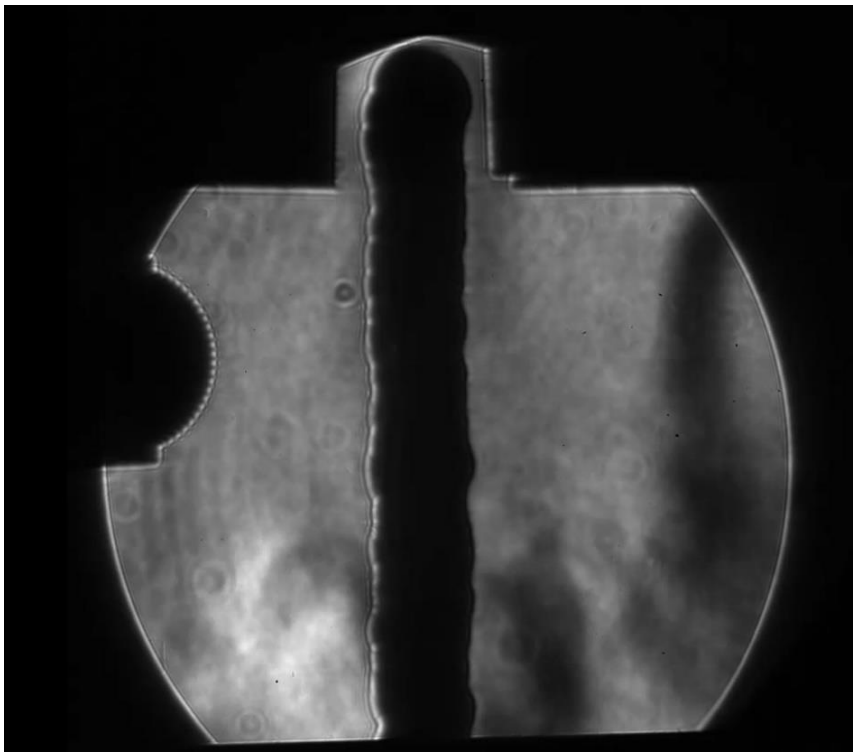

Figure 81.30-layer wall, 100 l/min argon flow schlieren experiment

Figure 80 and Figure 81 show that that the 75 and the 100 l/min flows lead to an increase in turbulence.

3.3.1 GTAW-DED schlieren experiments discussion

The schlieren experiments showed that the laminar flow trailing shield device does in-fact deliver laminar argon flows at 50 l/min. The images show that if the flow is increased beyond 50 l/min, turbulence is likely. Arguably, the best results were obtained with a 30 l/min flow in both of the experimental conditions tested. The argon flow curtains, and the argon flow that adheres to the side of the wall show very promising results and indicate that the trailing shield is likely to reduce oxidation. However, the schlieren images only provide a qualitative assessment and further experiments are required to test the validity of the system.

Similar experiments to those conducted by J. Ding et al., were an oxygen analyser is used to determine the oxygen concentration of specific points during the welding process will indicate if the 30 l/min flow is able to withstand the turbulence induced by process [67].

Chapter 4

PBF – Oxygen Monitoring and control

4.1 Shielding gas in PBF processes

During the PBF process, the interaction between the powder bed and the laser can lead to the formation of oxides. PBF technologies use sealed chambers with low-oxygen concentrations to reduce oxidation. In a similar way to GTAW-DED processes, oxide formation has a detrimental effect on process stability and can lead to a significant reduction in part quality. Li et al. determined that with an atmosphere with a high oxygen concentration, the wettability of liquid metal with the previously deposited and oxidised material is worsen, leading to ball formation [24] [96]. Balling refers to the formation of spherical and ellipsoidal balls during bead deposition and can lead porosity during a multi-layer process. Li et al. studied balling formation in PBF processes and concluded that the oxygen content plays a significant role in determining the balling initiation. Li el al. stated that balling can be considerably reduced with an oxygen concertation of less than 1000 ppm [96]. Camille Pauzon et al., also determined that below 1000 ppm, the effects of residual oxygen on the tensile properties of stainless steel 316L and the oxygen pickup from the produced parts are limited. They also concluded that processing with lower purity argon introduces powder degradation risks and that processing with high purity argon ensures limited powder degradation and high toughness of the produced parts [24].

Despite the importance of the shielding gas for PBF processes, the shielding gas used, and gas process parameters has been seldomly addressed [24]. As a result, the shielding gas used by PBF manufacturers is mostly limited to argon and nitrogen, and the only requirement in commercially available machines is that the oxygen level is below a certain threshold [24]. In commercial PBF machines, the required atmosphere is normally obtained by flushing the entire chamber with argon. The flushed gas is vented through a series of particle and gas filters until the required level of oxygen is obtained.

Another common approach is to create a low vacuum in the chamber before the flushing the process [24]. Despite the standardised procedures to reduce oxygen concentration, creating chambers that operate below 1000ppm has proven to be a challenging task.

In PBF processes, an inert gas crossflow is also used to remove unwanted by-products generated by the interaction between the laser and the powder. The main by-products are spatter, metal vapour plume and particulate condensates [22] [25].

These products can reduce the attenuation of the laser and re-deposit over the processing area affecting the mechanical properties of the built components [22]. Investigations for high-power laser beam welding have shown that that the condensed metal vapor particles alone can cause a 10% attenuation of the laser beam [20]. High speed imaging experiments have also shown, that powder particles ejected by process also interfere with laser path further compromising the stability of the process. Spatter and powder particles are reportedly ejected by entrainment of the plume's jet and by the Marangoni flow of unstable melt pools. Ly et al. classified particle ejection as follows: i) some particles are entrained by the gas flow and can be pulled into the melt pool; ii) some particles can travel through the vapour jet but not the laser beam, i.e. " cold particles"; iii) others can travel through the vapour jet and intersect the laser beam, i.e. "hot particles [24] [96].

If these particles are un-removed, the ejection of molten spatter can fall onto a consolidated surface and fuse with it. Haeckel shows the formation of pores due to large spatters adhering to the surface of PBF parts [20].

This chapter discusses the design, programming and manufacture of a PBF-AM machine. This work includes the design and testing of controlled environment capable of maintaining a 1ppm atmosphere during the entire build process and the development of a laminar crossflow device that effectively removes the unwanted by-products and improves part quality. The controlled environment is monitored during the entire build process and a simple control mechanism has been developed to stop the process if the oxygen level exceeds the selected threshold. High speed imaging experiments were also conducted to test the validity of the cross-flow device. The combination of the programming, the controlled environment, and the cross-flow device has drastically

improved the quality of the produced parts and allowed the developed PBF system to create complex lattice structures directly from CAD models.

4.2 PBF experimental apparatus

The PBF machine was developed to autonomously produce complex parts and to allow the user to image the process. This work follows P. Bidare's development of an open architecture AM machine that yielded multiple publications. Following the conclusions and guidance from P. Bidare and the literature, design efforts were focused on creating a low oxygen environment, a laminar crossflow and automating the process. Figure 82 and Figure 83, show diagrams of the developed PBF machine.

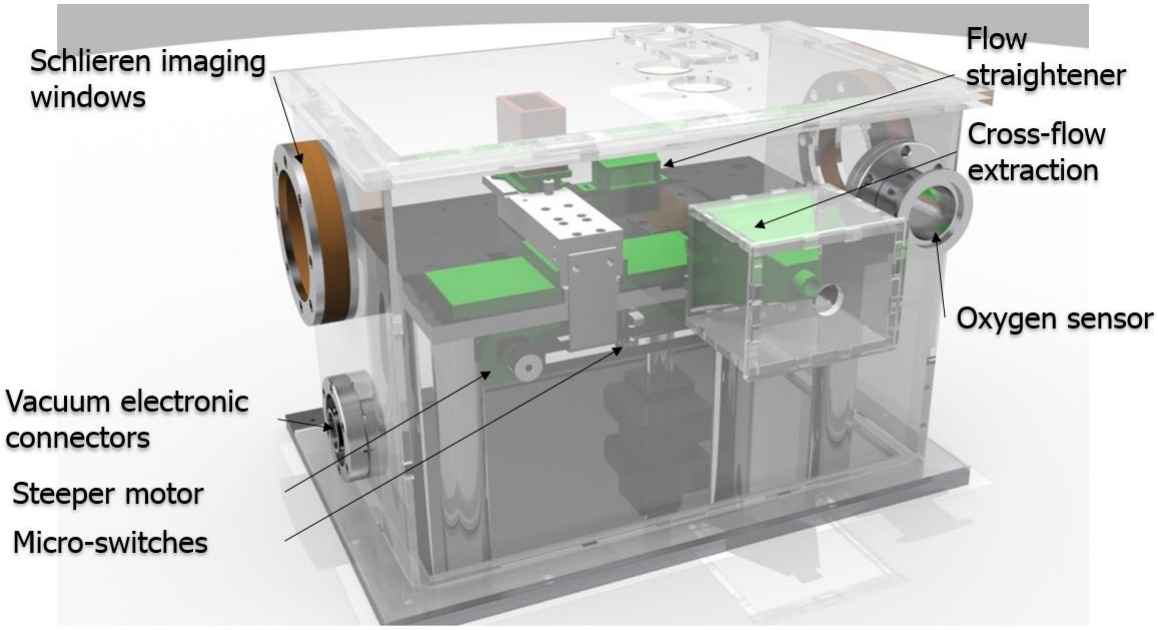

Figure 82. Powder based fusion machine design (1)

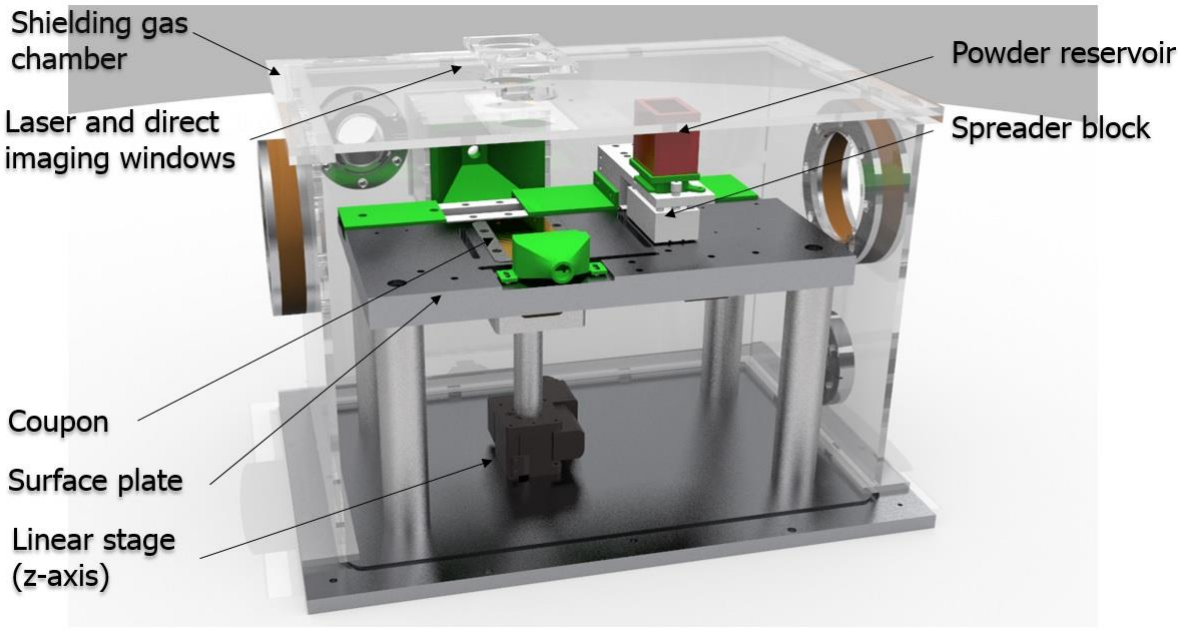

Figure 83. Powder based fusion machine design (2)

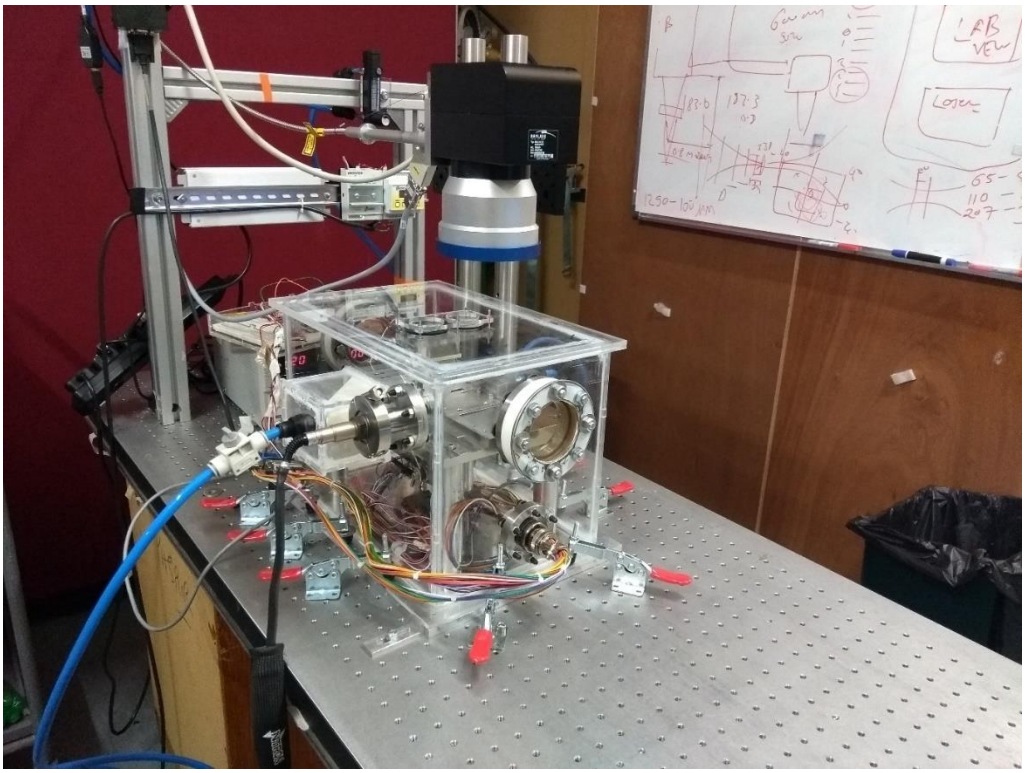

Figure 84. Open architecture powder based fusion machine

The PBF machine is programmed with multiple languages and controlled through LabView. The LabView allows the user to set parameters such as the number of layers,

the layer height, the powder spreader speed, the number of layers before the powder spreader is re-filled, the duration of the crossflow, etc. Once the LabVIEW program starts, operation commands are sent to a micro-controller coded with C#. This micro-controller operates the powder spreader and the automatic gas flow system. The Z stage movement is controlled directly through LabView and a data acquisition card is used to collect data from the oxygen sensor. The same data acquisition card is used to send a signal to the laser processing micro-controller. The laser processing is done through SCAPS (micro-controller) and SAMlight (software). This independent program is used to process the 2D layer information and the laser parameters. SCAPS/ SAMlight controls the galvo and also allows the user to draw scans and create hatch patterns. With this system, the PBF machine has the versatility of a commercial laser scanner and allows for the automated creation of complex parts. Once the user starts the process, the PBF machine requires no further intervention until the part is complete - aside from powder re-filling in long builds.

The LabView program controls the system as follows: First, the program checks the oxygen in the chamber. If the oxygen level is below the selected threshold, the reservoir and the spreader block are moved together via a belt drive system. The correct layer height is achieved by lowering the Z stage. Once the layer has been deposited, the program activates the cross-flow system. After a few seconds, the LabView signals the SCAPS system to start the laser processing. A few seconds after the material has been sintered, the crossflow is stopped. The Z stage is lowered, and a new layer of powder is deposited.

4.3 Apparatus components

Powder Spreading assembly

The powder spreader contains a V-shaped reservoir designed to deliver gravity fed powder between two cylindrical spreaders. As indicated by P. Bidare in [19], the rear spreader (with respect to the forward spreading direction) is 100 µm higher than the front spreader. The first pass leaves a 100 µm excess powder depth that is scraped-off when the spreader block returns to its starting position. The spreaders are made from 3 mm diameter silicon cylinders. Layer depth is determined by the height of the first spreader above the build coupon. Before the build process, the height is checked with feeler gauges. Subsequently, the layer height is controlled by the Z stage (Standa 8MVT40-13-1, ~10 nm resolution). The key requirement from the spreading system it that it produces a repeatable and accurate layer thickness.

To aid the gravity fed system and to increase the number of layers deposited without any intervention, a powder cartridge was designed.

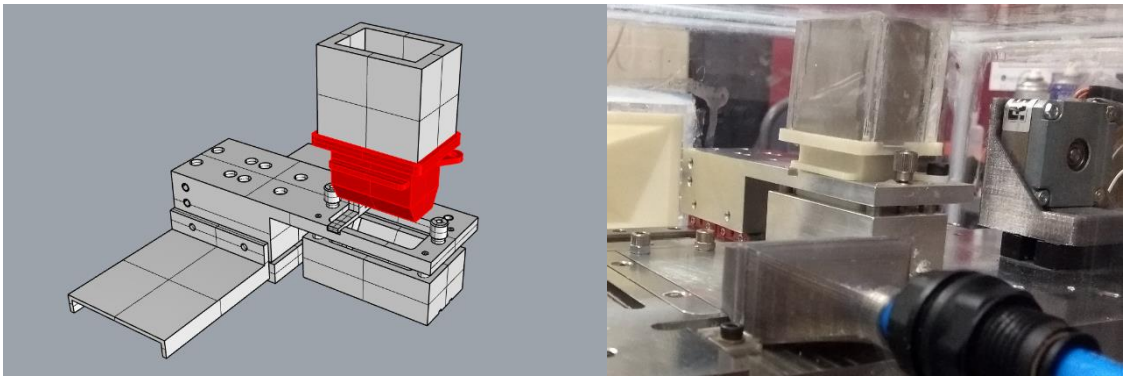

Figure 85. Powder reservoir system design

This design allows the PBF system to print approximately 100 layers without any user intervention. Further, the increase in powder mass aids the powder delivery of the gravity fed system, resulting in uniform and repeatable layers.

Build Platform

The build platform assembly is connected to the Z stage and allows the steel substrate (80x40 mm) to be lowered. The steel substrate is mounted onto a spring-loaded platform that allows the user to adjust the orientation of the substrate. This simple

design is similar to the one used in the GTAW-DED welding bed and ensures that the substrate is parallel to the powder spreaders. The spring-loaded platform also has a Teflon O-ring around the edge to prevent powder from falling when the Z-stage is lowered. The maximum printing height is approximately 8 mm.

Laser processing assembly

The powder was melted using an SPI 400W continuous wave (1070nm) laser and a Raylase MS-II-14 scanner with 163 mm focal length f-theta lens. The Raylase scanner and the f-theta assembly were mounted on a manually adjustable rail (Z axis) to control the focused spot diameter. In this work, a 50 µm spot diameter with a Gaussian beam profile was used in all experiments.

Controlled environment design

The controlled environment was designed to maintain an atmosphere with an oxygen concentration of 1 ppm during the build process. The sealed chamber was designed to allow for multiple electrical connections ports, multiple gas inlet and outlet ports and multiple windows to image the process. The system also contains a powder re-fill and an oxygen sensor port. As shown in Figure 86, the Perspex chamber is sealed with an aluminium base plate using a silicon gasket and 10 toggle clamps.

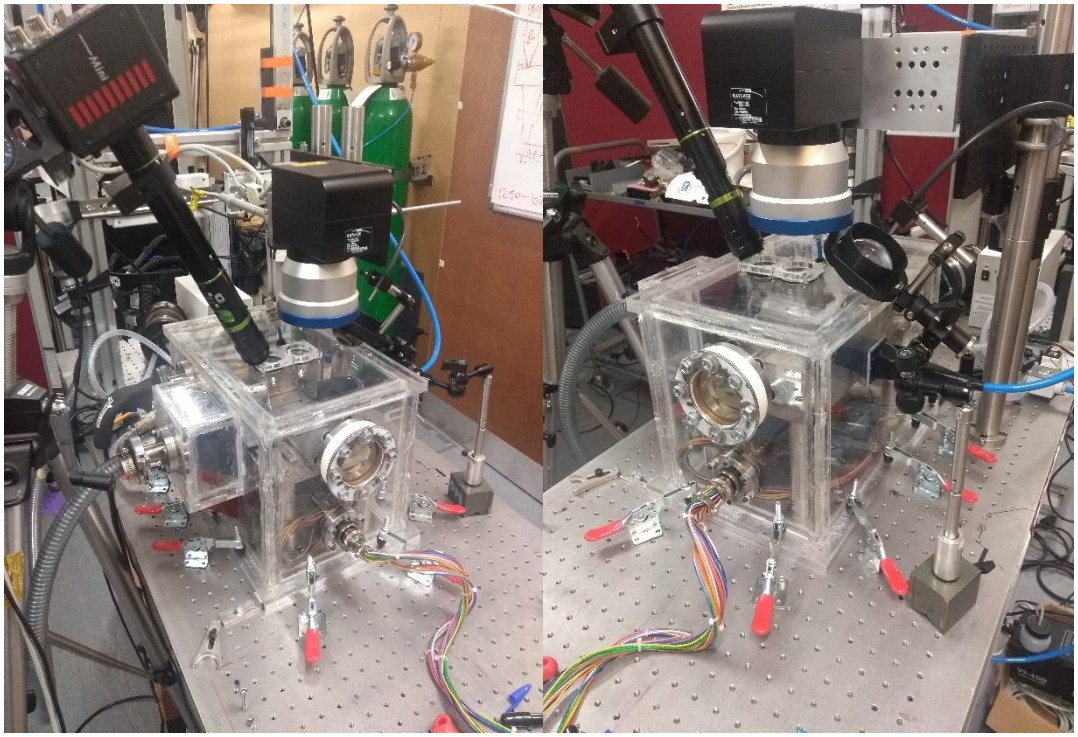

Figure 86. Controlled environment chamber design during operation

Despite the relative simplicity of the box, numerous design iterations and building procedures were needed to deliver the 1ppm target during the entire build process. To test the validity of the system, an oxygen sensor (Ntron-Microx) with a measuring range of 1ppm to 25% was used. The oxygen sensor data was collected with an NI data acquisition card and a shunt resistor circuit designed to measure the current output. Following experiments to determine the relationship between the current output and the oxygen content readings, leak rate experiments were performed both with the PBF machine in operation and static conditions.

The leak rate experiments showed that minor design and building procedure changes had a drastic impact on the effectiveness of the controlled environment. Figure 87 shows the results obtained during a static leak rate test for the 5th design iteration. This design used 5 mm Perspex and had a single outlet port. Note, that the 5th generation chamber is showed in Figure 84.

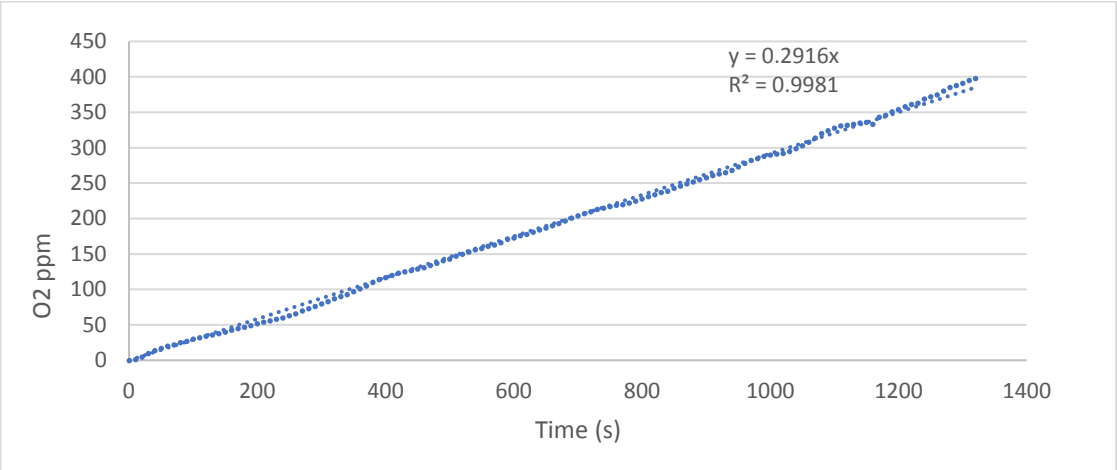

Figure 87. Static leak rate experiment on 5th generation chamber

Figure 87, shows that a leak rate of 0.2916 ppm per second was obtained with the 5th generation chamber. In this design, it was apparent that the chamber outputs were insufficiently large to accommodate the crossflow gas without increasing the pressure in the chamber. The repeated use of this design led to fatigue cracks that progressively deteriorated the chamber and increased the leak rate. For the 6th generation design (see Figure 86), 8 mm Perspex was used, and the outlet ports were designed to accommodate the cross-flow. The 6th iteration also incorporated Perspex L-brackets reinforcements in the corners. The building procedure was also modified accommodate three gluing operations. Two purpose built P3 particle and gas filters were also designed a connected to the new outlets.

The final chamber design and the final building procedure was able to maintain a 1 ppm oxygen environment during a 17h static test and 1ppm environment indefinitely during the build process. Further, a simple control system was developed to ensure that the PBF machine never operated below a selected oxygen threshold. If a relatively high oxygen concentration is detected, the cross-flow activation time is increased, and the machine does not operate until the required atmosphere is obtained.

Crossflow design

A crossflow design similar to the one used in GTAW-DED was developed to remove unwanted by-products. The aim is to transport these products away from the build platform. Figure 88 shows an example of the by-products that can interfere with the PBF process.

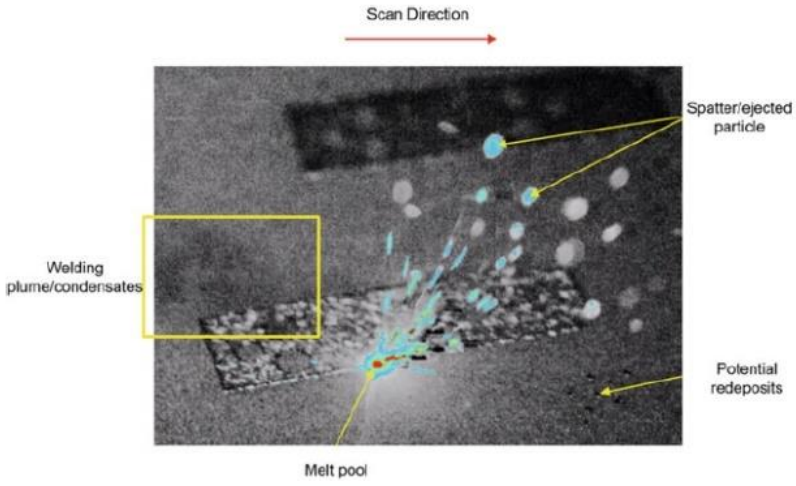

Figure 88. Unwanted by-products generated during a part build in a PBF process [22]

Following conclusions from the literature, the cross-flow device was designed to be laminar. Wei-Cheng Wang concluded that the uniformity of the flow in a PBF machine is one of the key requirements to improve process stability and Ferrar et al. showed that a more homogenous flow leads to a better density distribution in lattice structures [97]. The literature also suggests that homogeneous flow above the bed should be as fast as possible [20] [98] [99]. However, our imaging experiments indicate that a maximum flow rate is not always beneficial.

To obtain a homogeneous flow at high flowrates, the crossflow device was designed following the design specifications of the GTAW-DED laminar flow trailing shied. A pipe array structure based on Kulkarni's findings was used to straighten the flow by reducing lateral velocities. A settling chamber and a metal mesh were also used to deliver a homogenous flow and reduce the velocity profile. The main difference between the GTAW-DED trailing shield design and the PBF cross-flow device, is in the initial defusing mechanism. Since space was not a restriction, a relatively large diffuser could be used to gradually change from the 10 mm pipe diameter to the 30x30 mm outlet of the crossflow device. A gradual change from a circular cross-section to a square cross-section delays the separation of the boundary layer and reduces the abrupt expansion induced minor-coefficient losses. Fluid dynamics literature indicates that to reduce the minor-coefficient losses the angle of the diffuser has to be less than 8 degrees [100]. A simple COMSOL model was also developed by Ioannis Bitharas to determine the optimal length of the initial diffusion chamber. From the model, it was concluded that above 125

mm of diffuser length, the turbulence was adequately low. For the final design, the diffuser length was conservatively chosen to be 150 mm resulting in a diffusion angle of 5.4 degrees.

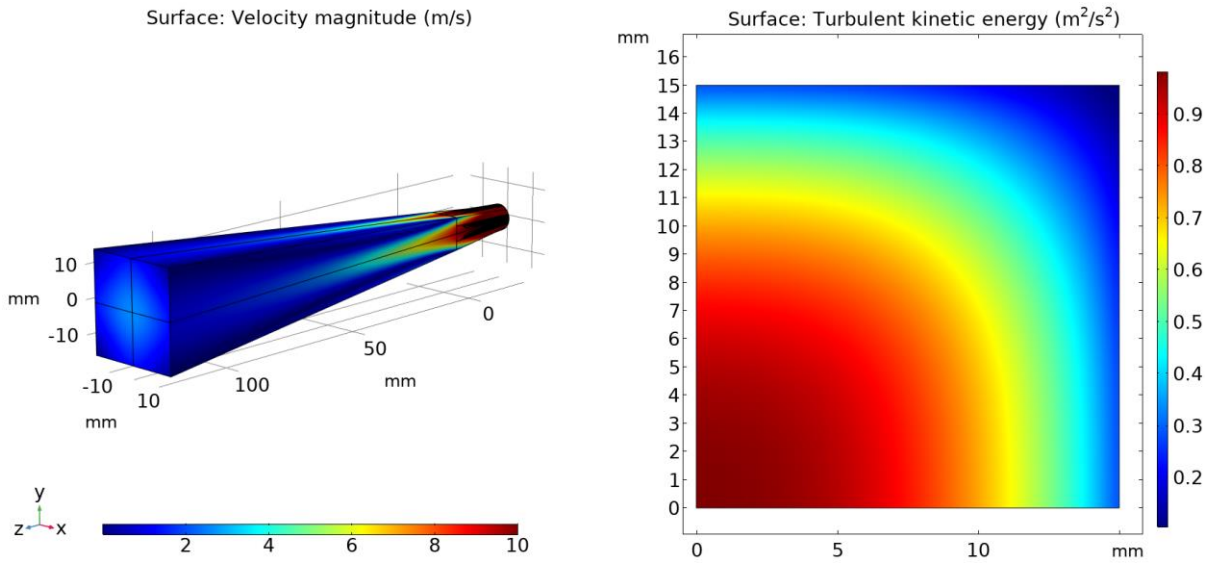

Figure 89. COMSOL model used to determine the crossflow diffusion chamber length (velocity magnitude and turbulence kinetic energy plots used to examine the fluid flow with different diffusion chamber lengths)

Figure 89 shows the model developed to determine the geometry of the diffusion chamber for a maximum flowrate of 150 l/min. As expected, the model shows that a velocity profile still exists and that further mechanisms like the honeycomb structure and a mesh screen are still required to obtain a homogeneous flow. Further experimental tests that evaluate the effectiveness of the mesh screen and pipe array were conducted and are explained in Section 4.4.1.

Figure 90 and Figure 91 show the design of the crossflow device and its position within the seal chamber.

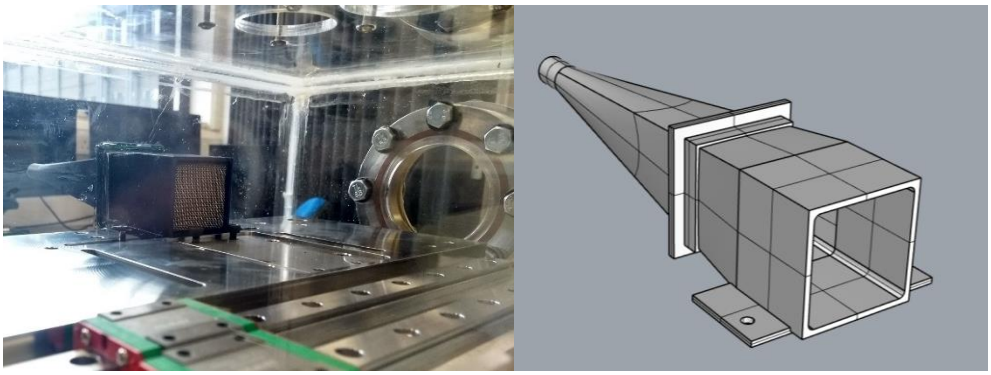

Figure 90. Crossflow diffusion chamber design and location in the PBF system

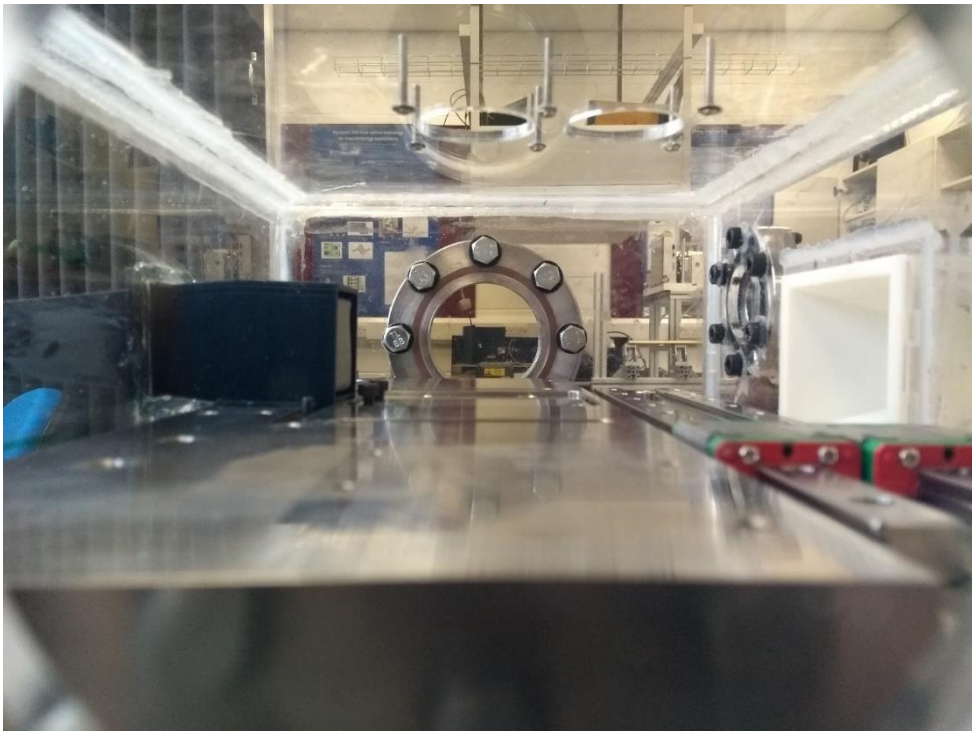

Figure 91. PBF crossflow device design installation

An extraction funnel was also designed to remove the by-products from the process. Figure 92 shows how the extraction funnel, crossflow and in-line filter assembly could be used in a re-circulation system. It is worth noting, that all experiments were conducted without a re-circulation system and that outlet pipe assembly shown in Figure 92 was significantly modified in the final controlled environment chamber.

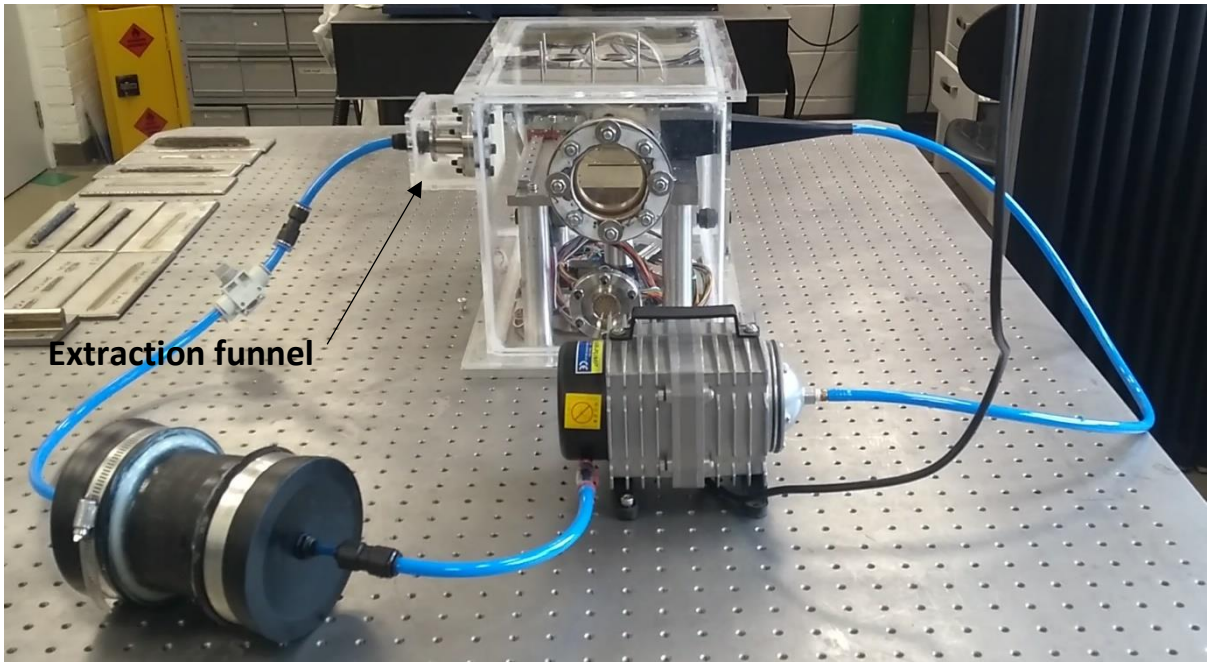

Figure 92. PBF crossflow re-circulation design

4.4 PBF Crossflow experiments

4.4.1 Flow characterisation experiments

Imaging experiments were performed to test the validity of the crossflow system. The schlieren system discussed in Section 3.3 was used to examine the flow dynamics at different flow rates and different crossflow device configurations.

Crossflow validation and configuration experiments

The schlieren system was used to determine if the crossflow device was delivering a laminar flow during process conditions. Figure 93, shows that without a pipe array and screening mesh, a 150 l/min flow is turbulent. With the use of a 3 mm pipe diameter array (length to diameter ratio of 8.3) and a screening mesh at outlet, the crossflow device delivers a laminar flow.

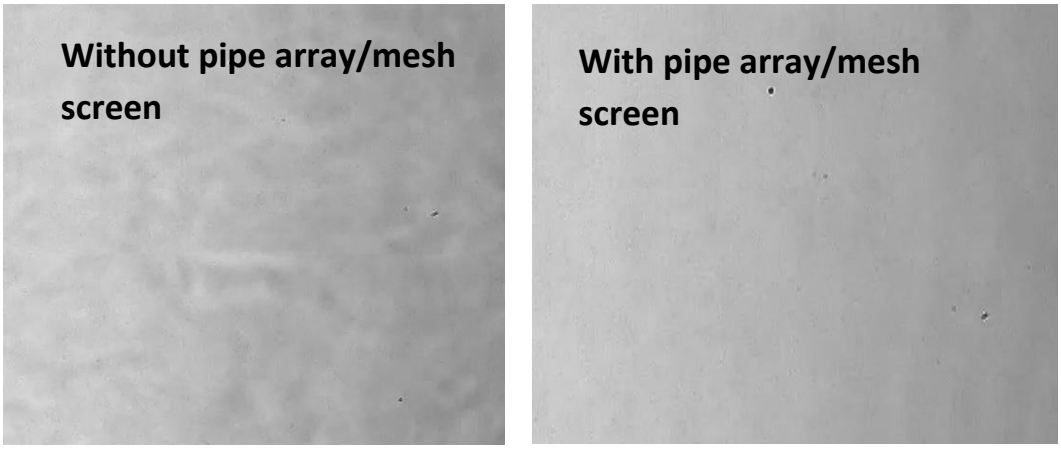

Figure 93. Comparison between different crossflow device configurations with an argon flow rate of 150 l/min

Figure 94 shows the interaction between the crossflow and the plume at different flow rates. In this experiment, no powder was used, and the laser was configured as follows: Spot diameter 50 µm; Power – 200W; Travel speed - 750 mm/s.

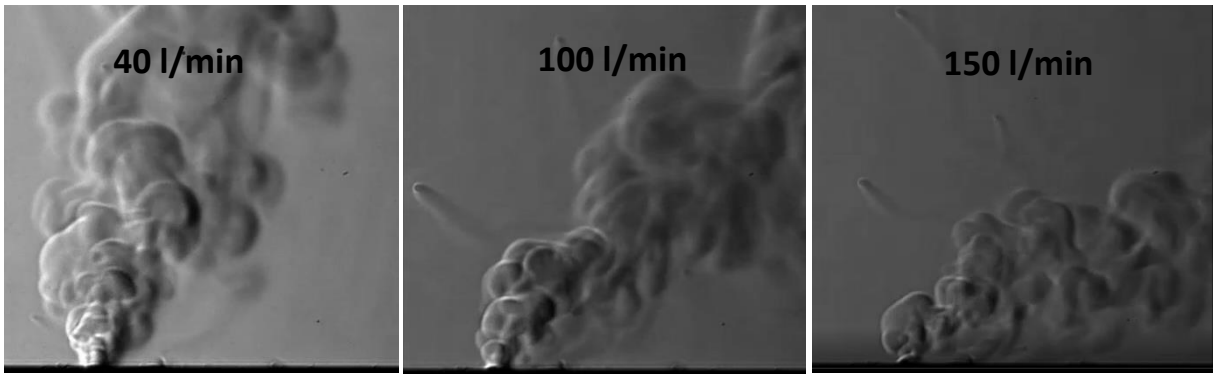

Figure 94. Plume extraction experiments with different crossflows (spot diameter 50 µm; Power – 200W; Travel speed - 750 mm/s)

Figure 94 indicates that higher flow rates minimise the possible interaction between the laser and the laser plume. The data collected from this experiment concurs with the findings in [98] [99], and indicates that the crossflow should be as fast as possible. However, the relatively large field of view and the lack of powder does not provide sufficient evidence to validate this conclusion. Thus, further experiments with a smaller field of view were conducted under real operating conditions.

Flow speed experiments

Experiments were conducted to establish the flow speed outside the crossflow device for different flow rates. The first attempt was the use of hot-wire anemometry to determine flow speed at different points across the build platform. Commercially available anemometers are only calibrated for air, thus a correction graph was required to determine fluid velocities in an argon atmosphere. Figure 95, shows the calibration apparatus used to obtain the correction graph.

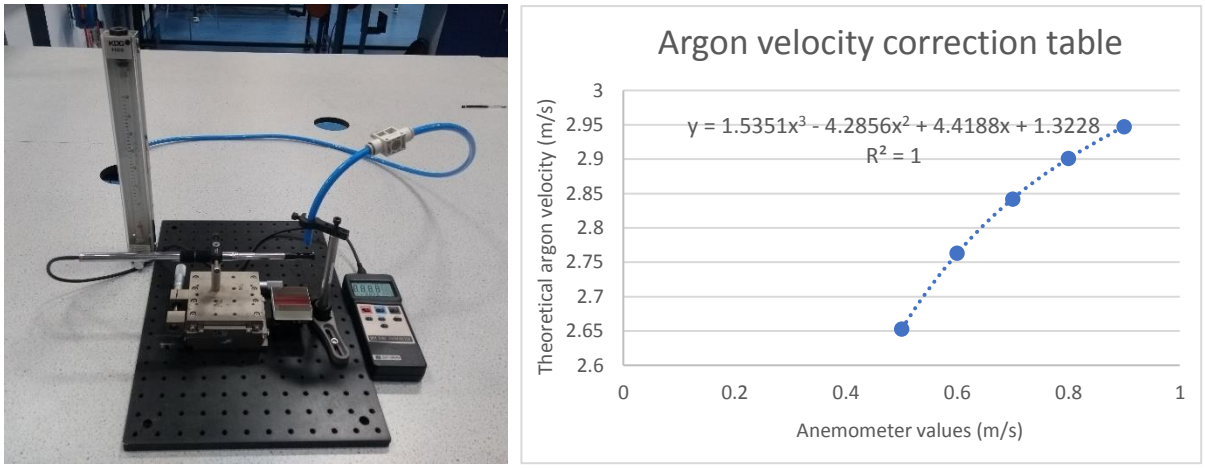

Figure 95. Experimental apparatus used to obtain an anemometer correction graph to measure Argon crossflow velocities

In this experiment, theoretical fluid velocity was calculated with the use of experimentally obtained flow rates. It is worth noting that only laminar flow speeds were used to calculate the correction graphs (Re<1400).

The data shown in Figure 95, was used in an attempt to obtain flow speeds at different points. However, the data obtained lacked consistency and the spatial resolution was inadequate to establish a fluid velocity profile. Thus, smoke visualization experiments similar to the ones used in [101], were used to estimate the average flow velocity under different conditions and to visualize the flow uniformity and velocity profile. Figure 96 shows frames of the videos used to estimate the velocity.

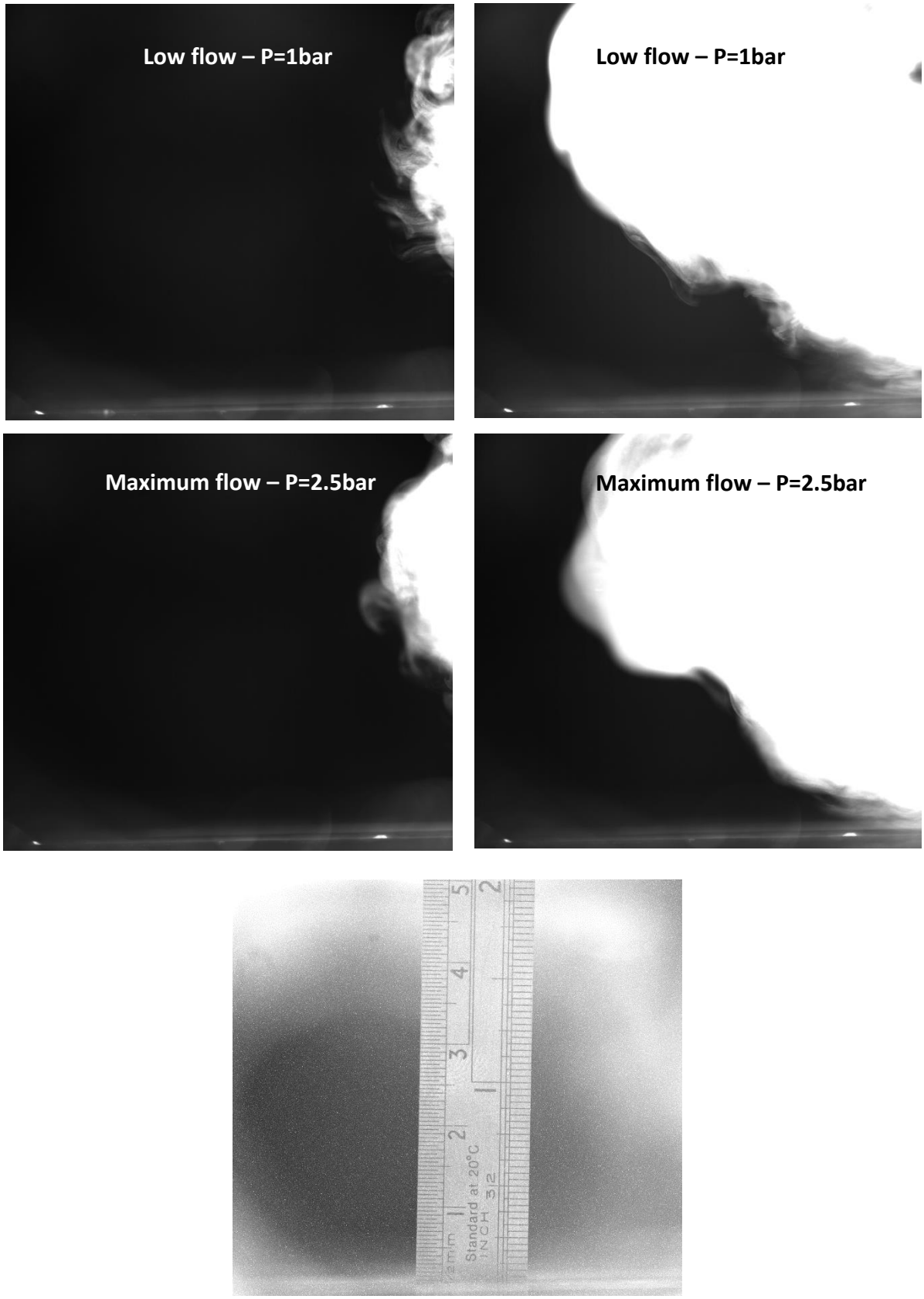

Figure 96. Velocity profile smoke visualization experiments under different operating conditions

In this experiment, the fluid velocity was varied by adjusting the output pressure from the argon cylinders. First, pressure/flowrate was gradually increased until a 50 µm layer of powder was disturbed. The maximum usable pressure was established to be 2.5bar. Under this condition, the flowrate was measured to be 95 L/min. A low flow condition (pressure=1bar and flowrate = 42 l/min) was also tested. The smoke visualization videos were analysed with ImageJ and the flow speed was calculated to be 0.8 ±0.1 m/s for the 2.5 bar condition and 0.6 ±0.15 m/s for the 1 bar condition.

In-process crossflow experiments

Schlieren imaging with a 6x6 mm view was used to examine the effect of the crossflow under different operating conditions.

In the first experiment (E1), the effectiveness of the of the maximum crossflow (P=2.5 bar, V ≈ 0.8m/s) was studied and compared to a no flow condition. In this experiment, no powder was used, and the laser was configured as follows: Spot diameter 50 µm; Power – 200W; Travel speed - 750 mm/s.

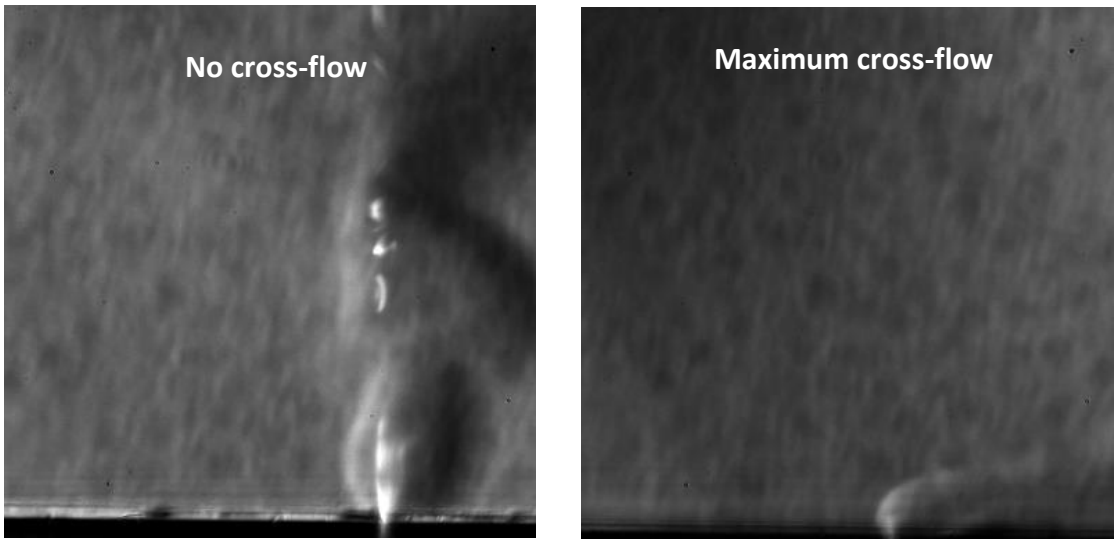

Figure 97. Example frames from experiment E1 (Spot diameter 50 µm; Power – 200W; Travel speed - 750 mm/s)

Figure 97 shows that the maximum crossflow is able to extract the plume and minimise its interaction with the laser. The no-flow condition experiment clearly shows how the laser can interact with plume. It is worth noting, that the background pattern shown in Figure 97, is due to defects in the optical path and does not represent flow disturbances. Figure 97 only shows selected frames from the high-speed videos.

The second experiment (E2), examines the interaction between the crossflow and the first layer of powder.

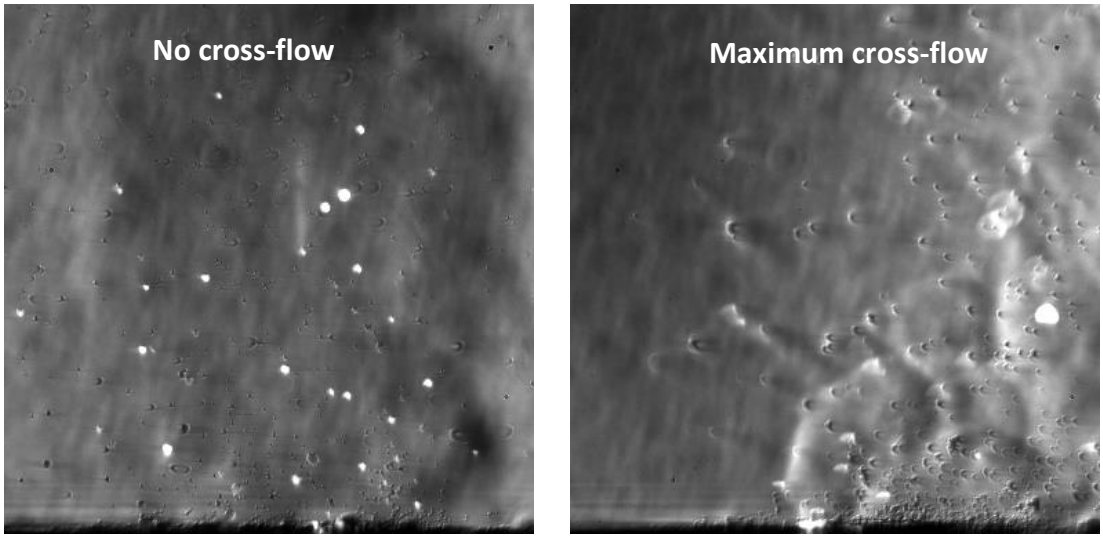

Figure 98. Example frames from experiment E2 (Spot diameter 50 µm; Power – 200W; Travel speed - 750 mm/s)

Experiment E2 shows that the crossflow not only reduces the interaction between the laser and the plume but also removes the ejected powder particles and spatter. Figure 98 shows that the powder particles ejected with the no flow condition are not removed and that a greater number of particles fall back on to the processing area. Figure 98 also shows that a greater number of the suspended particles are re-melted by the laser.

The third experiment (E3) examines the interaction between the crossflow and the powder once a steady state build process has been reached (layer 30).

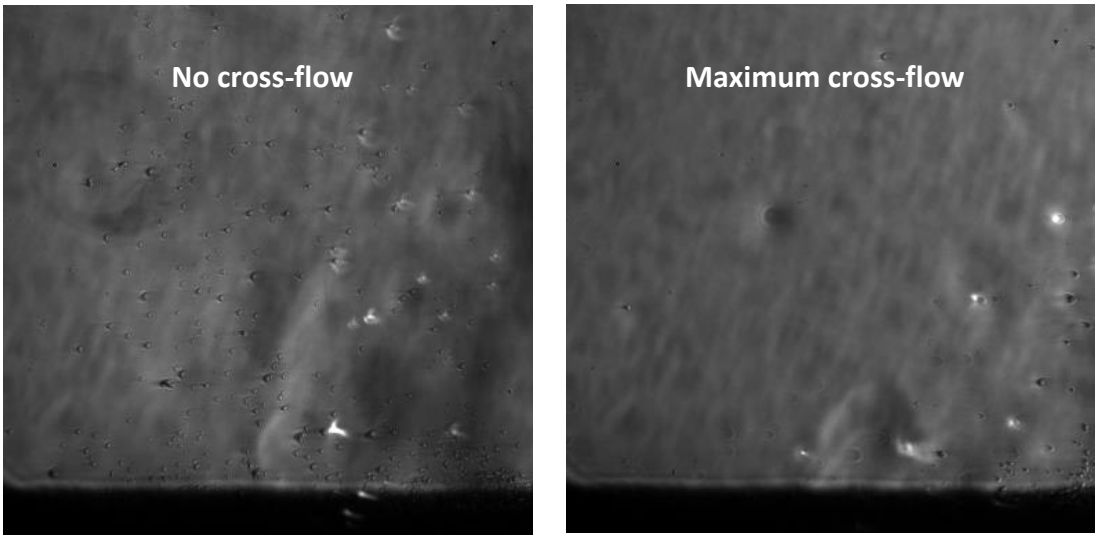

Figure 99. Example frames from experiment E3 (Spot diameter 50 µm; Power – 200W; Travel speed - 750 mm/s)

Figure 99 shows that the videos from experiment E3 show similar results to experiment E2.

Experiment E4 examines the effect of crossflow velocities on different process parameters at layer 1. In this experiment, the low flow (v≈0.6 m/s) and the high flow (V≈0.8 m/s) conditions were used with different laser parameters. Figure 100, shows the interaction between the different crossflows and the following laser parameters: Spot diameter 50 µm; Power – 200W; Travel speed - 750 mm/s.

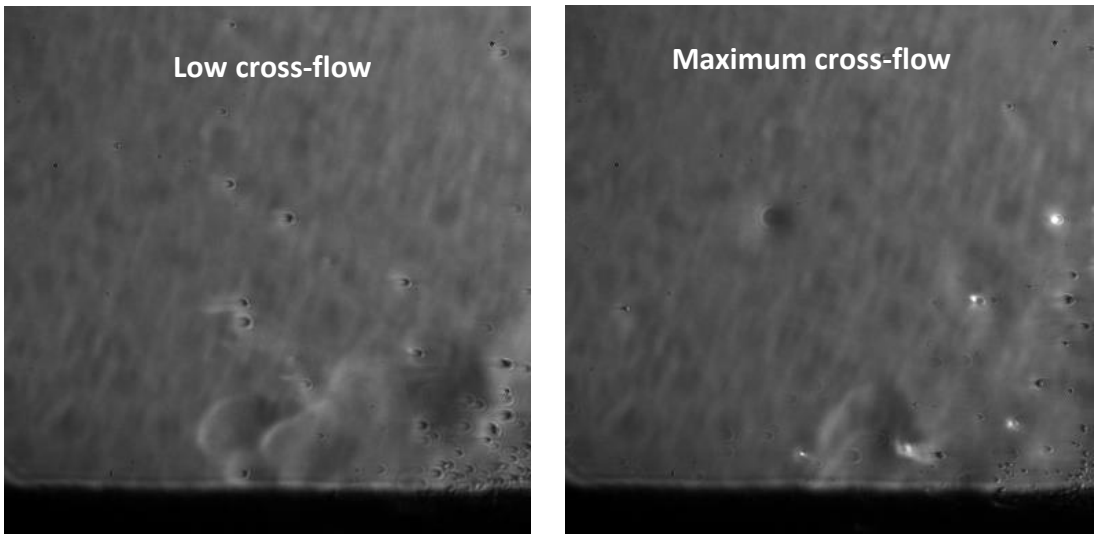

Figure 100. Example frames from experiment E4 with the 200W laser configuration (Spot diameter 50 µm; Power – 200W; Travel speed - 750 mm/s)

Figure 101, shows the interaction between the different crossflows and the following laser parameters: Spot diameter 50 µm; Power – 100W; Travel speed – 400 mm/s.

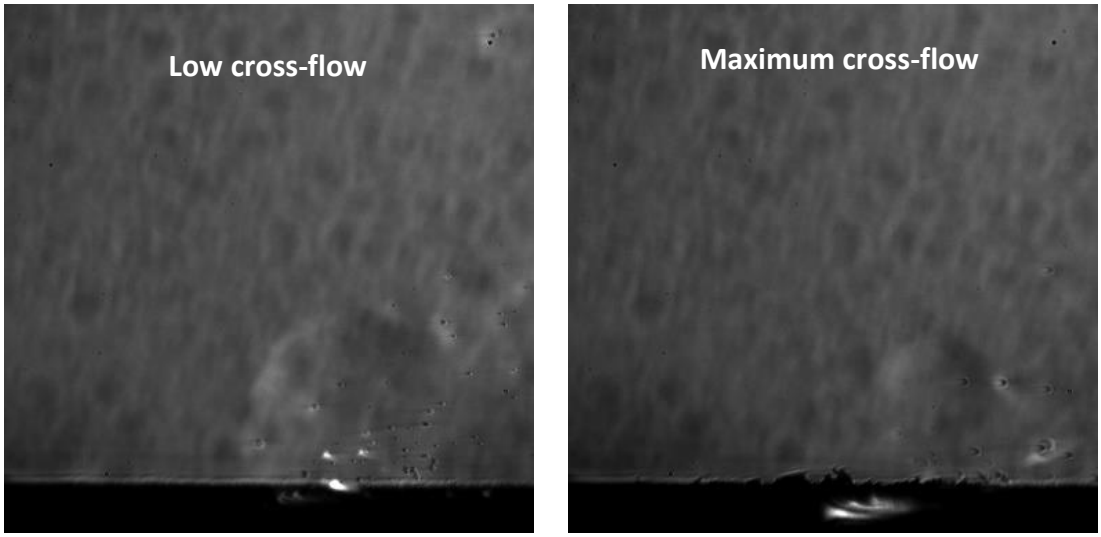

Figure 101. Example frames from experiment E4 with the 100W laser configuration (Spot diameter 50 µm; Power – 100W; Travel speed – 400 mm/s)

The results indicate that for the 200W configuration, the high flow condition extracts the plume and the particles at a faster rate. This results in a greater number of particles transported away from processing area and a reduction in the interaction between the plume and the laser. Thus, for the 200W configuration, the evidence suggests that a maximum flow is desirable. However, the 100W experiment showed that the maximum flow condition was directing the particles and metal vapour fumes back to processing area. This means that because of the lower intensity plume generated by the 100W laser, the high crossflow is able to alter the plume/particle trajectory quicker. The high flow does not allow the ejected particles and the metal vapor fumes to escape the processing area before they a re-deposited. This phenomenon can also be visibly observed after each layer has been deposited. For the 100W-high flow condition, the parts produced had a layer of soot from the deposition of the metal vapour fumes. It is worth noting that direct imaging experiments that complement the schlieren experiments were also conducted.

Experiment E4 indicates that the cross-flow speed should be selected to adequately remove the by-products from the processing area. Thus, to choose the appropriate flow speeds, the laser processing settings and part geometry should be considered. In

conclusion, the work indicates that the cross-flow speed should not always be selected to be as fast as possible.

4.5 Part Building with atmosphere control and crossflow device

The automation process, the design of the 1ppm controlled environment and the new crossflow has allowed the developed PBF machine to manufacture complex geometries directly from CAD models. The combination, of the controlled atmosphere and the crossflow gas, has dramatically increased process stability and part quality. Figure 102 shows examples of the parts created with the PBF system.

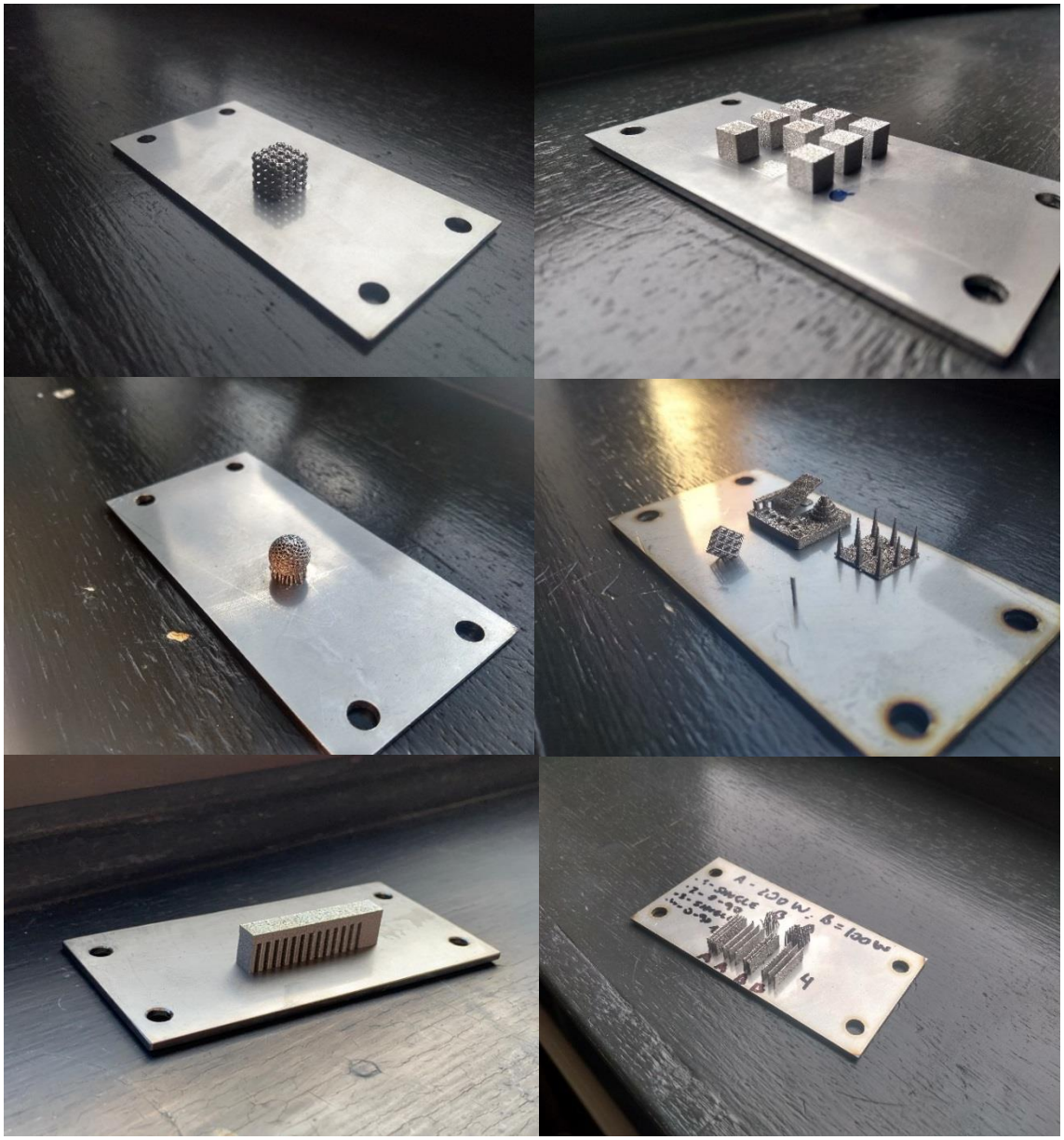

Figure 102. Example parts produced with the PBF machine

Figure 102 shows that the machine is able to create lattice structures and overhangs consistently. Further, the machine was able to build 100-layer single scan walls and multiple cubes under different parameters. The parameters used for example the builds range from 100 to 300W and 100 to 1300 mm/s. Without the crossflow and the new controlled enrolment, part building parameters were limited to 50W, due to the relatively small plume generated under such conditions. Before the new instalments, part building with industry standard parameters was unfeasible.

Chapter 5

GTAW-DED and PBF Conclusions and Future Work

5.1 Conclusions

The machines developed are working consistently and an are fully automated, i.e., no operator intervention is required at any point during the build process. The arc-length control system developed drastically improved process stability and part appearance. The GTAW-DED experimental apparatus can now deliver a constant transfer mode that fixes deposition errors and allows temperature to be measured consistently. This work shows that a successful temperature control system requires an arc-length control system be available.

Small improvements where observed with the use of the PID temperature control system. Peak temperatures were reduced by approximately 200°C. However, further process calibration is required to improve part appearance. The present results indicate that whilst a PID system might be able to control temperature in areas with constant heat transfer mechanisms, a feed-forward temperature control system might be required for those areas where the heat transfer mechanisms change. The literature also indicated that to improve process stability in GTAW-DED, oxidation should be reduced. Several trailing shield designs were tested and validated with multiple experiments, although further work is still required to identify if the developed GTAW-DED trailing shield would visibly improve part quality. From the GTWA-DED experiments, it can be concluded that that to improve part quality, multiple independent or MIMO control systems are required. The reduction of oxidation would likely improve temperature measurement by reducing oxide islands and the arc-length control system has proven to be essential for the development of a temperature control system.

The combination of oxygen monitoring and control, and the design of a laminar crossflow device based on the GTAW-DED trailing shield design has proven to drastically improve part quality in PBF. The control environment developed was able to maintain at atmosphere of 1 ppm consistently during the entire build process. The simple oxygen control system developed can detect if the oxygen concentration is above a user selected threshold and stop process to allow the crossflow device to reduce the oxygen concentration. The cross-flow device imaging experiments showed the interaction between the flow and the process by-products. From these experiments, it can be concluded that that the appropriate flow speed is dependent on process parameters and part geometry. The effectiveness of the crossflow at removing by-products is clearly shown by the imaging experiments and the drastic part quality improvement. With the new system, complex geometries that were previously unfeasible can now be consistently manufactured. From the PBF literature and experiments, in can also be concluded that to improve part quality, a combination of multiple independent control systems is likely required. The new PBF experimental apparatus is now ready to introduce new controls, such as a temperature control system.

GTAW-DED Future Work

Submerged wire-arc additive manufacturing

One of the main challenges of GTAW-DED is the heat accumulation over the build time due to changes in heat transfer mechanisms. Submerged wire-arc additive manufacturing (SWAAM) is a design idea to normalize heat transfer mechanisms over the entire part. The idea behind SWAAM is that a fluid -in this case water- will raise as layers are being deposited, only exposing the top three layers. The welding process and the molten metal will not be in contact with the water, removing the challenges of underwater welding. The increased cooling rate could drastically improve deposition rates without increasing inter-layer cooling time and preventing some of the geometrical inaccuracies induced by heat accumulation. The water will act as a heat sink during the entire deposition process. Figure 103, shows a prototype of the proposed manufacturing method.

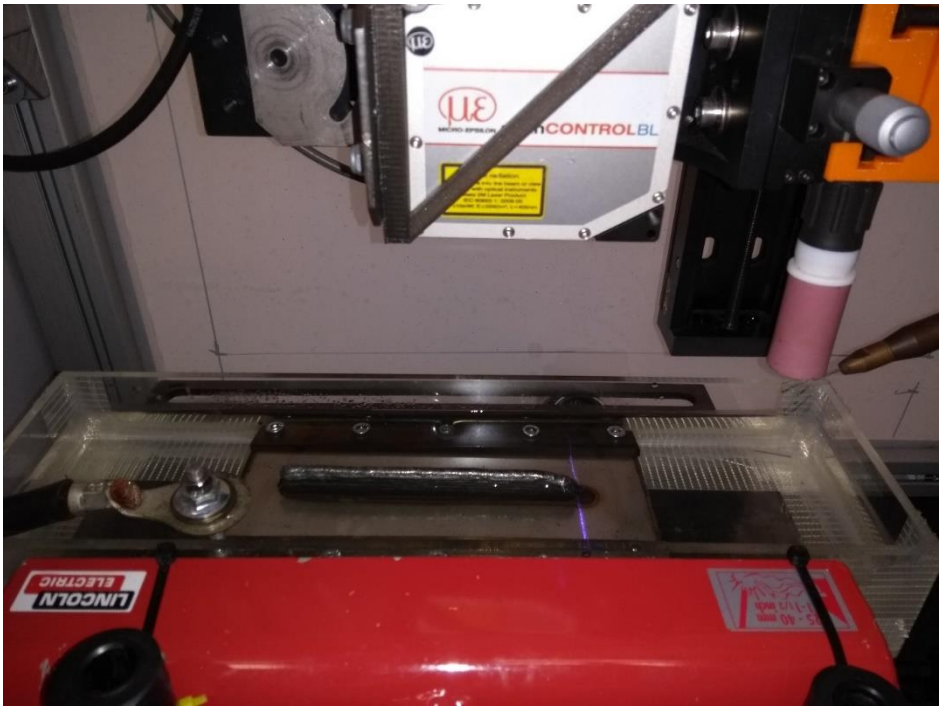

Figure 103. SWAAM experiment apparatus prototype

As shown in Figure 103, the GTAW-DED experimental apparatus was modified to incorporate a water tank. The water level was manually controlled with a water pump and the water was drained after the deposition of each layer to prevent it from heating

up. An additional possible feature of SWAAM, is that it can incorporate forced convection mechanisms to increase the heat transfer in localised areas. Figure 104, shows an example design of this system with a recirculation water pump.

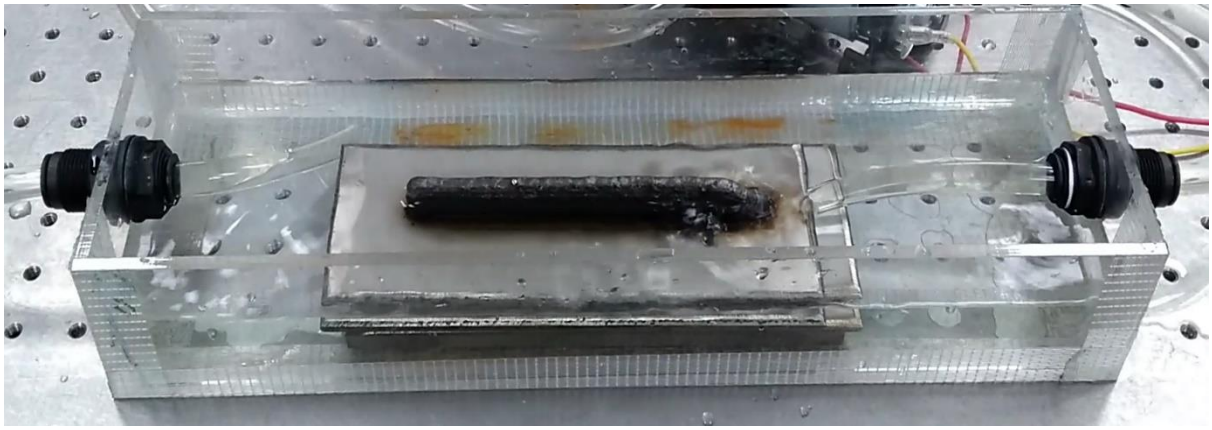

Figure 104. SWAAM experiment apparatus with a recirculation water pump for targeted forced convection

Preliminary tests of the SWAAM system show promising results. If the water level is maintained to approximately 3 layers from the top, the interaction between the water and the hot metal is minimal. The steam generation is particularly reduced with the used of the recirculating pump. Figure 105 shows an example 10-layer wall built with the SWAAM system and the arc-length control system.

Figure 105. Example of 10-layer wall built with the SWAAM experiment apparatus prototype

Figure 105 shows that with the use of SWAAM, a stable deposition process can be achieved. Further, the printed wall appears to be less oxidized than other 10-layer walls produced with a standard GTAW-DED process. However, evidence of oxidation is still present. To reduce oxidation, the trailing shield skirt design could be used to encase the top three layers of the wall.

In conclusion, SWAAM appears to show promising results and could be used to drastically improve GTAW-DED deposition process. However, further experiments are still required to cement the feasibility of the SWAAM.

Deposition strategy design

As highlighted in the literature, macrostructural deformations can be observed when every layer starts and ends at the same point. At the start of a deposition process, welding penetration is less than at the end of the wall due to heat accumulation. This can lead, to the commonly reported problem of tall beads at the beginning of a wall and a downwards slope at the end of the wall [88]. It has also been reported that way in which the material is added can also contribute to these deformations. To overcome these issues in a practical way, several reach groups have developed deposition strategies. Zhang et al., indicated that geometrical errors could be simply reduced by increasing the travel speed at the beginning of the part and gradually reducing travel speed at the end of the deposition [37]. Zeqi Hu et al., showed that switching the start and end positions every layer, an approach commonly known as zig-zag, can lead to a drastic reduction in the geometrical deformations [87] . Figure 106, shows an example of the different between a wall constructed with a standard deposition strategy and a wall constructed with a zig-zag approach in a GMAW-DED process.

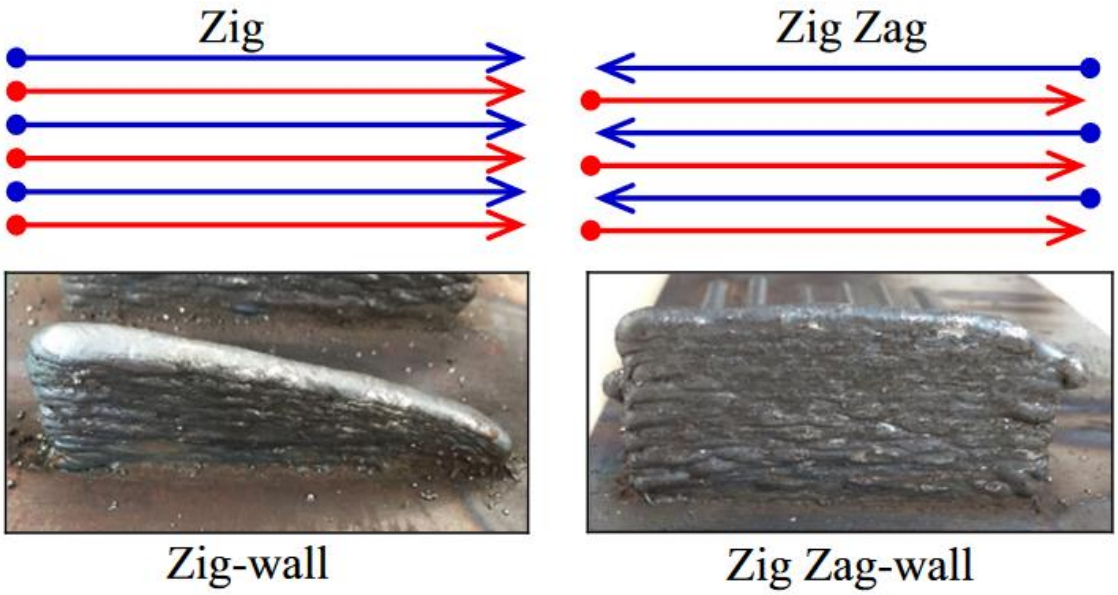

Figure 106. Comparison between zig and zig-zag walls (as reported by [87])

Following the conclusions from the literature, relatively simple design changes to the existing GTAW-DED process could be incorporated to add deposition versatility. Figure 107, shows the suggested design changes that would allow the welding bed of current GTAW-DED to rotate. This extra degree of freedom would a low for zig-zag deposition and for the creation of cylinders. The latter has been widely used by research groups in calibration experiments.

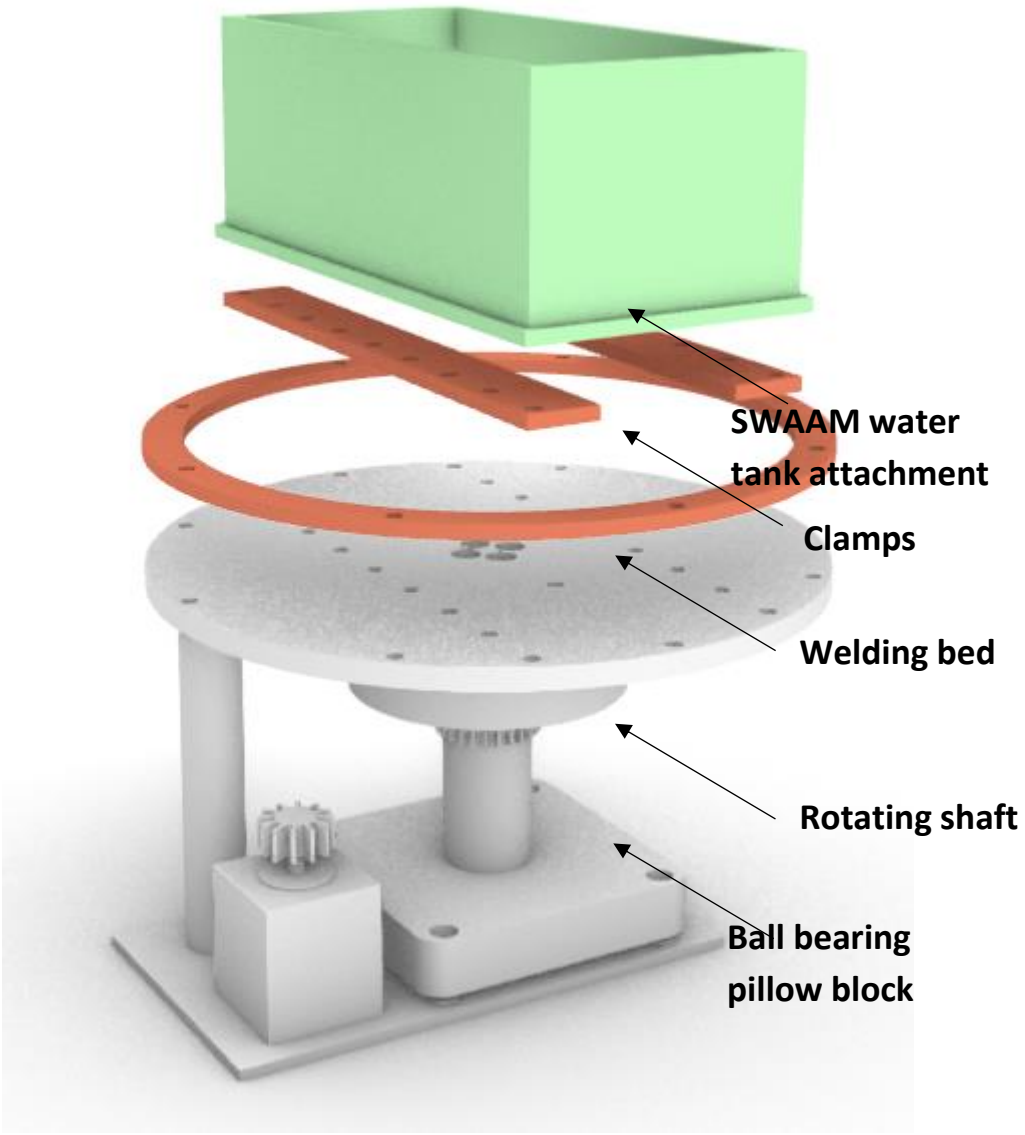

Figure 107. Rotating welding bed design for the GTAW-DED experiment apparatus

References

[1] T. Wohlers, "Tracking Global Growth in Industrial-Scale Additive Manufacturing", *3D Printing and Additive Manufacturing*, vol. 1, no. 1, pp. 2-3, 2014.

[2] G. Tapia and A. Elwany, "A Review on Process Monitoring and Control in Metal-Based Additive Manufacturing", *Journal of Manufacturing Science and Engineering*, vol. 136, no. 6, p. 060801, 2014.

[3] A. Heralić, A. Christiansson and B. Lennartson, "Height control of laser metal-wire deposition based on iterative learning control and 3D scanning", *Optics and Lasers in Engineering*, vol. 50, no. 9, pp. 1230-1241, 2012.

[4] "ASTM F2792 - 12a Standard Terminology for Additive Manufacturing Technologies, (Withdrawn 2015)", *Astm.org*, 2017. [Online]. Available: http: //www.astm.org/Standards/F2792.htm. [Accessed: 29- Nov- 2017].

[5] A. Heralić, A. Christiansson, K. Hurtig, M. Ottosson and B. Lennartson, "Control Design for Automation of Robotized Laser Metal-wire Deposition", *IFAC Proceedings Volumes*, vol. 41, no. 2, pp. 14785-14791, 2008.

[6] S. Williams, F. Martina, A. Addison, J. Ding, G. Pardal and P. Colegrove, "Wire + Arc Additive Manufacturing", 2017.

[7] Y. Ma, D. Cuiuri, H. Li, Z. Pan and C. Shen, "The effect of postproduction heat treatment on γ-TiAl alloys produced by the GTAW-based additive manufacturing process", *Materials Science and Engineering: A*, vol. 657, pp. 86-95, 2016.

[8] J. Xiong, Z. Yin and W. Zhang, "Closed-loop control of variable layer width for thin-walled parts in wire and arc additive manufacturing", *Journal of Materials Processing Technology*, vol. 233, pp. 100-106, 2016.

[9] L. Song, V. Bagavath-Singh, B. Dutta and J. Mazumder, "Control of melt pool temperature and deposition height during direct metal deposition process", *The International Journal of Advanced Manufacturing Technology*, vol. 58, no. 1-4, pp. 247-256, 2011.

[10] X. Xu, J. Ding, S. Ganguly, C. Diao and S. Williams, "Oxide accumulation effects on wire + arc layer-by-layer additive manufacture process", *Journal of Materials Processing Technology*, vol. 252, pp. 739-750, 2018.

[11] K. Zeng and D. Pal, "A Review of Thermal Analysis Methods in Laser Sintering and Selective Laser Melting", *Proceedings of the Solid Freeform Fabrication Symposium, Austin*, pp. 796–814, 2012.

[12] H. Geng, J. Li, J. Xiong, X. Lin and F. Zhang, "Optimization of wire feed for GTAW based additive manufacturing", *Journal of Materials Processing Technology*, vol. 243, pp. 40-47, 2017.

[13] D. Yang, G. Wang and G. Zhang, "Thermal analysis for single-pass multi-layer GMAW based additive manufacturing using infrared thermography", *Journal of Materials Processing Technology*, vol. 244, pp. 215-224, 2017.

[14] G. Bi, A. Gasser, K. Wissenbach, A. Drenker and R. Poprawe, "Identification and qualification of temperature signal for monitoring and control in laser cladding", *Optics and Lasers in Engineering*, vol. 44, no. 12, pp. 1348-1359, 2006.

[15] M. Liberini, A. Astarita, G. Campatelli, A. Scippa, F. Montevecchi, G. Venturini, M. Durante, L. Boccarusso, F. Minutolo and A. Squillace, "Selection of Optimal Process Parameters for Wire Arc Additive Manufacturing", *Procedia CIRP*, vol. 62, pp. 470-474, 2017.

[16] A. Heralić, A. Christiansson, K. Hurtig, M. Ottosson and B. Lennartson, "Visual feedback for operator interaction in robotized laser metal deposition", *International Conference on Surface Modification Technologies*, 2008.

[17] S. Writer, “Metal-based additive manufacturing: about to take off? - Manufacturers’ Monthly,” Manufacturers’ Monthly, 19-Nov-2016. [Online]. Available: https://www.manmonthly.com.au/features/metal-based-additive-manufacturing-take-off/. [Accessed: 24-Jun-2019].

[18] T. Craeghs, S. Clijsters, E. Yasa, J.-P. Kruth, Online quality control of selective laser melting, Solid Free. Fabr. Proc. (2011) 212–226.

[19] P. Bidare, R. R. J. Maier, R. J. Beck, J. D. Shephard, and A. J. Moore, “An open-architecture metal powder bed fusion system for in-situ process measurements,” Additive Manufacturing, vol. 16, pp. 177–185, Aug. 2017.

[20] M. Schniedenharn, F. Wiedemann, and J. H. Schleifenbaum, “Visualization of the shielding gas flow in SLM machines by space-resolved thermal anemometry,” Rapid Prototyping Journal, vol. 24, no. 8, pp. 1296–1304, Nov. 2018.

[21] A. G. Demir, “Micro laser metal wire deposition for additive manufacturing of thin-walled structures,” Optics and Lasers in Engineering, vol. 100, pp. 9–17, Jan. 2018.

[22] A. M. Philo et al., “A Multiphase CFD Model for the Prediction of Particulate Accumulation in a Laser Powder Bed Fusion Process,” CFD Modeling and Simulation in Materials Processing 2018, pp. 65–76, 2018.

[23] “Feature article: Design for metal AM - a beginner’s guide: Educational AM Article, Feature Article, Design for metal AM,” Renishaw.com, 2019. [Online]. Available: https://resources.renishaw.com/en/details/feature-article-design-for-metal-am-a-beginners-guide--101490. [Accessed: 23-May-2019].

[24] C. Pauzon, E. Hryha, P. Forêt, and L. Nyborg, “Effect of argon and nitrogen atmospheres on the properties of stainless steel 316 L parts produced by laser-powder bed fusion,” Materials & Design, p. 107873, May 2019.

[25] A. B. Anwar, I. H. Ibrahim, and Q.-C. Pham, “Spatter transport by inert gas flow in selective laser melting: A simulation study,” Powder Technology, vol. 352, pp. 103–116, Jun. 2019.

[26] A. Fathi, A. Khajepour, E. Toyserkani and M. Durali, "Clad height control in laser solid freeform fabrication using a feedforward PID controller", *The International Journal of Advanced Manufacturing Technology*, vol. 35, no. 3-4, pp. 280-292, 2006.

[27] J. Jeng and M. Lin, "Mould fabrication and modification using hybrid processes of selective laser cladding and milling", *Journal of Materials Processing Technology*, vol. 110, no. 1, pp. 98-103, 2001.

[28] L. Song and J. Mazumder, "Feedback Control of Melt Pool Temperature During Laser Cladding Process", *IEEE Transactions on Control Systems Technology*, vol. 19, no. 6, pp. 1349-1356, 2011.

[29] L. Song, V. Bagavath-Singh, B. Dutta and J. Mazumder, "Control of melt pool temperature and deposition height during direct metal deposition process", *The International Journal of Advanced Manufacturing Technology*, vol. 58, no. 1-4, pp. 247-256, 2011.

[30] G. Marshall, W. Young, S. Thompson, N. Shamsaei, S. Daniewicz and S. Shao, "Understanding the Microstructure Formation of Ti-6Al-4V During Direct Laser Deposition via In-Situ Thermal Monitoring", *JOM*, vol. 68, no. 3, pp. 778-790, 2016.

[31] E. Toyserkani and A. Khajepour, "A mechatronics approach to laser powder deposition process", *Mechatronics*, vol. 16, no. 10, pp. 631-641, 2006.

[32] "Metal Additive Manufacturing processes", *Metal Additive Manufacturing*, 2017. [Online]. Available: http://www.metal-am.com/introduction-to-metal-additive-manufacturing-and-3d-printing/metal-additive-manufacturing-processes/. [Accessed: 01- Dec- 2017].

[33] D. Pryadko, "A real thing: 3D printing with metal - how it works - AptGadget.com", *AptGadget.com*, 2017. [Online]. Available: http://aptgadget.com/a-real-thing-3d-printing-with-metal-how-it-works/. [Accessed: 01- Dec- 2017].

[34] J. Xiong and G. Zhang, "Adaptive control of deposited height in GMAW-based layer additive manufacturing", *Journal of Materials Processing Technology*, vol. 214, no. 4, pp. 962-968, 2014.

[35] J. Xiong, Z. Yin and W. Zhang, "Closed-loop control of variable layer width for thin-walled parts in wire and arc additive manufacturing", *Journal of Materials Processing Technology*, vol. 233, pp. 100-106, 2016.

[36] Rapid prototyping of metal parts by three-dimensional welding Proceedings of the Institution of Mechanical Engineers, Part B: Journal of Engineering Manufacture - J D Spencer, P M Dickens, C M Wykes, 1998", *Journals.sagepub.com*, 2017. [Online]. Available: http://journals.sagepub.com/doi/abs/10.1243/0954405981515590?journalCode=pibb #articleCitationDownloadContainer. [Accessed: 01- Dec- 2017].

[37] Y. Zhang, Y. Chen, P. Li and A. Male, "Weld deposition-based rapid prototyping: a preliminary study", *Journal of Materials Processing Technology*, vol. 135, no. 2-3, pp. 347-357, 2003.

[38] X. Xiong, H. Zhang and G. Wang, "Metal direct prototyping by using hybrid plasma deposition and milling", *Journal of Materials Processing Technology*, vol. 209, no. 1, pp. 124-130, 2009.

[39] K. Karunakaran, S. Suryakumar, V. Pushpa and S. Akula, "Low cost integration of additive and subtractive processes for hybrid layered manufacturing", *Robotics and Computer-Integrated Manufacturing*, vol. 26, no. 5, pp. 490-499, 2010.

[40] B. Baufeld, E. Brandl and O. van der Biest, "Wire based additive layer manufacturing: Comparison of microstructure and mechanical properties of Ti–6Al–4V components fabricated by laser-beam deposition and shaped metal deposition", *Journal of Materials Processing Technology*, vol. 211, no. 6, pp. 1146-1158, 2011.

[41] F. Martina, J. Mehnen, S. Williams, P. Colegrove and F. Wang, "Investigation of the benefits of plasma deposition for the additive layer manufacture of Ti–6Al–4V", *Journal of Materials Processing Technology*, vol. 212, no. 6, pp. 1377-1386, 2012.

[42] F. Martina, P. Colegrove, S. Williams and J. Meyer, "Microstructure of Interpass Rolled Wire + Arc Additive Manufacturing Ti-6Al-4V Components", *Metallurgical and Materials Transactions A*, vol. 46, no. 12, pp. 6103-6118, 2015.

[43] D. Yang, G. Wang and G. Zhang, "Thermal analysis for single-pass multi-layer GMAW based additive manufacturing using infrared thermography", Journal of Materials Processing Technology, vol. 244, pp. 215-224, 2017.

[44] Y. Song, S. Park, D. Choi and H. Jee, "3D welding and milling: Part I–a direct approach for freeform fabrication of metallic prototypes", *International Journal of Machine Tools and Manufacture*, vol. 45, no. 9, pp. 1057-1062, 2005.

[45] "Consortium Claims World First with 3D Printed Propeller", *Porttechnology.org*, 2017. [Online]. Available: https://www.porttechnology.org/news/consortium_claims_world_first_with_3d_printed_propeller. [Accessed: 01- Dec- 2017].

[46] A. Heralić, A. Christiansson, M. Ottosson and B. Lennartson, "Increased stability in laser metal wire deposition through feedback from optical measurements", *Optics and Lasers in Engineering*, vol. 48, no. 4, pp. 478-485, 2010.

[47] W. Syed, A. Pinkerton and L. Li, "A comparative study of wire feeding and powder feeding in direct diode laser deposition for rapid prototyping", *Applied Surface Science*, vol. 247, no. 1-4, pp. 268-276, 2005.

[48] Zeng, K., Pal, D., and Stucker, B., 2012, “A Review of Thermal Analysis Methods in Laser Sintering and Selective Laser Melting,” Proceedings of the Solid Freeform Fabrication Symposium, Austin, TX, pp. 796–814.

[49] T. Hua, C. Jing, L. Xin, Z. Fengying and H. Weidong, "Research on molten pool temperature in the process of laser rapid forming", *Journal of Materials Processing Technology*, vol. 198, no. 1-3, pp. 454-462, 2008.

[50] "WP-197 Additive Layer Manufacturing (ALM)", Huntingdonfusion.com, 2018. [Online]. Available: https://www.huntingdonfusion.com/index.php/en/technical-

support/white-papers-40017/2757-wp-197-additive-layer-manufacturing. [Accessed: 04- Jul- 2018].

[51] M. Griffith, M. Schlienger, L. Harwell, M. Oliver, M. Baldwin, M. Ensz, M. Essien, J. Brooks, C. Robino, J. Smugeresky, W. Hofmeister, M. Wert and D. Nelson, "Understanding thermal behaviour in the LENS process", *Materials & Design*, vol. 20, no. 2-3, pp. 107-113, 1999.

[52] Backes G, Kreutz EW, Gasser A, Stromeyer R, Wissenbach K. Process monitoring and control during alloying and cladding with CO2 laser radiation. European conference on laser treatment of materials (ECLAT), 22–23 September 1998, Hannover, Germany, p. 227–36.

[53] Klocke F, Scheller D. Process monitoring in laser surface treatment operations with reflection and temperature measurement. Prod Eng 1997; 4(1):39–44.

[54] Ignatiev M, Smurov I, Flamant G. Real time optical pyrometry in laser machining. Meas Sci Technol 1994; 5:563–73

[55] Smurov I. Pyrometry applications in laser machining. Proc SPIE 2001; 4157:55–66.

[56] L. Han et al., "Modelling of laser cladding with powder injection," Metallurgical Mater. Trans. B-Process Metallurgy Mater. Process. Sci., vol. 35, pp. 1139–1150, Dec. 2004.

[57] M. Doubenskaia et al., "Optical monitoring of Nd: YAG laser cladding," Thin Solid Films, vol. 453, pp. 477–485, 2004.

[58] G. J. Bi et al., "Development and qualification of a novel laser-cladding head with integrated sensors," Int. J. Mach. Tools Manuf., vol. 47, pp. 555 –561, Mar. 2007.

[59] G. J. Bi et al., "Investigation on the direct laser metallic powder deposition process via temperature measurement," Appl. Surf. Sci., vol. 253, pp. 1411 –1416, 2006.

[60] F.Meriaudeau and F. Truchetet, “Control and optimization of the laser cladding process using matrix cameras and image processing ,” J. Laser Appl., vol. 8, pp. 317–324, Dec. 1996.

[61] D. M. Hu and R. Kovacevic, “Sensing, modelling and control for laser-based additive manufacturing,” Int. J. Mach. Tools Manuf., vol. 43, pp. 51–60, Jan. 2003.

[62] H. Köhler, C. Thomy and F. Vollertsen, "Contact-less temperature measurement and control with applications to laser cladding", Welding in the World, vol. 60, no. 1, pp. 1-9, 2015.

[63] "Thermocouples Operating Principles", Msm.cam.ac.uk, 2017. [Online]. Available: https://www.msm.cam.ac.uk/utc/thermocouple/pages/ThermocouplesOperatingPrinciples.html. [Accessed: 21- Dec- 2017].

[64] Temperature Measurement. Web.mst.edu, 2017. [Online]. Available: https://web.mst.edu/~cottrell/ME240/Resources/Temperature/Temperature.pdf. [Accessed: 21- Dec- 2017].

[65] F. Martina, "Investigation of methods to manipulate geometry, microstructure and mechanical properties in titanium large scale Wire+Arc Additive Manufacturing", *Cranfield University doctoral thesis*, 2014.

[66] “Unsheathed Fine Gage Tungsten-Rhenium Microtemp Thermocouples,” Omega.co.uk, 2019. [Online]. Available: https://www.omega.co.uk/pptst/TOR-BW.html. [Accessed: 23-May-2019].

[67] J. Ding, P. Colegrove, F. Martina, S. Williams, R. Wiktorowicz, and M. R. Palt, “Development of a laminar flow local shielding device for wire + arc additive manufacture,” Journal of Materials Processing Technology, vol. 226, pp. 99–105, Dec. 2015.

[68] D. Salehi and M. Brandt, "Melt pool temperature control using LabVIEW in Nd:YAG laser blown powder cladding process", The International Journal of Advanced Manufacturing Technology, vol. 29, no. 3-4, pp. 273-278, 2005.

[69] Hua Y, Choi J (2005) Adaptive direct metal/material deposition process using a fuzzy logic-based controller. J Laser Appl 17 (4):200–210

[70] Toyserkani E, Khajepour A, Corbin SF (2002) Application of experimental-based modelling to laser cladding. J Laser Appl 14 (3):165–173

[71] J. Koch and J.Mazumder, “Apparatus and methods for monitoring and controlling multi-layer laser cladding,” U.S. Patent 6 122 564, Sep. 19, 2000.

[72] C. Doumanidis and Y. Kwak, "Multivariable adaptive control of the bead profile geometry in gas metal arc welding with thermal scanning", International Journal of Pressure Vessels and Piping, vol. 79, no. 4, pp. 251-262, 2002.

[73] J. Kim and Y. Peng, "Plunging method for Nd: YAG laser cladding with wire feeding", *Optics and Lasers in Engineering*, vol. 33, no. 4, pp. 299-309, 2000.

[74] J.D. Kim, Y. Peng, Opt. Lasers Eng. 33 (2000) 299

[75] Some practical aspects of surface temperature measurement by optical and ratio pyrometers", *Ntrs.nasa.gov*, 1966. [Online]. Available: https://ntrs.nasa.gov/archive/nasa/casi.ntrs.nasa.gov/19660026358.pdf. [Accessed: 04- Jul- 2018].

[76] A. Book, "TR Two-colour pyrometer 201507 en - Keller ITS (Infrared Temperature Solutions) - PDF Catalogue | Technical Documentation | Brochure", *Pdf.directindustry.com*, 2018. [Online]. Available: http://pdf.directindustry.com/pdf/keller-its-infrared-temperature-solutions/tr-two-colour-pyrometer-201507-en/14914-705255.html. [Accessed: 04- Jul- 2018].

[77] P. A. Hooper, “Melt pool temperature and cooling rates in laser powder bed fusion,” Additive Manufacturing, vol. 22, pp. 548–559, Aug. 2018.

[78] Burgess, G. and Waltenberg, R. (n.d.). The emmisivity of metals and oxides.

[79]“Fluke Process Instruments,” Flukeprocessinstruments.com, 2019. [Online]. Available: https://www.flukeprocessinstruments.com/en-us/service-and-

support/knowledge-center/infrared-technology/how-do-ratio-pyrometers-work. [Accessed: 29-May-2019].

[80] J-D. Kim and Y. Peng. Plunging method for Nd:YAG laser cladding with wire feeding. Optics and Lasers in Engineerng, 33(4):299–309, 2000.

[81] R.M. Miranda, G. Lopes, L. Quintino, J.P. Rodrigues, and S. Williams. Rapid prototyping with high power fibre lasers. Materials and D [62] esign, 29:2072–2075, 2008.

[82] S.H. Mok, G. Bi, J. Folkes, and I. Pashby. Deposition of Ti6Al4V using a high-power diode laser and wire, Part I: Investigation on the process characteristics. Surface and Coatings Technology, 202:3933–3939, 2008

[83] F. Moures, E. Cicala, P. Sallamand, D. Grevey, B. Vannes, and S. Ignat. Optimisation of refractory coatings realised with cored wire addition using a high-power diode laser. International Journal of Machine Tools and Manufacture, 200:2283–2292, 2005.

[84]“PID Theory Explained - National Instruments,” Ni.com, 2019. [Online]. Available: http://www.ni.com/en-gb/innovations/white-papers/06/pid-theory-explained.html.

[85] “Home - www.caltech.edu,” Caltech.edu, 2019. [Online]. Available: https://www.cds.caltech.edu/~murray/courses/cds101/fa04/caltech/am04_ch8-3nov04.pdf. [Accessed: 29-May-2019].

[86] S. Temel, S. Yagli, and S. Goren, “Discrete Time Control Systems,” Researchgate. [Online].
Available:https://www.google.com/url?sa=t&rct=j&q=&esrc=s&source=web&cd=1&ved=2ahUKEwj9sPS37sDiAhV1SBUIHYmwAvoQFjAAegQIABAC&url=https%3A%2F%2Fwww.researchgate.net%2Ffile.PostFileLoader.html%3Fid%3D54685991d11b8bc9668b461a%26assetKey%3DAS%253A273635200176128%2540144225112395 4&usg=AOvVaw2zOzkD7QaAg0eclQFeo91Q.

[87] Z. Hu, X. Qin, T. Shao, and H. Liu, “Understanding and overcoming of abnormity at start and end of the weld bead in additive manufacturing with GMAW,” The

International Journal of Advanced Manufacturing Technology, vol. 95, no. 5–8, pp. 2357–2368, Nov. 2017.

[88] T. A. Rodrigues, V. Duarte, R. M. Miranda, T. G. Santos, and J. P. Oliveira, “Current Status and Perspectives on Wire and Arc Additive Manufacturing (WAAM),” Materials, vol. 12, no. 7, p. 1121, Apr. 2019.

[89] V. Kulkarni, N. Sahoo, and S. D. Chavan, “Simulation of honeycomb–screen combinations for turbulence management in a subsonic wind tunnel,” Journal of Wind Engineering and Industrial Aerodynamics, vol. 99, no. 1, pp. 37–45, Jan. 2011.

[90] Babish, F, 2007. Guide for the fusion welding of titanium and titanium allows, AWS. G2.4-G2.4M-2007

[91]Mazumdar, Amrita. “Principles and Techniques of Schlieren Imaging Systems.” (2013).

[92]“Schlieren Flow Visualization,” Nasa.gov, 2015. [Online]. Available: https://www.grc.nasa.gov/www/k-12/airplane/tunvschlrn.html. [Accessed: 07-Jun-2019].

[93] G.J Gibson, Gas flow requirements for inert-gas shielded arc welding, Weld. J. 32 (1953) 128a-208s

[94] M. Dreher, U. Füssel, S. Rose, M. Häßler, M. Hertel, and M. Schnick, “Methods and results concerning the shielding gas flow in GMAW,” Welding in the World, Mar. 2013.

[95] I. Bitharas, S. W. Campbell, A. M. Galloway, N. A. McPherson, and A. J. Moore, “Visualisation of alternating shielding gas flow in GTAW,” Materials & Design, vol. 91, pp. 424–431, Feb. 2016.

[96] R. Li, J. Liu, Y. Shi, L. Wang, and W. Jiang, “Balling behavior of stainless steel and nickel powder during selective laser melting process,” The International Journal of Advanced Manufacturing Technology, vol. 59, no. 9–12, pp. 1025–1035, Aug. 2011.

[97] B. Ferrar, L. Mullen, E. Jones, R. Stamp, and C. J. Sutcliffe, “Gas flow effects on selective laser melting (SLM) manufacturing performance,” Journal of Materials Processing Technology, vol. 212, no. 2, pp. 355–364, Feb. 2012.

[98]A. Ladewig, G. Schlick, M. Fisser, V. Schulze, and U. Glatzel, “Influence of the shielding gas flow on the removal of process by-products in the selective laser melting process,” Additive Manufacturing, vol. 10, pp. 1–9, Apr. 2016.

[99] A. B. Anwar and Q.-C. Pham, “Selective laser melting of AlSi10Mg: Effects of scan direction, part placement and inert gas flow velocity on tensile strength,” Journal of Materials Processing Technology, vol. 240, pp. 388–396, Feb. 2017.

[100] “Air Duct Components and Minor Dynamic Loss Coefficients,” Engineeringtoolbox.com, 2019. [Online]. Available: https://www.engineeringtoolbox.com/minor-loss-air-ducts-fittings-d_208.html. [Accessed: 24-Jun-2019].

[101] W.-C. Wang and C.-Y. Chang, “Flow analysis of the laminated manufacturing system with laser sintering of metal powder. Part I: flow uniformity inside the working chamber,” The International Journal of Advanced Manufacturing Technology, vol. 92, no. 1–4, pp. 1299–1314, Mar. 2017.

Appendix

A. Two colour pyrometer calibration graphs

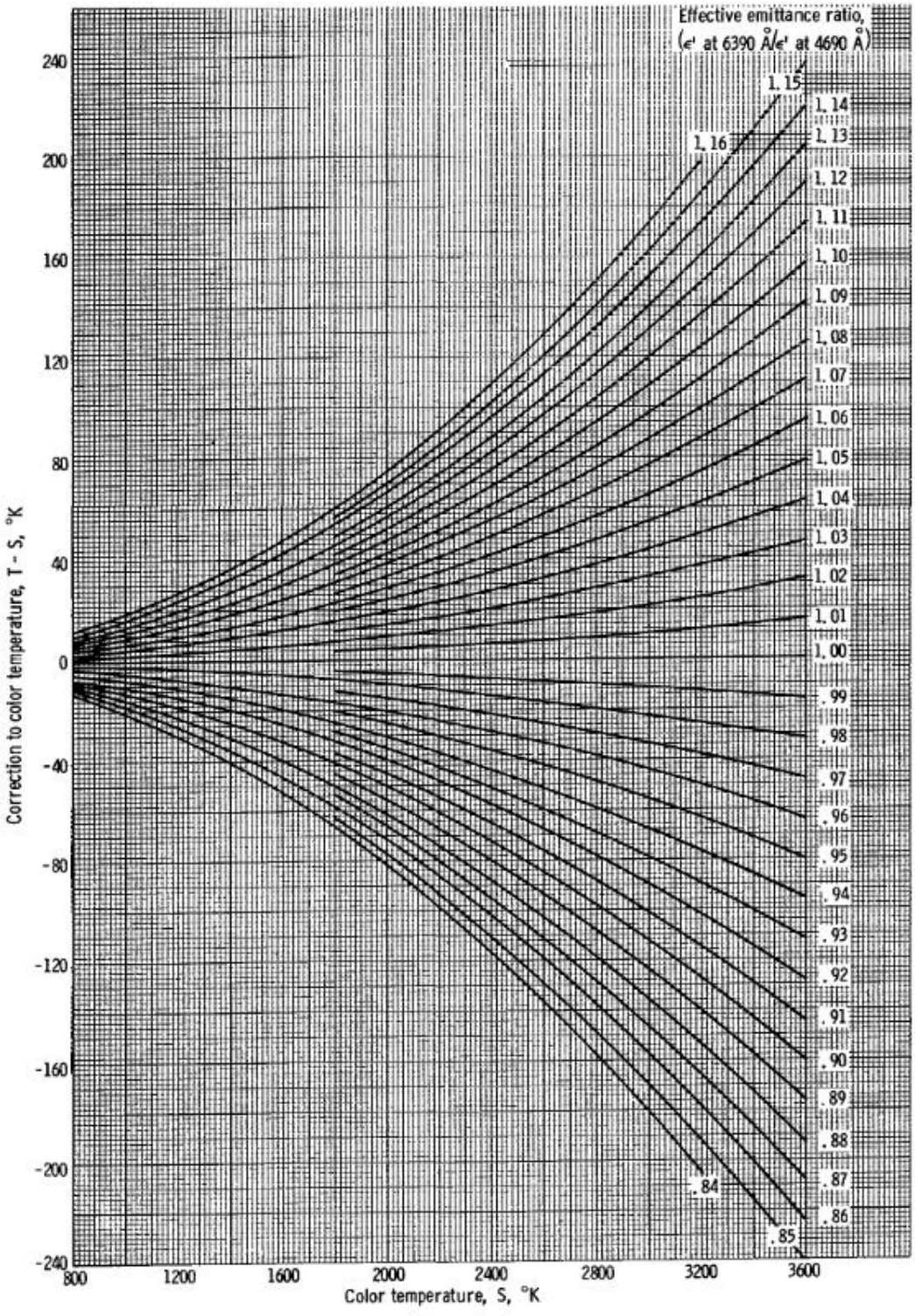

(a) Band passes at 6390 and 4690 angstroms.

Figure 29. - Color-temperature correction for a ratio pyrometer.

B. Fixed point pyrometer experiment with offsets